Distribution Agreement

In presenting this thesis or dissertation as a partial fulfillment of the requirements for an advanced degree from Emory University, I hereby grant to Emory University and its agents the non-exclusive license to archive, make accessible, and display my thesis or dissertation in whole or in part in all forms of media, now or hereafter known, including display on the world wide web. I understand that I may select some access restrictions as part of the online submission of this thesis or dissertation. I retain all ownership rights to the copyright of the thesis or dissertation. I also retain the right to use in future works (such as articles or books) all or part of this thesis or dissertation.

Signature:

_____ _____

Kyle John Mascaritolo Date

A Journey towards the Construction and Operation of a Photoelectron Velocity-Map Imaging Spectrometer

By

Kyle John Mascaritolo
Doctor of Philosophy
Chemistry

_____

Michael C. Heaven, Ph. D.
Advisor

_____

James T. Kindt, Ph. D.
Committee Member

_____

Susanna L. Widicus Weaver, Ph. D.
Committee Member

Accepted:

_____

Lisa A. Tedesco, Ph.D.
Dean of the James T. Laney School of Graduate Studies

_____

Date

A Journey towards the Construction and Operation of a Photoelectron Velocity-Map Imaging Spectrometer

By

Kyle John Mascaritolo

B.S., Georgia Southern University, 2010

Advisor: Michael C. Heaven, Ph. D.

An abstract of
A dissertation submitted to the Faculty of the
James T. Laney School of Graduate Studies of Emory University
in partial fulfillment of the requirements for the degree of
Doctor of Philosophy
in Chemistry
2016

Abstract

A Journey towards the Construction and Operation of a Photoelectron Velocity-Map Imaging Spectrometer

By Kyle John Mascaritolo

Photoelectron velocity – map imaging spectroscopy is a highly versatile spectroscopic technique that is capable of measuring numerous molecular properties of neutral and anionic gas phase species. Pioneered by Dr. Danial Neumark at the University of California, Berkeley, it combines anion photodetachment spectroscopy with velocity – map imaging spectroscopy.

Presented here is a report of the evolution of a spectrometer capable of studying beryllium containing molecules with the use of photoelectron velocity – map imaging spectroscopy. During the development of the spectrometer, several sub-projects were executed to benchmark its performance. The $^2\Pi(4p)$-X $^2\Pi$ $(3p)$ band system of the AlAr van der Waals complex using two-photon excitation was first studied to measure the production of internally cold molecules from the laser ablation source. With the determination that cold molecules could be produced, the radical BeOH was studied. The ground state of BeOH was predicted to have a bent equilibrium structure, contrary to the other alkaline earth metal hydroxides with linear equilibrium ground state geometries. The use of laser excitation techniques to observe the $2^2A'$-$1^2A'$ transition of BeOH/D in the energy range 30300-32800 cm^{-1} revealed rotationally resolved spectra of several bending mode transitions. Ab initio calculations were used to guide the analysis of the spectroscopic data permitting unambiguous assignment of all spectral features. It was confirmed that the equilibrium geometry of the ground state is bent, and that the barrier to linearity lies below the zero-point energies for both BeOH and BeOD. A new Wiley-McLaren time of flight mass spectrometer was then incorporated into the existing spectrometer to provide the ability to mass separate anions generated from the laser ablation source. The $^1\Sigma^+ \leftarrow X\ ^1\Sigma^+$ ground state to dipole bound state electronic transition of AlO^- was studied by means of autodetachment spectroscopy. This studied benchmarked the capability to photodetach mass separated anions. Lastly, velocity – map imaging optics and a position sensitive detector were added to the spectrometer to finalize the construction of the photoelectron velocity – map imaging spectrometer. The previously unreported X $^1\Sigma^+$-X $^2\Sigma^+$ anion ground state to neutral ground state electronic transition of BeO^- was studied as a benchmark molecule for the spectrometer. The current results are presented here, along with a detailed report of the individual components of the spectrometer, and an overall evaluation of the performance of the spectrometer.

A Journey towards the Construction and Operation of a Photoelectron Velocity-Map Imaging Spectrometer

By

Kyle John Mascaritolo

B.S., Georgia Southern University, 2010

Advisor: Michael C. Heaven, Ph. D.

A dissertation submitted to the Faculty of the
James T. Laney School of Graduate Studies of Emory University
in partial fulfillment of the requirements for the degree of
Doctor of Philosophy
in Chemistry
2016

Acknowledgements

Acquiring a Ph.D. in any field of study is no trivial task and cannot be done alone. The ability it to collaborate is just one of many skills developed in the course of earning a Ph.D.

There are, of course, numerous individuals I should thank that have assisted me in developing as a graduate student. I, however, will only limit these acknowledgements to the individuals that I routinely think and talk about during every week in the lab.

I would like to thank my family for their support. Even though I have failed to incorporate them into my studies at Emory University, I know that they are extremely proud of my accomplishments, and for being the first in the family to achieve the educational level of Ph.D. Without their generosity, I would not have been able to graduate with my bachelors in chemistry from Georgia Southern University. Additionally, the constant knowledge that they are my safety net in life allowed me focus on my studies.

The entire Heaven group at Emory University deserves an acknowledgement for their numerous inputs towards the experiment. However, two individuals stand far above the rest: Dr. Jiande Han and Dr. Adrian Gardner. Jiande was one of the first individuals I encountered at Emory University. Over the years, being desk neighbors allowed for me to ask him all the stupid questions I was too afraid for Dr. Heaven to know about. Educating me, frequent chatting breaks, and lending a hand in lab gives me the pleasure for calling Jiande a friend. Adrian was my lab partner for two years. Together, we

designed and constructed a vast majority of the photoelectron velocity – map imaging spectrometer. His intense work ethic and even more intense love of spectroscopy definitely rubbed off on me. Without his enthusiasm fueling me, I would not be the spectroscopist I am today. I am grateful for the two years we had working eight days a week. He was not only my lab partner, but also a close friend.

The construction of the spectrometer would not have been possible without the skills of Cody Anderson and Horace Dale of the Physics Machine Shop at Emory University. Their incredible work machining metal parts for the spectrometer were always above what was expected. Their advice on better designs for the components of the spectrometer greatly improved its ease of use, and helped improve my own skills in the designing and constructing of several components myself (and doing it correctly the first time). I thank both of them for their kindness, patience, and understanding towards helping me.

I would also like to acknowledge Joseph Czekner (Joe), a graduate student at Brown University under the advisement of L.S. Wang. I was fortunate enough to be able to visit Joe at Brown to pick his brain on how he records images on his spectrometer. Without his sage advice, I would not have been able to effectively troubleshoot our spectrometer to understand the necessary modification needed to record perfect images.

It goes without saying that the members of my committee deserve acknowledgement. In addition to being my favorite lectures at Emory University, their guidance has help me journey towards earning a Ph.D. My advisor, Dr. Michael Heaven, above all, deserves the largest acknowledgment. It is no secret that I, and the entire Heaven group, considers him the ideal advisor. His kindness, patience, humor,

willingness to help, and his understanding of stress, frustration, and annoyance in lab make us proud to brag about him to prospective students. I thank him.

Contents

Listing of Figures

Listing of Tables

Chapter 1

A Journey towards the Construction and Operation of a Photoelectron Velocity-Map Imaging Spectrometer

The main focus for the completion of my Ph.D. was to construct an apparatus capable of photoelectron velocity-map imaging spectroscopy[1-3] in order to study the electronic structure and bonding of beryllium containing species. This apparatus was to be modeled after the slow electron velocity-map imaging (SEVI) apparatus of Dr. Danial Neumark at the University of California, Berkeley.[1] Though this was nearly achieved, many steps were taken in the evolution of the apparatus's construction. Along the way, increasingly difficult projects were performed in order to not only benchmark the capabilities of the apparatus, but also develop the experimental and spectroscopic skills needed to execute the notoriously challenging task of velocity-map imaging electrons.

Outlined in this chapter will be a description defining the choice for using photoelectron velocity-map imaging spectroscopy as a means to study beryllium containing species, particularly beryllium and beryllium oxide clusters (Be_n and Be_nO_m, respectively), and their anionic forms. Following this are introductions to each of the four projects that I completed at Emory University. A primary focus in these introductions will be placed on the significance of the projects with regard to the phases

of constructing the photoelectron velocity-map imaging experiment and bringing it to a state of operation. The secondary focus is on the general advancement in understanding the chemistry of the species studied. Lastly, a description of the structure of the remaining body of this dissertation is presented.

1.1 Photoelectron Velocity-Map Imaging Spectroscopy: Application to the Study of Beryllium Containing Clusters

The evolution of bonding within molecular metal clusters and metal – oxide clusters as they grow in size is of great interest.[4-10] Fundamental questions regarding these clusters are: how do their properties develop as a function of cluster size, and at what size do clusters exhibit the properties of bulk metal? Properties that can be measured in the gas phase that can provide answers to these questions include the ionization energy, bond energies, geometric structures, and the energy gap between the highest occupied molecular orbital (HOMO) and the lowest unoccupied molecular orbital (LUMO).

Be_n and Be_nO_m are a prime example to investigate spectroscopically to probe the questions regarding cluster to bulk metal properties. In addition to these species having relatively few electrons, making them suitable for high level *ab initio* theories,[7,11-34] the light masses of beryllium and oxygen make the smaller clusters candidates for rotationally resolved spectroscopies, allowing for geometric analysis.[35-39] Though many theoretical predictions have been made on Be_n clusters, only the dimer has been studied experimentally.[35,36,38] There is a lack of data for any of the small Be_nO_m clusters.[16,17,39,40]

The properties of the clusters listed above can usually be measured via standard spectroscopy techniques for cluster sizes containing just a few atoms. However, complication can arise as cluster size increases.

When trying to probe the ground state directly through techniques involving absorption spectroscopy, creating enough number density of a metal containing species in the gas phase is typically difficult with standard technique such as Knudsen oven heating, laser ablation, or electrical discharge sources. Additionally, since these sources are generally p\species non-selective, absorption of undesired species is unavoidable in many cases. Mass selected methods can avoid this problem, but this requires the species to be charged. Other techniques, such as laser induced fluorescence, that measure the electronic structure of the ground state indirectly via excitation to excited states also struggle when applied to large clusters. As cluster sizes grow, the density of excited states can become overwhelming making state assignment difficult. Resonance enhance multiphoton ionization is a technique that can be mass selective when coupled with a mass spectrometer, but not only is it hindered by the density of states problem, but large clusters are prone to dissociation through multiphoton processes due to their tendency to have large photon absorption cross-sections. Dissociation of clusters can result in misleading signals from detection of the smaller cluster fragments.

Probing the ground state of a neutral cluster by use of photodetachment spectroscopy[41,42] on its anionic form provides a solution to the problems listed above.[4,6,42-45] This method can be mass selective since the starting species are charged, allowing for the use of electric fields for mass separation. Additionally, charged particles can be trapped with electric fields. Trapping allows for both the accumulation of sample,

increasing number density, and the cooling of the internal states of the anions.[46-49] With cold anions, this method also allows for direct measurements of ground state properties of the neutrals, since most of the anion population will be in its ground state. Specifically using photodetachment velocity-map imaging spectroscopy[1] can provide a wealth of information such as the electron affinity of the neutral, the molecular symmetry of the electronic states of both the neutral and anion, the HOMO – LUMO gap, and, with a resolution of only a few wavenumbers, the vibrational frequencies of both species.[50-57]

1.2 The First Stage - AlAr

Before the proposed research on beryllium containing clusters began, sub-projects were completed in the overall construction of the photoelectron velocity-map imaging spectrometer. The first project that I completed was a study on the aluminum – argon (AlAr) van der Waals complex (See Chapter 2). The experimental setup is shown in Figure 1 and is designated as the first stage in construction of the photoelectron velocity-map imaging experiment. This project was designed to primarily test the capabilities of the R.M. Jordan PSV C-211 supersonic pulse valve coupled with laser ablation, and secondarily to test the overall vacuum and laser systems. The vacuum and laser systems used in this stage will not be discussed in any great detail here.

In order to create anions in a supersonic jet expansion for the final stage, it is advised to use a short gas pulse duration, on the order of tens of microseconds or shorter.

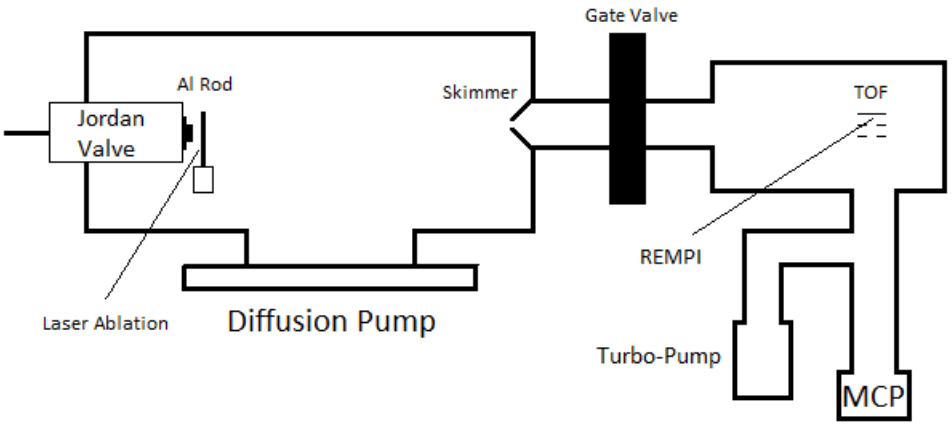

Figure 1: Stage one towards the photoelectron velocity-map imaging spectrometer. TOF: Time of flight. MCP: Microchannel plates. For specific experimental details refer to Chapter 2. This diagram is not drawn to scale.

A short pulse duration will avoid detachment of the anions from the collisional cooling process within a supersonic jet expansion. Detachment of an anion can occur if they undergo too many collisions with the carrier gas before expanding into the hard vacuum of the source chamber. Generally, the longer the gas pulse the greater the number of collisions. The Jordan valve has been found to be able to operate with a pulse duration of 40 – 60 μs.

Another desire for the formation of anions in the final stage is the production of internally cold anions. Cold anions, like most molecules, provide much simpler spectra to analyze. However, creating internally cold anions is quite difficult due to the collisional detachment mentioned above. Collisions are needed to transfer internal energy from the anion to the carrier gas, but too many will eventually detach the electron. It is a double edged sword that requires much time and experimentation to discover the source design and operating conditions that will produce cold anions.

The AlAr complex was chosen to test the cooling performance of the Jordan valve and the laser ablation setup coupled to it. AlAr is a van der Waals complex, bound only by the weak intermolecular attractions generated from the mutually induced polarization of the valence electrons of each atom.[58,59] van der Waals interactions are extremely weak compared to covalent and ionic bounds as described in any general chemistry textbook. For example, the dissociation energy[60] of AlO is 42500 ± 160 cm^{-1} whereas the dissociation energy[59] of AlAr is only 122.4 ± 4.0 cm^{-1}. This shallow potential energy curve of AlAr is limited to a relatively few number of bound states and can only be formed if the internal temperature of the complex is very low. If the complex is too

"warm" it will auto-dissociate. The 122 cm^{-1} dissociation limit equates to a temperature of 85 K ($T=\frac{E}{k}$).

In the source of the first stage, not only was the complex successfully made, but there was no evidence of vibrational hot bands in the recorded spectra. The harmonic vibrational frequency of the ground state of AlAr is $\omega_e = 31.6$ cm^{-1},[59] which would be populated at a vibrational temperature of about 22 K. Therefore, it was concluded that the source design in the first stage was capable of creating molecules at low internal temperatures. The overall source design was retained throughout each of the following stages. (A drawing of the source used in the final stage is shown later in Figure 5. This design is largely based on the design used to study AlAr in the first stage with only cosmetic changes made to fit the experimental needs for the final stage.)

1.3 BeOH in the First Stage

Once it was established that the first stage was suitable for molecular spectroscopy of cold molecules, our attention was turned to study a molecule containing beryllium. Beryllium containing molecules have been the subject of much research in order to understand the unusual bonding characteristics of the beryllium atom.[7,12,18-24,28,30-35,38,39,61-87] The beryllium dimer is one such molecule that has received much attention, being a prime example of the abnormality of beryllium bonding. Molecular orbital theory predicts a formal bond order of zero for the dimer, however it has been shown experimentally to be bound by $D_e = 0.115$ eV (927 cm^{-1}).[35] While this binding energy is not on the order of typical covalent or ionic bonds, it is considerably higher

than the binding seen in van der Waal complexes like AlAr mentioned earlier, stimulating investigation. Theories beyond first order approximations are need to accurately predict the effects of electron correlation and the participation of the 2*p* orbitals in bonding responsible for beryllium dimer bond.[18,27,28,30,32,36-38,75,82,88-95]

Relevant to the research presented here (Chapter 3) is the bonding trends of the group IIA metal hydroxides. The heavier metal hydroxides (Ba, Sr, Ca, Mg) have been shown to exhibit formal ionic bonding giving rise to a linear ground state geometry.[96-107] However, BeOH displays signs of covalency in its bonding through a bent equilibrium geometry,[97,98,108] partially due to beryllium's high ionization energy and its small radius. This geometry was predicted to have a barrier to linearity of only 136 cm^{-1},[97,98,108] but there lacked experimental data to support these findings.

The data reported in Chapter 3 reveals that the equilibrium geometry of the ground state of BeOH is in fact bent, but with a barrier to linearity lying below the vibrational zero-point energy. Additionally, complimentary data for BeOD is presented. The rotational temperature of the experiment was found to be only 8 K, further demonstrating the Jordan valve's ability to produce cold molecules.

1.4 Anions and Photodetachment in Stage Two

The second stage of the experiment was a huge leap toward photoelectron velocity-map imaging. This stage was used to master the difficult task of creating and mass selecting anions, and then photodetaching them. The difficulty in the creation and mass selection of anions, or any changed particles, comes with the fact that the two

processes are coupled. One cannot know if charged particles are being produced by the source if the mass spectrometer is not functional, as well as one cannot know if the mass spectrometer is functional if charged particles are not being produced. The difficulty in photodetaching anions is in the multidimensionality of the task. This process is a function of four variables: the spatial and temporal overlapping of both the anions and the incident photons (laser). Unless the overall structure of the spectrometer is carefully designed and built, this process can be extremely challenging.

A few additional features to stage one were needed to achieve the desirable experimental conditions needed for photodetachment spectroscopy. The most critical of these features was the ability to mass select anions generated from the source. There were no modifications done to the overall source design of stage one since there are numerous previously reported experiments involving the generation of anions through laser ablation. Only a few are cited here.[6,42,109] However, the Wiley-McLaren time of flight mass spectrometer (WM-TOFMS) in the experimental setup of stage one was located in a position much too far from the source to achieve the number densities needed for photodetachment. Additionally, the length of the drifting region was too short to mass select heavy ions.

A diagram of the second stage is shown in Figure 2. The chamber that houses the source of the second stage (furthest to the left) is identical to stage one (Figure 1), but some modification were made to the equipment inside. It should be noted that the view of the source chamber in Figure 1 is from the side, while the view in Figure 2 is from the top. A new WM-TOFMS[110] was constructed and set in a position perpendicular to the Jordan valve/laser ablation setup. The Jordan valve had to be moved to achieve this orientation

as can be seen in Figure 2. The mass spectrometer was comprised of three electrodes: a repeller, an extractor, and a ground. It is shown in Figure 3. Each stainless steel electrode was constructed from two 3 inch outer diameter plates with a 1 inch diameter hole in each plate. A 95% transparent copper mesh (Industrial Netting) was sandwiched between each plate over the 1 inch hole. The plates were held together with six 0-80 bolts countersunk into the plates to provide a flat surface. All three electrodes were supported by four alumina tubes with 0-80 threaded rods running inside and separated by 1/2 inch length alumina spacers that slipped over the alumina tubes. The whole mass spectrometer assembly was supported by two aluminum plates 4.5 inches in diameter that rested on a 6 mm rod cage system. Nuts at the ends of the 0-80 rods held the whole assembly together. The WM-TOFMS had to be confined within a steel structure with a small hole for the jet expansion in order to maintain a low enough pressure for the charged mass spectroscopy plates to function without electrically discharging.

Two new chambers replaced the last chamber in stage one. The first of the two chambers (middle chamber in Figure 2) ultimately was only used in this stage to increase the time of flight distance from the source to the photodetachment region. The resolution of the mass spectrometer was $t/\Delta t = 690$. This resolution was able to resolve anions differing by 1 mass to charge ratio unit (m/z) at a m/z up to at least 59 (AlO_2^-). Anions with higher m/z were not investigated with optimal focusing of the mass spectrometer. The last chamber contained the photodetachment region and the detector, along with electrodes to produce a retardation field needed for the study of autodetachment of dipole bound states of AlO^- (See Chapter 4).

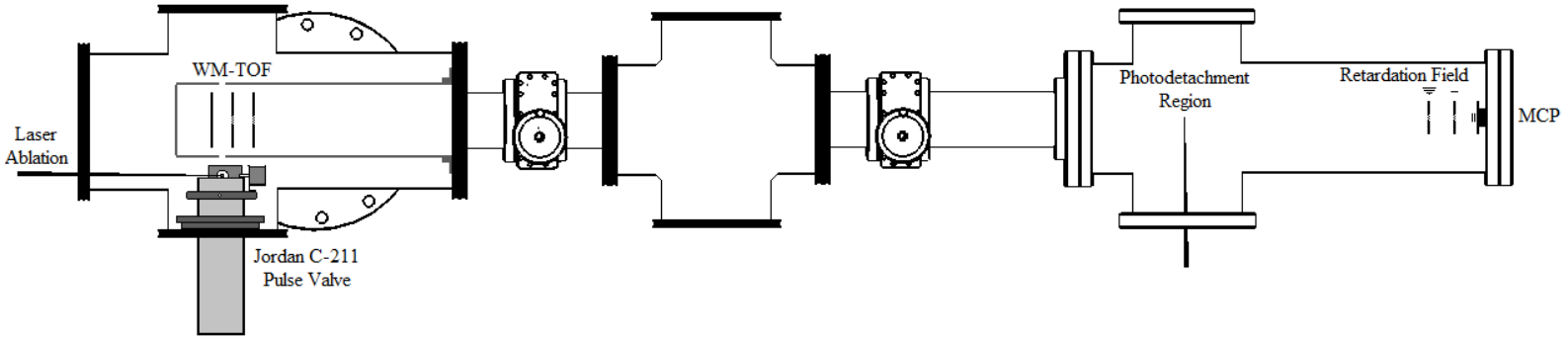

Figure 2: Stage two towards the photoelectron velocity-map imaging spectrometer. WM-TOF: Wiley-McLaren time of flight, MCP: Microchannel plates. For specific experimental details refer to Chapter 4. This diagram is drawn to scale.

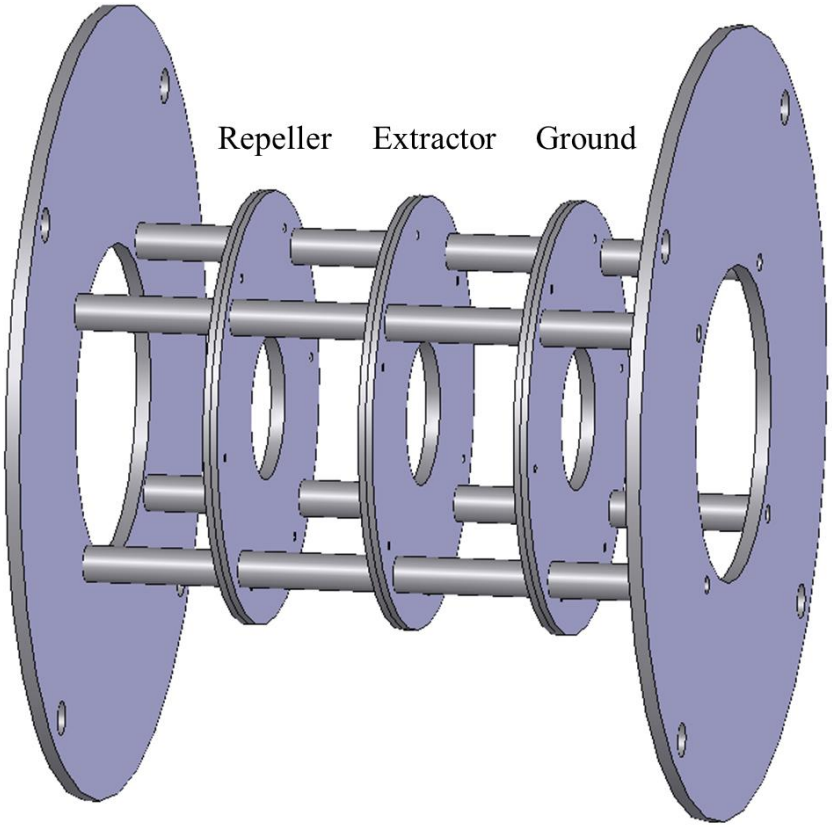

Figure 3: Drawing of the Wiley-McLaren time of flight mass spectrometer used in the second and final stages.

1.5 The Final Stage

As was described in the last section, the second stage was able to produce mass selected anions and photodetach them. Though photoelectrons were being produced, electrons were not being detected; the neutrals remaining after detachment were instead detected (See Chapter 4). Several additions to stage two were needed in order to detect electrons with the velocity-map imaging technique. The photoelectron velocity-map imaging spectroscopic technique will be discussed in detail later in Chapter 5. This section will provide the reader with a brief description of the technique to compliment the extensive discussion of the hardware and design of the photoelectron velocity-map imaging spectrometer given here. Additionally, a sub-section describing the necessities of a well-built velocity-map imaging optics setup is included.

Photoelectron velocity – map imaging spectroscopy is a variant of photodetachment spectroscopy. Mass selected anions in the gas phase are intersected by a fixed frequency laser above the detachment threshold of the anion. Detached electrons from the anions will have quantized amounts of kinetic energy described by

$$h\upsilon = EA + E_{Binding} + eKE \qquad \text{(Eq. 1)}$$

where hν is the photon energy, EA is the electron affinity of the neutral (detachment threshold of the anion), $E_{Binding}$ is the internal state energy of the neutral after photodetachment, and eKE is the kinetic energy of the detached electrons. Based on Eq. 1, it can be seen that $E_{Binding}$ and eKE are correlated. Since EA is constant for a species, the quantization of the internal states of the neutral species dictates that the kinetic energy of the detached electrons must also be quantized.

The spatial distribution of detached electrons traveling away from the anions with various quantized kinetic energies (velocities) are known as Newton spheres. The unique radii of these spheres are related to the quantized eKEs, while the anisotropy of the distribution of the electrons about the outer surface of the spheres encodes the angular momentum of the photoelectrons, and some molecular dynamics. The degree of anisotropy can be measured from the photoelectron angular distribution (PAD), described by

$$I(\theta)=\frac{\sigma}{4\pi}(1+\beta P_2(\cos\theta)) \qquad \text{(Eq. 2)}$$

where σ is the total photodetachment cross section, $P_2(\cos\theta)$ is the second Legendre polynomial, and β is the anisotropy parameter having values between -1 and 2.

After photodetachment, the Newton spheres are accelerated towards and focused onto a position sensitive detector by an electrostatic lens in a process called velocity – map imaging. Velocity – map imaging maps charged particles with similar velocities (kinetic energies) onto a common spot a fixed distance away. In the case of photoelectron velocity – map imaging spectroscopy, electrons with the same quantized amount of kinetic energy are detected on a spatially different area on the position sensitive detector from all other electrons with different kinetic energies. Furthermore, the intensity pattern produced upon the accumulation of tens of thousands of electron impacts on the detector will reveal the PAD. The accumulation of electrons, producing an image, is recorded with a charged couple device (CCD) camera.

Figure 4 shows the final stage with the additions to the second stage needed to effectively detect electrons with photoelectron velocity – map imaging spectroscopy.

The source chamber was unaltered from the second stage. It proved to be well-designed for producing anions. A drawing of the source used is shown in Figure 5. The Jordan valve was mounted through a 3.5 inch hole drilled in the center of a steel flange. It was held in place by the force generated from compressing an o-ring around the valve with an aluminum plate fitted around the valve. Bolts tightened into tapped holes on the vacuum side of the flange provided the compressing force. This o-ring was also provided a vacuum seal between the surfaces of the valve and the flange it was mounted in. An ablation block similar to those used elsewhere[111] was mounted onto the front of the valve through a custom plate. A stepper motor underneath the valve provided rotational motion for a metal rod target. This motor was also mounted on a rail and car system to provide vertical motion of the rod via a second stepper motor. The second stepper motor was mounted perpendicular to the first and was attached to it with a string. As the motor spun, the string would wine on the shaft of the motor, pulling the other motor vertically. These motions allowed for laser ablation of a fresh surface on the target for each event cycle of the experiment.

An Einzel lens and four sets of deflector plates were added in the second chamber to focus and guide the anions into the center of the velocity-map imaging (VMI) optics. A drawing of the Einzel lens is shown in Figure 6**.** This was modeled after the Einzel lens example potential array given in the SIMION 8.0 software package.[112] The dimensions of the original model from SIMION were doubled for ease of construction and use. Each part of the lens was made from a stainless steel tube with an outer diameter of 24 mm and an inner diameter of 18 mm. The lengths of each part were 14,

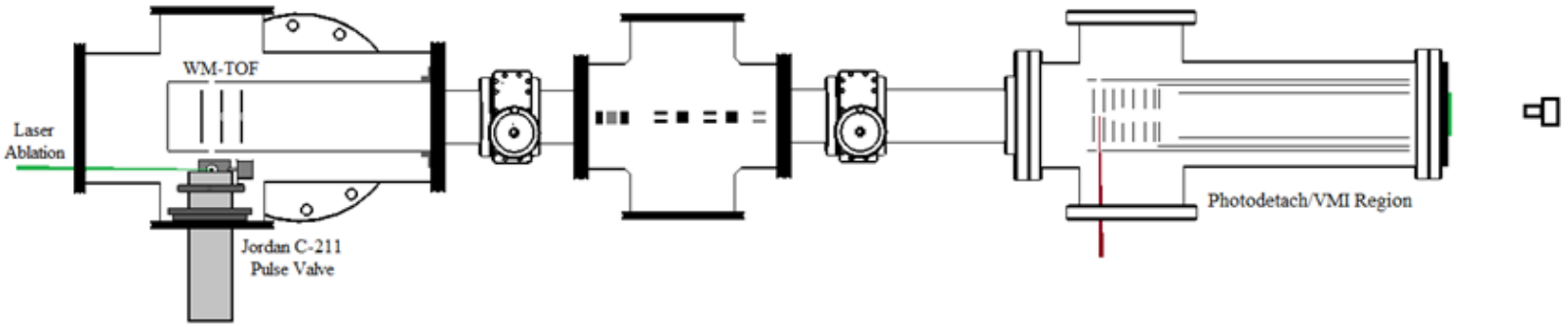

Figure 4: Schematic of photoelectron velocity-map imaging spectrometer, the final stage. WM-TOF: Wiley-McLaren Time of Flight, VMI: Velocity-Map Imaging. This figure is drawn to scale.

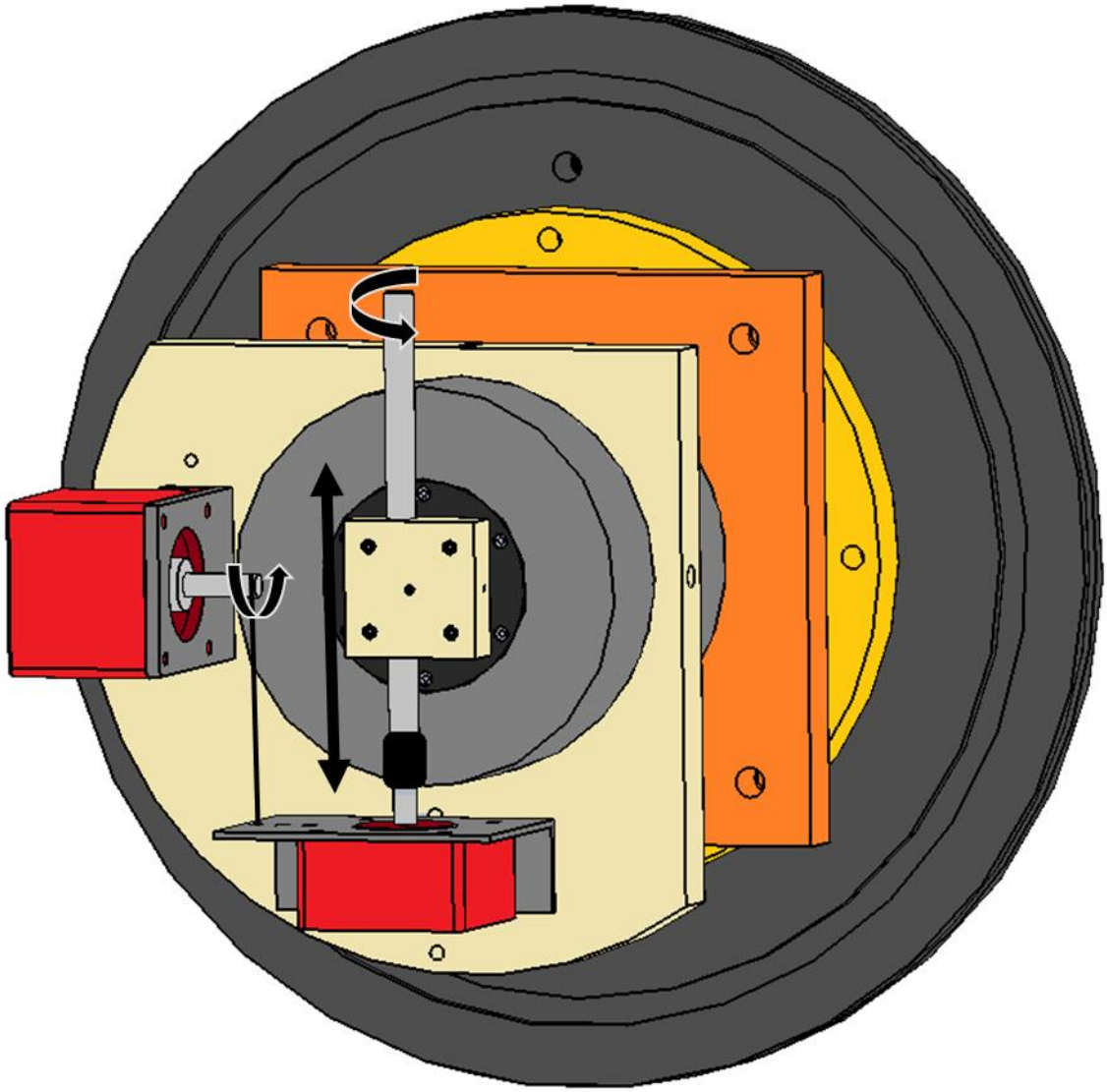

Figure 5: Drawing of the Jordan valve/laser ablation anion source (Color). Flange (dark grey), O-ring compression plates (yellow and orange), Stepper motor support ring (Tan), Stepper motor (red), Jordan valve (grey), Custom face plate for Jordan valve (black), Ablation block (Tan).

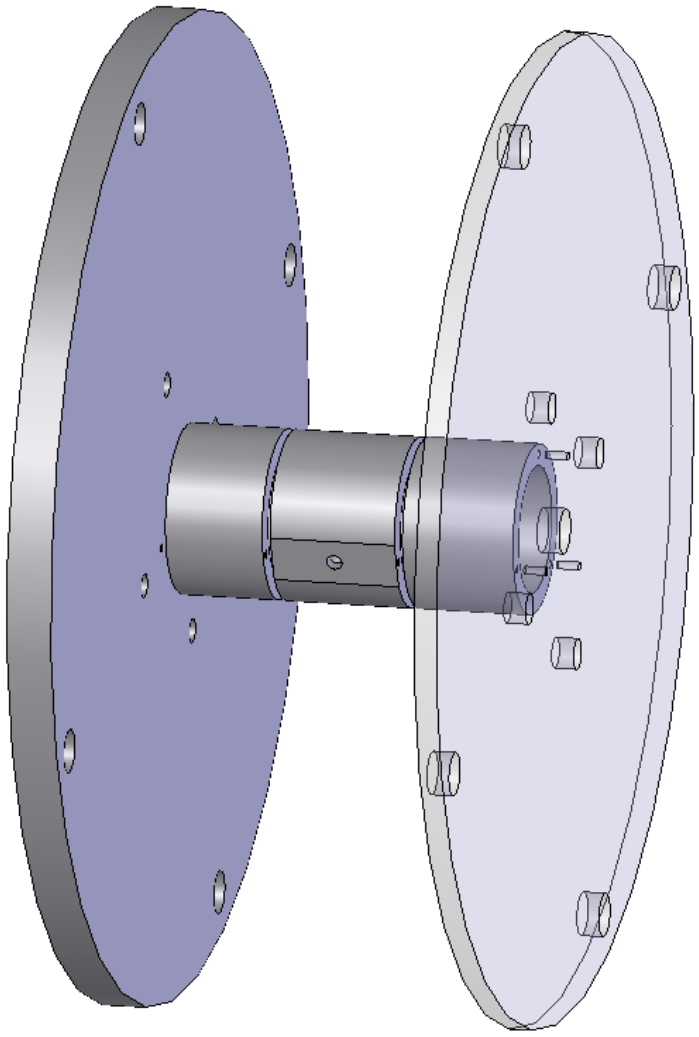

Figure 6: Drawing of Einzel lens. The end support plate has been made transparent for clarity.

18, and 16 mm, following the flight path of the anions through the lens. The parts were separated from each other with 3/32 inches diameter ceramic balls. The lens was held together by compressing the tubes and balls with 8-32 threaded rods and nuts attached to support plates on either side of the lens (rods not shown in Figure 6). The assembly was mounted on a similar 6 mm cage system as the WM – TOFMS mentioned in the previous section. A negative potential was applied only to the center ring of the lens for focusing conditions. The outer rings were kept at ground.

Two sets of the deflector plates were used to guide the anions into the VMI optics. One of these assemblies is shown in Figure 7. Each deflector plate was made of a square inch stainless steel plate 1/32 in thick and was attached to an aluminum L-shaped support via 4-40 bolts, electrically separated by plastic washers. Each deflector plate support was mounted onto an overall assembly support, positioned so that each deflector plate was separated by a distance of one half inch. The two sets of plates were positioned orthogonal to each other to provide guidance of the anions in two dimensions (vertical and horizontal). One plate of each set was grounded while the opposite plate was connected to a voltage source. The assemblies were also mounted on a similar 6 mm cage system as the WM – TOFMS mentioned in a previous section. Two entire assemblies were needed in order to be able to both angle and translate the anions along their flight path. A fifth set of deflector plates was used as a mass gate.

The most important additions to the final stage were the VMI optics and the imaging detector. The VMI optics were modeled after León and Wang.[2] The geometry of the individual optic plates within the lens were kept identical to those of León and Wang, expect the outer diameter of the plates, which was increased to 4.5 inches to be

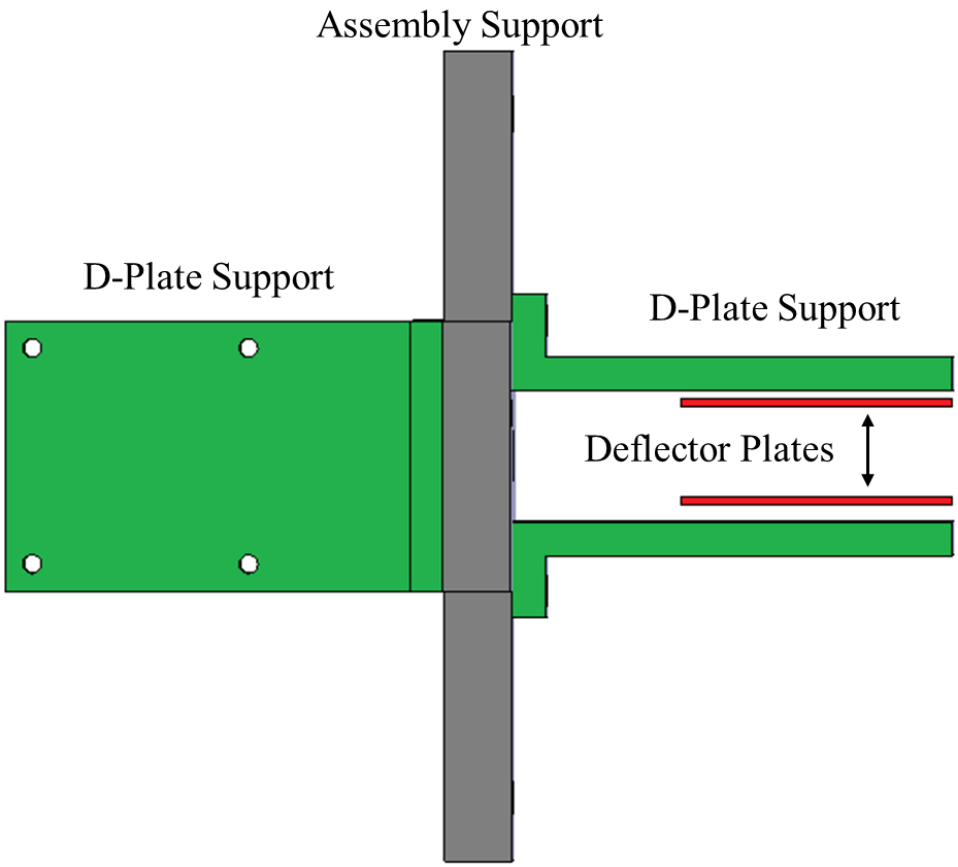

Figure 7: Drawing of a deflector plate assembly (Color). Deflector Plates (red), Deflector Plate Support (D – Plate Support, green), Assembly Support (grey).

compatible with an existing mounting system within the chamber. The plates were also made of 304 stainless steel instead of gold plated, oxygen free copper. 304 stainless steel was used instead for its rigidity, but should still produce similar results to the copper plates used by León and Wang. The copper plates were gold plated to increase the work function of the VMI optics. This allows for the use of higher energy photons for detachment processes while avoiding electron emission from the plates themselves. Gold plating of the 304 stainless steel plates is planned for future experiments. The VMI optics were mounted on four ¼ inch diameter alumina tubes with 8-32 aluminum threaded rods running inside them. They were separated by Teflon™ spacers cut to the same dimensions as those reported by León and Wang.[2] The alumina tubes and aluminum rods were then mounted onto a support ring, which was supported by threaded rods screwed into a flange on axis with the molecular beam.

Once photoelectrons were produced within the lens, they were accelerated down a drift region to the detector 66 cm away (PHOTONIS USA, INC. 75mm Chevron stacked microchannel plates (MCP) with a fiberoptic phosphor screen with P47 phosphor). This region was shielded from external electric and magnetic fields by layers of mu-metal. Electrons impacting the detector were recorded with a CCD camera (Physimetrics UI-2230SE-M-GL, 1024x768). The camera was mounted 60 cm from the detector screen, housed in a black-painted aluminum tube bolted into the flange of the detector. This mounting system allowed for the camera to be routinely positioned in the same orientation with respect to the detector, and to shield the camera from room light. A 1 inch focal length spherical lens was placed 1 inch from the CCD array of the camera.

Electrons impacting the detector were discriminatively detected from all other charged particles by pulsing the voltage (gain) on the MCPs only when the electrons arrived at the detector. Individual electron distributions from each cycle of the experiment were recorded and summed over several tens of thousands of cycles to produce an image. The final image was saved using the imaging software developed by Suits.[113] Transformation of the image from velocity space to energy was done using the Polar Onion Peeling (POP) technique[114] and Maximum Entropy Velocity Legendre Reconstruction (MEVELER).[115] The illumination of the screen from electron or anion impacts could also be monitored with a photomultiplier tube positioned off axis from the camera. This form of detection produced the TOF-MS spectrum, and was extremely useful in the optimization of anion and photoelectron production. The repetition rate of the experiment was 10 Hz.

1.6 Developing High Quality Velocity-Map Imaging Optics

Two criteria must be met to achieve the absolute best resolution from a VMI setup: the electrons must be focused well by the VMI optics onto the detector, and the trajectories of the electrons as they travel to the detector must only be effected by *uniform* potentials within the VMI optics. These two criteria are extremely difficult to achieve. Over a year was spent on attempting to achieve these criteria in the final stage, but they were not completely met. Resolution in the following text refers to the pixel width of features in a raw image.

Focusing the electrons well by the VMI optics onto the detector is a function of three primary conditions: the focal plane of the VMI optics must be exactly at, and exactly the same as, the plane of the detector, the interaction volume within the VMI optics must be as small as possible, and the interaction volume must be at the axial center of the VMI between the repeller and extractor electrodes (the first two plates). Meeting each condition by itself is challenging, but what becomes even more problematic is that the negative effects brought upon the resolution of the spectrometer by not meeting one of these conditions is identical in appearance on the final image as not meeting all of the conditions. For example, if the focusing conditions of the VMI are perfect, but interaction volume is too large (~ >1 mm diameter sphere) the image will be blurry (increased pixel width). However, if the opposite is true, the interaction volume is a near point source, but the focusing of the VMI is far from perfect, the image will also be blurry. Recording the sharpest image possible requires iteratively adjusting the above three conditions until the resolution no longer improves.

Creating uniform electric fields within the VMI optics is also essential to the resolution of an image. Under the assumption that the criteria in the immediate above text are met, uniform potentials within the VMI will map the trajectories of the electrons onto the detector as perfect spheres. This in turn will display ring structures as the electron spheres are flattened from impacting the detector. Perfectly circular images are needed when transforming an image in velocity space to energy space.[114-117] Any non-circularity in the image created from non-uniform potentials will degrade the resolution since quadrant symmetrizing signal on different radii will broaden a ring.

There are a few conditions that can cause non-uniformity of the potentials within the VMI. The electric fields within the optics must be as close to symmetrical about the center axis as possible. Any defects will break the symmetry and map electrons with the same velocity vectors onto different radii. The surface quality and flatness of the individual plates is very important in maintaining a uniform electric field between each plate. Any defects such as scratches, chips, dirt and oil, or curvature can degrade the electric field quality. Ideally, the finish on the electrodes should be mirror like. Another factor is the degree of parallelism of each plate with respect to every other plate. If all of the plates are not parallel to each other the electric field between them will be asymmetric. Lastly, the VMI optics must be parallel to the detector. The electron spheres created within the VMI optics must impact the detector head on. If there is any drift from the center axis of the experiment, the image will become elliptical.

The effects of non-uniform potentials differ from the effects the previous conditions cause on an image. Typically, misshaping of the image, drop in intensity within large sections of the image, and pockets of blurriness rather than an overall blurriness of the image are all indications that the electric potentials within the VMI optics are not uniform.

To demonstrate the importance of symmetrical images, Figure 8 shows an image of the photodetachment of the sulfur atomic anion, S^-. This image is the highest resolution image of any species recorded on this spectrometer. The energy resolution of this image after transformation using the Polar Onion Peeling technique[114] is 18%. The deconvoluted spectrum is shown in Figure 9 (Top). An energy resolution of 18% is about a factor of 35 worse than the experimentally proven best resolution achievable of 0.53%

for this VMI design.[2] One of the biggest contributors to the low resolution is the non-circularity of the image, most easily seen in the bottom right quadrant. The radii of the rings are smaller in this quadrant compared to the rest of the image. If the same image is then transformed only using the top left quadrant, the resolution is improved to ~5%. The deconvoluted spectrum is shown in Figure 9 (Bottom). While this is still an order of magnitude worse than the best resolution possible, it demonstrates the importance of having circular images.

The final stage is being used to study the photodetachment of BeO^- (See Chapter 5). Preliminary data has measured the previously unknown electron affinity of BeO and the $\Delta G_{1/2}$ vibrational interval of BeO^- yielding results that are in great agreement with theoretical predictions.

1.7 Structure of the Remaining Dissertation

The remaining body of this dissertation is broken up into four chapters. Chapter 2 contains the published work on the aluminum – argon (AlAr) van der Waals complex,[118] Chapter 3 details the spectroscopy of the BeOH molecule,[119] and Chapter 4 presents the autodetachment of dipole bound states of AlO^-.[120] The content in these chapters is identical to the published work with one exception. Figure 4 of Chapter 4 has been replaced with the correct figure as detailed in the erratum[121] to the publication. Lastly, Chapter 5 gives a brief overview of photoelectron velocity-map imaging spectroscopy, reports the unpublished work on the photoelectron velocity-map imaging spectroscopy of BeO^-, and describes the experimental details and performance of the final stage.

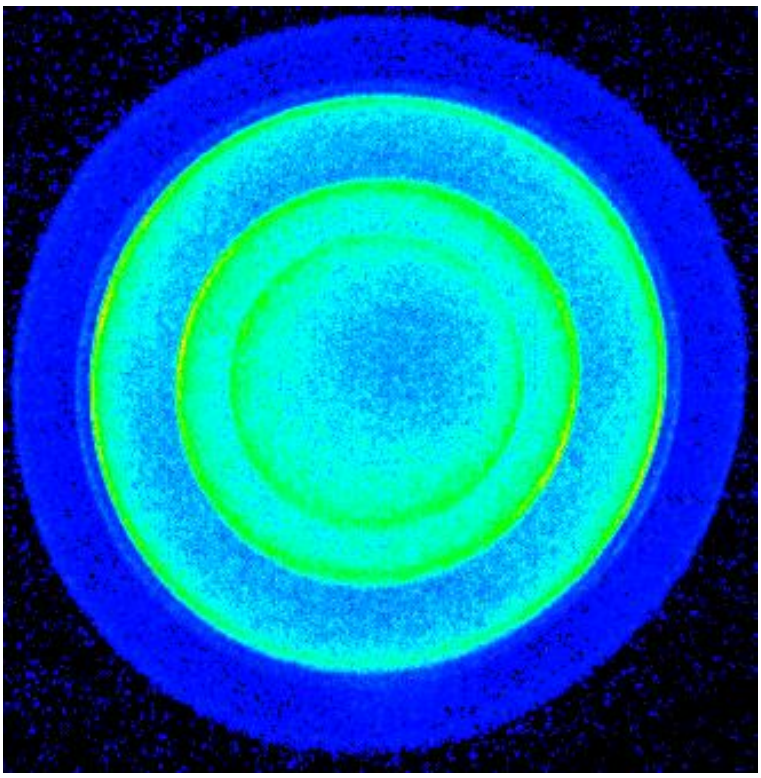

Figure 8: Photoelectron velocity-map image of the sulfur atomic anion, S^-. For experimental details of this image refer to Chapter 5.

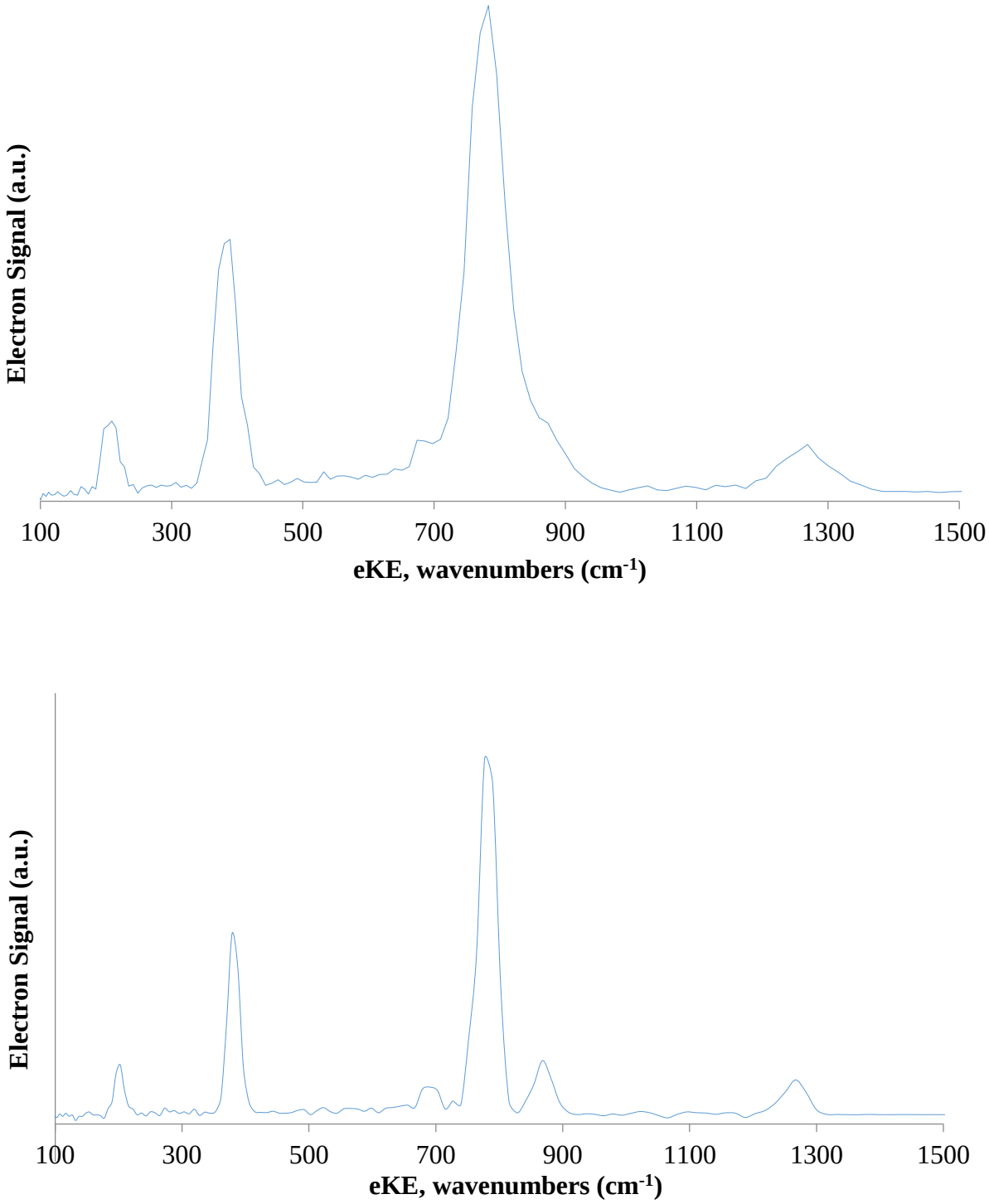

Figure 9: (Top) Deconvoluted image of S^- using the entire image shown in Figure 4. (Bottom) Deconvoluted image of S^- using only quadrant II of the image shown in Figure 4.

1.8 References to Chapter 1

(1) Neumark, D. M. Slow Electron Velocity-Map Imaging of Negative Ions: Applications to Spectroscopy and Dynamics. *Journal of Physical Chemistry A* **2008**, *112*, 13287-13301.

(2) Leon, I.; Yang, Z.; Liu, H. T.; Wang, L. S. The design and construction of a high-resolution velocity-map imaging apparatus for photoelectron spectroscopy studies of size-selected clusters. *Review of Scientific Instruments* **2014**, *85*, 12.

(3) Eppink, A.; Parker, D. H. Velocity map imaging of ions and electrons using electrostatic lenses: Application in photoelectron and photofragment ion imaging of molecular oxygen. *Review of Scientific Instruments* **1997**, *68*, 3477-3484.

(4) Wang, L. M.; Wang, L. S. Probing the electronic properties and structural evolution of anionic gold clusters in the gas phase. *Nanoscale* **2012**, *4*, 4038-4053.

(5) Jena, P.; Castleman, A. W. Clusters: A bridge across the disciplines of physics and chemistry. *Proceedings of the National Academy of Sciences of the United States of America* **2006**, *103*, 10560-10569.

(6) Thomas, O. C.; Zheng, W. J.; Xu, S. J.; Bowen, K. H. Onset of metallic behavior in magnesium clusters. *Physical Review Letters* **2002**, *89*, 4.

(7) Heaven, M. C.; Merritt, J. M.; Bondybey, V. E.: Bonding in Beryllium Clusters. In *Annual Review of Physical Chemistry, Vol 62*; Leone, S. R., Cremer, P. S., Groves, J. T., Johnson, M. A., Eds.; Annual Review of Physical Chemistry; Annual Reviews: Palo Alto, 2011; Vol. 62; pp 375-393.

(8) Hakkinen, H.; Moseler, M.; Landman, U. Bonding in Cu, Ag, and Au clusters: Relativistic effects, trends, and surprises. *Physical Review Letters* **2002**, *89*, 4.

(9) Raghavachari, K.; Logovinsky, V. STRUCTURE AND BONDING IN SMALL SILICON CLUSTERS. *Physical Review Letters* **1985**, *55*, 2853-2856.

(10) Morse, M. D. CLUSTERS OF TRANSITION-METAL ATOMS. *Chemical Reviews* **1986**, *86*, 1049-1109.

(11) Lesiuk, M.; Przybytek, M.; Musial, M.; Jeziorski, B.; Moszynski, R. Reexamination of the calculation of two-center, two-electron integrals over Slater-type orbitals. III. Case study of the beryllium dimer. *Physical Review A* **2015**, *91*, 12.

(12) Sheng, X. W.; Kuang, X. Y.; Li, P.; Tang, K. T. Analyzing and modeling the interaction potential of the ground-state beryllium dimer. *Physical Review A* **2013**, *88*, 6.

(13) Mentel, L. M.; Baerends, E. J. Can the Counterpoise Correction for Basis Set Superposition Effect Be Justified? *Journal of Chemical Theory and Computation* **2014**, *10*, 252-267.

(14) Sulka, M.; Labanc, D.; Kovac, M.; Pitonak, M.; Cernusak, I.; Neogrady, P. Ab initio study of the stability of beryllium clusters: accurate calculations for Be2-6. *Journal of Physics B-Atomic Molecular and Optical Physics* **2012**, *45*, 12.

(15) Ascik, P. N.; Rugango, R.; Simmonett, A. C.; Compaan, K. R.; Schaefer, H. F. The Beryllium Pentamer: Trailing an Uneven Sequence of Dissociation Energies. *Chemphyschem* **2012**, *13*, 1255-1260.

(16) Zhou, Z. J.; Li, Y. Z.; Zhuang, J.; Wang, G. J.; Chen, M. H.; Zhao, Y. Y.; Zheng, X. M.; Zhou, M. F. Formation and Characterization of Two Interconvertible Side-On and End-On Bonded Beryllium Ozonide Complexes. *Journal of Physical Chemistry A* **2011**, *115*, 9947-9953.

(17) Ostojic, B.; Jensen, P.; Schwerdtfeger, P.; Assadollahzadeh, B.; Bunker, P. R. The predicted infrared spectrum of the hyperberyllium molecule BeOBe in its (X)over-tilde(1)Sigma(+)(g) and (a)over-tilde(3)Sigma(+)(u) electronic states. *Journal of Molecular Spectroscopy* **2010**, *263*, 21-26.

(18) Spirko, V. Potential energy curve of Be-2 in its ground electronic state. *Journal of Molecular Spectroscopy* **2006**, *235*, 268-270.

(19) Kowalski, K.; Hirata, S.; Wloch, M.; Piecuch, P.; Windus, T. L. Active-space coupled-cluster study of electronic states of Be-3. *Journal of Chemical Physics* **2005**, *123*, 6.

(20) Srinivas, S.; Jellinek, J. Structural and electronic properties of small beryllium clusters: A theoretical study. *Journal of Chemical Physics* **2004**, *121*, 7243-7252.

(21) Junquera-Hernandez, J. M.; Sanchez-Marin, J.; Bendazzoli, G. L.; Evangelisti, S. Full configuration interaction calculation of singlet excited states of Be-3. *Journal of Chemical Physics* **2004**, *121*, 7103-7109.

(22) Junquera-Hernandez, J. M.; Sanchez-Marin, J.; Bendazzoli, G. L.; Evangelisti, S. Full configuration interaction calculation of Be-3. *Journal of Chemical Physics* **2004**, *120*, 8405-8411.

(23) Beyer, M. K.; Kaledin, L. A.; Kaledin, A. L.; Heaven, M. C.; Bondybey, V. E. Density functional calculations of beryllium clusters Be-n, n=2-8. *Chemical Physics* **2000**, *262*, 15-23.

(24) Kaplan, I. G.; Roszak, S.; Leszczynski, J. Nature of binding in the alkaline-earth clusters: Be-3, Mg-3, and Ca-3. *Journal of Chemical Physics* **2000**, *113*, 6245-6252.

(25) Kolchin, A. M.; Hall, R. W. Electronic properties of small neutral and charged beryllium clusters. *Journal of Chemical Physics* **2000**, *113*, 4083-4092.

(26) Begue, D.; Merawa, M.; Rerat, M.; Pouchan, C. Dynamic dipole polarizabilities and C-6 dispersion coefficients for small clusters of beryllium Be-n (n = 2,3,4). *Chemical Physics Letters* **1999**, *301*, 43-52.

(27) Gdanitz, R. J. Accurately solving the electronic Schrodinger equation of atoms and molecules using explicitly correlated (r(12)-)MR-CI. The ground state of beryllium dimer (Be-2). *Chemical Physics Letters* **1999**, *312*, 578-584.

(28) Roeggen, I.; Almlof, J. Interatomic potential for the X(1)Sigma(+)(g) state of Be-2. *International Journal of Quantum Chemistry* **1996**, *60*, 453-466.

(29) Starck, J.; Meyer, W. The ground state potential of the beryllium dimer. *Chemical Physics Letters* **1996**, *258*, 421-426.

(30) Evangelisti, S.; Bendazzoli, G. L.; Gagliardi, L. FULL CONFIGURATION-INTERACTION CALCULATIONS ON BE2. *Chemical Physics* **1994**, *185*, 47-56.

(31) Sudhakar, P. V.; Lammertsma, K. BOND PROPERTIES OF BE(3-7) CLUSTERS. *Journal of Chemical Physics* **1993**, *99*, 7929-7937.

(32) Petersson, G. A.; Shirley, W. A. THE BERYLLIUM DIMER POTENTIAL. *Chemical Physics Letters* **1989**, *160*, 494-501.

(33) Khanna, S. N.; Reuse, F.; Buttet, J. ELECTRONIC-STRUCTURE AND STABILITY OF CHARGED BERYLLIUM CLUSTERS. *Zeitschrift Fur Physik D-Atoms Molecules and Clusters* **1989**, *12*, 357-359.

(34) Khanna, S. N.; Reuse, F.; Buttet, J. STABILITY AND OBSERVABILITY OF CHARGED BERYLLIUM CLUSTERS. *Physical Review Letters* **1988**, *61*, 535-538.

(35) Merritt, J. M.; Bondybey, V. E.; Heaven, M. C. Beryllium Dimer-Caught in the Act of Bonding. *Science* **2009**, *324*, 1548-1551.

(36) Merritt, J. M.; Kaledin, A. L.; Bondybey, V. E.; Heaven, M. C. The ionization energy of Be(2), and spectroscopic characterization of the (1)(3)Sigma(+)(u), (2)(3)Pi(g), and (3)(3)Pi(g) states. *Physical Chemistry Chemical Physics* **2008**, *10*, 4006-4013.

(37) Kaledin, L. A.; Kaledin, A. L.; Heaven, M. C.; Bondybey, V. E. Electronic structure of B-2: theoretical and experimental results. *Journal of Molecular Structure-Theochem* **1999**, *461*, 177-186.

(38) Bondybey, V. E.; English, J. H. LASER VAPORIZATION OF BERYLLIUM - GAS-PHASE SPECTRUM AND MOLECULAR-POTENTIAL OF BE2. *Journal of Chemical Physics* **1984**, *80*, 568-570.

(39) Merritt, J. M.; Bondybey, V. E.; Heaven, M. C. Spectroscopy, Structure, and Ionization Energy of BeOBe. *Journal of Physical Chemistry A* **2009**, *113*, 13300-13309.

(40) Andrews, L.; Chertihin, G. V.; Thompson, C. A.; Dillon, J.; Byrne, S.; Bauschlicher, C. W. Infrared spectra and quantum chemical calculations of group 2 MO(2), O(2)MO(2), and related molecules. *Journal of Physical Chemistry* **1996**, *100*, 10088-10099.

(41) Corderman, R. R.; Lineberger, W. C. NEGATIVE-ION SPECTROSCOPY. *Annual Review of Physical Chemistry* **1979**, *30*, 347-378.

(42) Boesl, U.; Knott, W. J. Negative ions, mass selection, and photoelectrons. *Mass Spectrometry Reviews* **1998**, *17*, 275-305.

(43) Desai, S. R.; Wu, H. B.; Rohlfing, C. M.; Wang, L. S. A study of the structure and bonding of small aluminum oxide clusters by photoelectron spectroscopy: AlxOy- (x=1-2, y=1-5). *Journal of Chemical Physics* **1997**, *106*, 1309-1317.

(44) Zhai, H. J.; Wang, L. S. Probing the electronic structure and band gap evolution of titanium oxide clusters (TiO2)(n)(-) (n=1-10) using photoelectron spectroscopy. *Journal of the American Chemical Society* **2007**, *129*, 3022-3026.

(45) Jellinek, J.; Acioli, P. H.; Garcia-Rodeja, J.; Zheng, W. J.; Thomas, O. C.; Bowen, K. H. Mn-n(-) clusters: Size-induced transition to half metallicity. *Physical Review B* **2006**, *74*.

(46) Wang, X. B.; Wang, L. S. Development of a low-temperature photoelectron spectroscopy instrument using an electrospray ion source and a cryogenically controlled ion trap. *Review of Scientific Instruments* **2008**, *79*, 8.

(47) Hock, C.; Kim, J. B.; Weichman, M. L.; Yacovitch, T. I.; Neumark, D. M. Slow photoelectron velocity-map imaging spectroscopy of cold negative ions. *Journal of Chemical Physics* **2012**, *137*, 6.

(48) Itano, W. M.; Bergquist, J. C.; Bollinger, J. J.; Wineland, D. J. COOLING METHODS IN ION TRAPS. *Physica Scripta* **1995**, *T59*, 106-120.

(49) Gerlich, D.; Borodi, G. Buffer gas cooling of polyatomic ions in rf multi-electrode traps. *Faraday Discussions* **2009**, *142*, 57-72.

(50) Andersen, T.; Lykke, K. R.; Neumark, D. M.; Lineberger, W. C. AUTODETACHMENT STUDY OF THE ELECTRONIC SPECTROSCOPY OF FEO. *Journal of Chemical Physics* **1987**, *86*, 1858-1867.

(51) Garand, E.; Neumark, D. M. Study of RgS(-) and RgS (Rg = Ne, Ar, and Kr) via slow photoelectron velocity-map imaging spectroscopy and ab initio calculations. *Journal of Chemical Physics* **2011**, *135*, 8.

(52) Lykke, K. R.; Neumark, D. M.; Andersen, T.; Trapa, V. J.; Lineberger, W. C. AUTODETACHMENT SPECTROSCOPY AND DYNAMICS OF CH2CN- AND CD2CN. *Journal of Chemical Physics* **1987**, *87*, 6842-6853.

(53) Zhai, H. J.; Kiran, B.; Cui, L. F.; Li, X.; Dixon, D. A.; Wang, L. S. Electronic structure and chemical bonding in MOn- and MOn clusters (M=Mo, W; n=3-5): A photoelectron spectroscopy and ab initio study. *Journal of the American Chemical Society* **2004**, *126*, 16134-16141.

(54) Zhai, H. J.; Wang, L. S.; Alexandrova, A. N.; Boldyrev, A. I. Electronic structure and chemical bonding of B-5(-) and B-5 by photoelectron spectroscopy and ab initio calculations. *Journal of Chemical Physics* **2002**, *117*, 7917-7924.

(55) Akola, J.; Manninen, M.; Hakkinen, H.; Landman, U.; Li, X.; Wang, L. S. Photoelectron spectra of aluminum cluster anions: Temperature effects and ab initio simulations. *Physical Review B* **1999**, *60*, 11297-11300.

(56) Bragg, A. E.; Verlet, J. R. R.; Kammrath, A.; Neumark, D. M. C-6(-) electronic relaxation dynamics probed via time-resolved photoelectron imaging. *Journal of Chemical Physics* **2004**, *121*, 3515-3526.

(57) Bragg, A. E.; Kammrath, A.; Verlet, J. R. R.; Cheshnovsky, O.; Neumark, D. M. Intra- and interband relaxation dynamics of anionic mercury clusters via time-resolved photoelectron imaging and phofragmentation studies. *Abstracts of Papers of the American Chemical Society* **2004**, *227*, U330-U330.

(58) Callender, C. L.; Mitchell, S. A.; Hackett, P. A. INTERATOMIC POTENTIALS FOR VANDERWAALS COMPLEXES OF GROUP-13 METAL ATOMS - ALAR, ALKR, AND ALXE. *Journal of Chemical Physics* **1989**, *90*, 5252-5261.

(59) Heidecke, S. A.; Fu, Z. W.; Colt, J. R.; Morse, M. D. SPECTROSCOPY OF ALAR AND ALKR FROM 31000 CM-1 TO THE IONIZATION LIMIT. *Journal of Chemical Physics* **1992**, *97*, 1692-1710.

(60) Pasternack, L.; Dagdigian, P. J. EFFECT OF REAGENT TRANSLATION ON PRODUCT INTERNAL ENERGY-DISTRIBUTIONS - LASER FLUORESCENCE STUDY OF AL+O2. *Journal of Chemical Physics* **1977**, *67*, 3854-3863.

(61) Koch, W.; Collins, J. R.; Frenking, G. ARE THERE NEUTRAL HELIUM COMPOUNDS WHICH ARE STABLE IN THEIR GROUND-STATE - A THEORETICAL INVESTIGATION OF HEBCH AND HEBEO. *Chemical Physics Letters* **1986**, *132*, 330-333.

(62) Frenking, G.; Koch, W.; Gauss, J.; Cremer, D. STABILITIES AND NATURE OF THE ATTRACTIVE INTERACTIONS IN HEBEO, NEBEO, AND ARBEO AND A COMPARISON WITH ANALOGS NGLIF, NGBN, AND NGLIH (NG=HE,AR) - A THEORETICAL INVESTIGATION. *Journal of the American Chemical Society* **1988**, *110*, 8007-8016.

(63) Takayanagi, T.; Motegi, H.; Taketsugu, Y.; Taketsugu, T. Accurate ab initio electronic structure calculations of the stable helium complex: HeBeO. *Chemical Physics Letters* **2008**, *454*, 1-6.

(64) Motegi, H.; Kakizaki, A.; Takayanagi, T.; Taketsugu, Y.; Takesugu, T.; Shiga, M. Path-integral molecular dynamics simulations of BeO embedded in helium clusters: Formation of the stable HeBeO complex. *Chemical Physics* **2008**, *354*, 38-43.

(65) Merritt, J. M.; Bondybey, V. E.; Heaven, M. C. Experimental and theoretical study of the electronic spectrum of BeAl. *Physical Chemistry Chemical Physics* **2008**, *10*, 5403-5411.

(66) Heaven, M. C.; Bondybey, V. E.; Merritt, J. M.; Kaledin, A. L. The unique bonding characteristics of beryllium and the Group IIA metals. *Chemical Physics Letters* **2011**, *506*, 1-14.

(67) Couchman, S. A.; Holzmann, N.; Frenking, G.; Wilson, D. J. D.; Dutton, J. L. Beryllium chemistry the safe way: a theoretical evaluation of low oxidation state beryllium compounds. *Dalton Transactions* **2013**, *42*, 11375-11384.

(68) Diaz-Torrejon, C. C.; Kaplan, I. G. Many-body forces and stability of the alkaline-earth tetramers. *Chemical Physics* **2011**, *381*, 67-71.

(69) Iversen, K. J.; Couchman, S. A.; Wilson, D. J. D.; Dutton, J. L. Modern organometallic and coordination chemistry of beryllium. *Coordination Chemistry Reviews* **2015**, *297*, 40-48.

(70) Bondybey, V. E. Electronic structure and bonding of diatomic beryllium. *Chem. Phys. Lett. FIELD Full Journal Title:Chemical Physics Letters* **1984**, *109*, 436-441.

(71) Cerowski, V.; Rao, B. K.; Khanna, S. N.; Jena, P.; Ishii, S.; Ohno, K.; Kawazoe, Y. Evolution of the electronic structure of Be clusters. *Journal of Chemical Physics* **2005**, *123*.

(72) Marino, M. M.; Ermler, W. C. ELECTRONIC STATES AND GEOMETRIES OF SMALL BE CLUSTERS. *Journal of Chemical Physics* **1987**, *86*, 6283-6294.

(73) Pecul, M.; Jaszunski, M.; Larsen, H.; Jorgensen, P. Singlet excited states of Be-2. *Journal of Chemical Physics* **2000**, *112*, 3671-3679.

(74) Rao, B. K.; Khanna, S. N.; Meng, J.; Jena, P. GEOMETRIES AND BINDING-ENERGIES OF SMALL BERYLLIUM CLUSTERS USING VARIOUS LEVELS OF APPROXIMATIONS FOR EXCHANGE AND CORRELATION - A COMPARATIVE-STUDY. *Zeitschrift Fur Physik D-Atoms Molecules and Clusters* **1991**, *18*, 171-174.

(75) Roeggen, I.; Morokuma, K.; Yamashita, K. ON THE BINDING-ENERGY OF THE GROUND-STATE OF BE2. *Chemical Physics Letters* **1987**, *140*, 349-354.

(76) Watts, J. D.; Cernusak, I.; Noga, J.; Bartlett, R. J.; Bauschlicher, C. W.; Lee, T. J.; Rendell, A. P.; Taylor, P. R. TRIPLE AND QUADRUPLE EXCITATION CONTRIBUTIONS TO THE BINDING IN BE CLUSTERS - CALIBRATION CALCULATIONS ON BE-3. *Journal of Chemical Physics* **1990**, *93*, 8875-8880.

(77) Whiteside, R. A.; Krishnan, R.; Pople, J. A.; Kroghjespersen, M. B.; Schleyer, P. V.; Wenke, G. SMALL ELEMENTAL CLUSTERS .1. THE

STRUCTURES OF BE2, BE3, BE4, AND BE5. *Journal of Computational Chemistry* **1980**, *1*, 307-322.

(78) Gdanitz, R. J. Accurately solving the electronic Schrodinger equation using explicitly correlated (r(12)-) multi-reference methods. *Recent Research Developments in Quantum Chemistry, Vol 3* **2002**, *3*, 245-276.

(79) Gerber, I. C.; Angyan, J. G. Potential curves for alkaline-earth dimers by density functional theory with long-range correlation corrections. *Chemical Physics Letters* **2005**, *416*, 370-375.

(80) Kaplan, I. G.; HernandezCobos, J.; OrtegaBlake, I.; Novaro, O. Many-body forces and electron correlation in small metal clusters. *Physical Review A* **1996**, *53*, 2493-2500.

(81) Kaplan, I. G.; Murrell, J. N.; Roszak, S.; Leszczynski, J. Ab initio model potentials for the alkaline-earth trimers Be-3, Mg-3, and Ca-3. *Molecular Physics* **2002**, *100*, 843-849.

(82) Lee, J. S. Basis-set limit binding energies of Be-n and Mg-n (n=2,3,4) clusters. *Physical Review A* **2003**, *68*, 7.

(83) Srnec, M.; Zahradnik, R. Diatomics AB (A = Be, Mg; B=O, S) and oligomers thereof: A theoretical study. *Chemical Physics Letters* **2005**, *407*, 283-288.

(84) Veldkamp, A.; Frenking, G. STRUCTURES AND BOND-ENERGIES OF THE NOBLE-GAS COMPLEXES NGBEO (NG=AR, KR, XE). *Chemical Physics Letters* **1994**, *226*, 11-16.

(85) Shinde, R.; Tayade, M. Remarkable Hydrogen Storage on Beryllium Oxide Clusters: First-Principles Calculations. *Journal of Physical Chemistry C* **2014**, *118*, 17200-17204.

(86) Alipour, M. Theoretical Determination of the Differential Polarizability and Anisotropy of Alkaline Earth Oxide Nanoclusters (BeO)(n) n=2-9 : The Basis Set and Electron Correlation Effects. *International Journal of Quantum Chemistry* **2014**, *114*, 255-260.

(87) Qu, Y. H.; Zhang, Y. Z. Structure and vibrations of BenOn (n=3-10) clusters. *Spectrochimica Acta Part a-Molecular and Biomolecular Spectroscopy* **2007**, *67*, 350-354.

(88) Bondybey, V. E. ELECTRONIC-STRUCTURE AND BONDING OF BE2. *Chemical Physics Letters* **1984**, *109*, 436-441.

(89) Begue, D.; Merawa, M.; Rerat, M.; Pouchan, C. Long-range coefficients for the low-lying electronic states of BeLi and Be-2. *Journal of Chemical Physics* **1999**, *110*, 2051-2058.

(90) Bondybey, V. E. LASER-INDUCED FLUORESCENCE AND BONDING OF METAL DIMERS. *Science* **1985**, *227*, 125-131.

(91) Cernusak, I.; Noga, J.; Diercksen, G. H. F.; Sadlej, A. J. A STUDY OF THE RELIABILITY OF DIFFERENT MANY-BODY METHODS - POTENTIAL-ENERGY CURVE FOR THE GROUND-STATE OF BE-2. *Chemical Physics* **1988**, *125*, 255-260.

(92) Galek, P. T. A.; Handy, N. C.; Lester, W. A., Jr. Quantum Monte Carlo studies on small molecules. *Molecular Physics* **2006**, *104*, 3069-3085.

(93) Ruzsinszky, A.; Perdew, J. P.; Csonka, G. I. Binding energy curves from nonempirical density functionals II. van der Waals bonds in rare-gas and alkaline-earth diatomics. *Journal of Physical Chemistry A* **2005**, *109*, 11015-11021.

(94) Porsev, S. G.; Derevianko, A. High-accuracy calculations of dipole, quadrupole, and octupole electric dynamic polarizabilities and van der Waals coefficients C-6, C-8, and C-10 for alkaline-earth dimers. *Journal of Experimental and Theoretical Physics* **2006**, *102*, 195-205.

(95) Patkowski, K.; Podeszwa, R.; Szalewicz, K. Interactions in diatomic dimers involving closed-shell metals. *Journal of Physical Chemistry A* **2007**, *111*, 12822-12838.

(96) Palke, W. E.; Kirtman, B. CALCULATIONS OF THE BENDING POTENTIALS OF MGOH AND BEOH. *Chemical Physics Letters* **1985**, *117*, 424-426.

(97) Bauschlicher, C. W.; Langhoff, S. R.; Partridge, H. ABINITIO STUDY OF THE ALKALI AND ALKALINE-EARTH MONOHYDROXIDES. *Journal of Chemical Physics* **1986**, *84*, 901-909.

(98) Theodorakopoulos, G.; Petsalakis, I. D.; Hamilton, I. P. Ab initio calculations on the ground and excited states of BeOH and MgOH. *Journal of Chemical Physics* **1999**, *111*, 10484-10490.

(99) Fletcher, D. A.; Anderson, M. A.; Barclay, W. L.; Ziurys, L. M. MILLIMETER-WAVE SPECTROSCOPY OF VIBRATIONALLY EXCITED GROUND-STATE ALKALINE-EARTH HYDROXIDE RADICALS (X(2)SIGMA(+)). *Journal of Chemical Physics* **1995**, *102*, 4334-4339.

(100) Brom, J. M.; Weltner, W. ESR-SPECTRUM AND STRUCTURE OF MGOH RADICAL. *Journal of Chemical Physics* **1973**, *58*, 5322-5330.

(101) Bunker, P. R.; Kolbuszewski, M.; Jensen, P.; Brumm, M.; Anderson, M. A.; Barclay, W. L.; Ziurys, L. M.; Ni, Y.; Harris, D. O. NEW ROVIBRATIONAL DATA FOR MGOH AND MGOD AND THE INTERNUCLEAR POTENTIAL FUNCTION OF THE GROUND ELECTRONIC-STATE. *Chemical Physics Letters* **1995**, *239*, 217-222.

(102) Tandy, J. D.; Wang, J. G.; Bernath, P. F. High-resolution laser spectroscopy of BaOH and BaOD: Anomalous spin-orbit coupling in the (A)(2)over tilde(2)Pi state. *Journal of Molecular Spectroscopy* **2009**, *255*, 63-67.

(103) Wang, J. G.; Dick, M. J.; Sheridan, P. M.; Yu, S.; Bernath, P. F. Further spectroscopic investigations of the high energy electronic states of SrOH: The (B)over-tilde '(2)Sigma(+)(000)-(A)over-tilde(2)Pi(000) and the (D)over-tilde(2)Sigma(+)(000)-(A)over-tilde(2)Pi(000) transitions. *Journal of Molecular Spectroscopy* **2007**, *245*, 26-33.

(104) Beardah, M. S.; Ellis, A. M. Observation of a new (2)Sigma(+)-(2)Sigma(+) transition of the SrOH free radical. *Journal of Molecular Spectroscopy* **2003**, *218*, 80-84.

(105) Presunka, P. I.; Coxon, J. A. LASER EXCITATION AND DISPERSED FLUORESCENCE INVESTIGATIONS OF THE A(2)PI-X(2)SIGMA(+) SYSTEM OF SROH. *Chemical Physics* **1995**, *190*, 97-111.

(106) Coxon, J. A.; Li, M. G.; Presunka, P. I. LASER FLUORESCENCE EXCITATION SPECTROSCOPY OF CAOH AND CAOD - THE A2-PI-X2-SIGMA+ (100)-(000) BAND SYSTEM AND THE (100)-(020) FERMI RESONANCE. *Journal of Molecular Spectroscopy* **1991**, *150*, 33-45.

(107) Fernando, W.; Douay, M.; Bernath, P. F. VIBRATIONAL ANALYSIS OF THE A2-PI-X2-SIGMA+ AND A'2-DELTA-X2-SIGMA+ TRANSITIONS OF BAOH AND BAOD. *Journal of Molecular Spectroscopy* **1990**, *144*, 344-351.

(108) Koput, J.; Peterson, K. A. Ab initio prediction of the potential energy surface and vibrational-rotational energy levels of X(2)A ' BeOH. *Journal of Physical Chemistry A* **2003**, *107*, 3981-3986.

(109) Hakkinen, H.; Yoon, B.; Landman, U.; Li, X.; Zhai, H. J.; Wang, L. S. On the electronic and atomic structures of small Au-N(-) (N=4-14) clusters: A photoelectron spectroscopy and density-functional study. *Journal of Physical Chemistry A* **2003**, *107*, 6168-6175.

(110) Wiley, W. C.; McLaren, I. H. TIME-OF-FLIGHT MASS SPECTROMETER WITH IMPROVED RESOLUTION. *Review of Scientific Instruments* **1955**, *26*, 1150-1157.

(111) Duncan, M. A. Invited Review Article: Laser vaporization cluster sources. *Review of Scientific Instruments* **2012**, *83*, 19.

(112) Dahl, D. A. SIMION for the personal computer in reflection. *International Journal of Mass Spectrometry* **2000**, *200*, 3-25.

(113) Li, W.; Chambreau, S. D.; Lahankar, S. A.; Suits, A. G. Megapixel ion imaging with standard video. *Review of Scientific Instruments* **2005**, *76*, 7.

(114) Roberts, G. M.; Nixon, J. L.; Lecointre, J.; Wrede, E.; Verlet, J. R. R. Toward real-time charged-particle image reconstruction using polar onion-peeling. *Review of Scientific Instruments* **2009**, *80*, 7.

(115) Dick, B. Inverting ion images without Abel inversion: maximum entropy reconstruction of velocity maps. *Physical Chemistry Chemical Physics* **2014**, *16*, 570-580.

(116) Garcia, G. A.; Nahon, L.; Powis, I. Two-dimensional charged particle image inversion using a polar basis function expansion. *Review of Scientific Instruments* **2004**, *75*, 4989-4996.

(117) Dribinski, V.; Ossadtchi, A.; Mandelshtam, V. A.; Reisler, H. Reconstruction of abel-transformable images: The Gaussian basis-set expansion abel transform method. *Review of Scientific Instruments* **2002**, *73*, 2634-2642.

(118) Mascaritolo, K. J.; Antonov, I. O.; Heaven, M. C. Two-photon excitation of the (2)Pi(4p)-X-2 Pi(3p) transition of AlAr. *Journal of Molecular Spectroscopy* **2014**, *297*, 1-3.

(119) Mascaritolo, K. J.; Merritt, J. M.; Heaven, M. C.; Jensen, P. Experimental and Theoretical Characterization of the 2(2)A '-1(2)A ' Transition of BeOH/D. *Journal of Physical Chemistry A* **2013**, *117*, 13654-13663.

(120) Mascaritolo, K. J.; Gardner, A. M.; Heaven, M. C. Autodetachment spectroscopy of the aluminum oxide anion dipole bound state. *Journal of Chemical Physics* **2015**, *143*, 7.

(121) Mascaritolo, K. J.; Gardner, A. M.; Heaven, M. C. Autodetachment spectroscopy of the aluminum oxide anion dipole bound state (vol 143, 114311, 2015). *Journal of Chemical Physics* **2015**, *143*.

Chapter 2

Two-photon excitation of the $^2\Pi(4p)$-$X^2\Pi(3p)$ transition of AlAr.

The $^2\Pi(4p)$-$X^2\Pi(3p)$ band system of AlAr has been observed using two-photon excitation. The spectrum consists of a short progression of doublet bands, with spin-orbit intervals that are close to that of Al($4p$). Potential energy curve fitting yielded a bond dissociation energy for $^2\Pi(4p)$ of D_e=495(5) cm^{-1} and an approximate bond length of R_e=3.33(4) Å.

2.1 Introduction

The Al-Rg complexes (Rg=Ar, Kr, Xe) have been examined previously using electronic spectroscopy techniques[1-4]. These open-shell species are of interest as they can be used to explore the evolution of physical bonding forces as a function of electronic excitation. It has been shown that binding of the lower energy states benefits from the greater polarizability of the excited orbital[3]. At higher energies, where the states become increasingly more Rydberg in character, the Al-Rg binding energy increases towards the value expected for the ionic Al^+-Rg complex. To date, spectroscopic studies of Al-Rg complexes have focused on states that can be accessed by one-photon

transitions. In the present study we report a band system of Al-Ar, accessed by a two-photon excitation process.

Spectra for the $B^2\Sigma^+(4s)$-$X^2\,\Pi\,(3p)$ transition of Al-Ar were first reported by Gardner and Lester[2], who used resonant two-photon ionization (R2PI) as the means for detection of single-photon resonances. This transition was subsequently examined using laser induced fluorescence (LIF) spectroscopy. Callender, Mitchell and Hackett[1] characterized the dispersed fluorescence spectrum, from which they derived a ground state dissociation energy of D_0=136±65 cm^{-1}. McQuaid, Gole and Heaven[4] recorded rotationally resolved spectra, from which the $B^2\Sigma^+(4s)$ state potential energy curve was recovered via the RKR inversion process. Heidecke et al.[3] used R2PI to study a wide range of states, spanning the range from $B^2\Sigma^+(4s)$ all the way to the ionization limit. Term energies and vibrational constants were reported for 33 electronically excited states. The ionization energy was found to be 47418.5(±2.0) cm^{-1}. In the energy range of relevance to the present study, 32400-33000 cm^{-1}, they observed states that were attributed to the Al(3*d*)+Ar and Al(4*p*)+Ar dissociation asymptotes. The two-photon excitation spectra reported here provide new information concerning the $^2\Pi(4p)$ state.

2.2 Experimental

The apparatus used for these measurements has been described previously[5]. Al-Ar complexes were generated using a conventional pulsed laser ablation source[6]. The fundamental from a Nd/YAG laser (1064nm, ≈5 mJ/ pulse) was used to ablate the surface of an Al rod. The ablation plume was entrained in pure Ar at a pressure of 7.6 atm, and

cooled by supersonic free-jet expansion. Al-Ar complexes formed during this expansion process. The core of the expansion was sampled via a conical skimmer, into the ion source region of a time-of-flight mass spectrometer. The Al-Ar complexes were photo-ionized by the beam from a tunable dye laser, operating over the wavelength range 606.06 - 617.28 nm. Three photons are required for ionization at this wavelength. As there are no one-photon resonances in this range, resonantly enhanced ionization could be unambiguously assigned to a 2+1 sequence. Spectra were recorded by monitoring the ion current associated with the arrival time for $AlAr^+$ (m/*e*=67). The dye laser was operated with a beam diameter of 2 mm and a pulse energy of approximately 5 mJ. The linewidth (FWHM) was 0.3 cm^{-1}. Absolute wavelength calibration was obtained using a commercial wavemeter (Bristol Instruments model 821).

2.3 Results and Discussion

Figure 1 shows the 2+1 photoionization spectrum. The bands in the low energy range (two-photon energies of 32300 - 32580 cm^{-1}) were weak and the vertical scale has been expanded to show them more clearly. The intensities in this trace have not been adjusted for variation of the laser power over the scan. These features were readily identified as the bands of the $^2\Delta(3d)$, $^2\Pi(3d)$, $^2\Sigma(3d) \leftarrow X^2\Pi(3p)$ series reported by Heidecke et al.[3] The more intense features in the 32580 - 32850 cm^{-1} range present a simple vibrational progression of doublets that do not correspond to any of the systems reported by Heidecke et al.[3] These bands were not rotationally resolved, and so we present the band centers in Table 1, along with the doublet spacings.

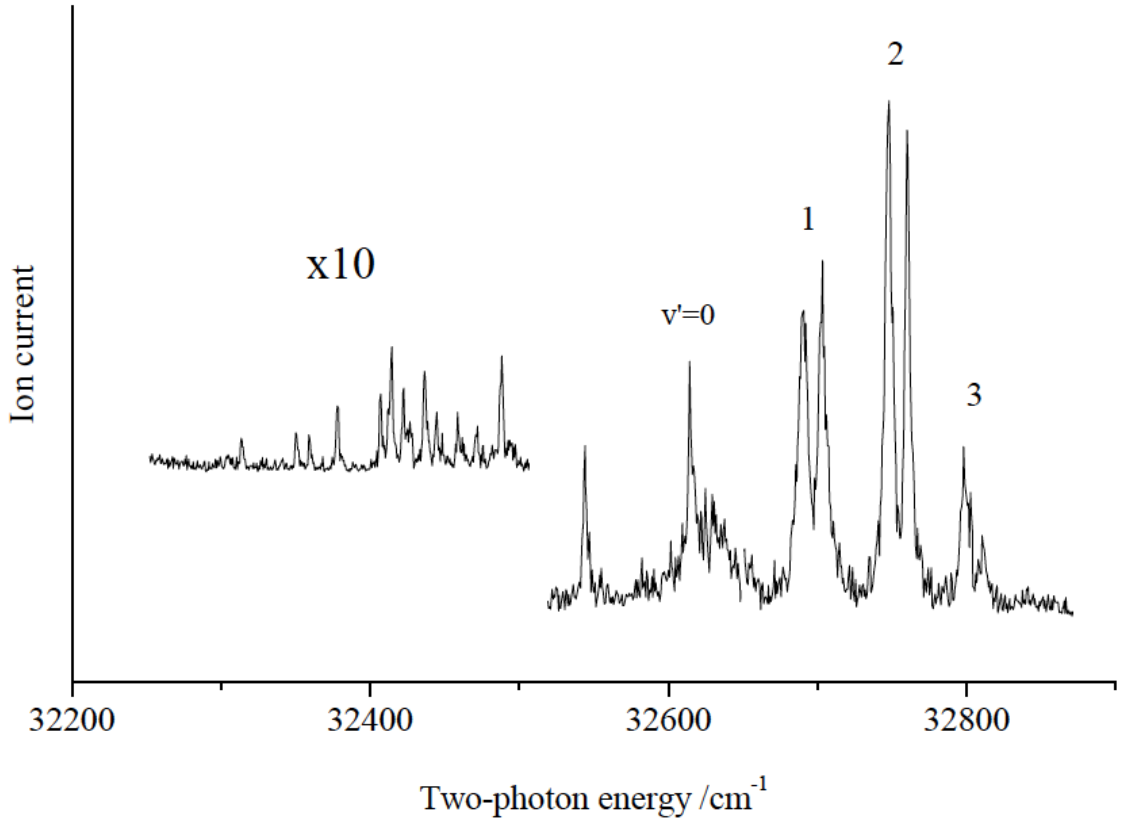

Figure 1. Two-photon excitation spectrum of AlAr. The peaks with vibrational numbers are assigned to the $^2\Pi(4p)$-$X^2\Pi_{1/2}(3p)$ transition. Note that the vertical axis was expanded by a factor of 10 to display the weak features in the 32300-32580 cm^{-1} range.

Table 1. Band centers for the $^2\Pi(4p)$-$X^2\Pi_{1/2}(3p)$ transition of AlAr

v'	$^2\Pi_{1/2}$	$^2\Pi_{3/2}$	ΔE
0	32618.5	32637.0	18.5
1	32690.3	32703.4	13.1
2	32747.7	32760.4	12.7
3	32799.0	32810.9	11.9

The band centers are given in cm^{-1} units, with uncertainties of ± 0.2 cm^{-1}. The fourth column gives the interval between the spin-orbit components.

To assign the new transition, we begin by considering the lowest energy band observed at 32618.5 cm^{-1}. Heidecke et al.[3] determined that the ground state dissociation energy was 122.4(40) cm^{-1}. Hence, the lowest energy band lies 32496.1 cm^{-1} above the Al(3*p*, $^2P_{1/2}$)+Ar dissociation asymptote. This precludes assignment to a state that correlates with Al(3*d*) as the highest energy component ($^2D_{3/2}$) is at 32436.8 cm^{-1} relative to (3*p*, $^2P_{1/2}$)[7]. The obvious conclusion is that the new band system correlates with the Al(4*p*, ^2P)+Ar dissociation asymptote, which is consistent with the selection rules for two-photon excitation in the atomic limit. Furthermore, the doublet splittings (Table 1) are approximately consistent with the Al(4*p*, ^2P) spin-orbit interaction constant of A_{SO}=10.55 cm^{-1} (derived from the 4*p* $^2P_{3/2}$-$^2P_{1/2}$ interval[7]). Without interactions between the states of different electronic configuration, it is expected that the ^2P(4*p*) state would exhibit a spin orbit splitting that was close to A_{SO}. It is likely that the larger observed value for the lowest energy states reflects interactions between the Al(3*d*, $^2D_{3/2}$)-Ar and Al(4*p*, $^2P_{3/2}$)-Ar configurations.

The intensity envelope of the new band system indicates that there is a significant change in the equilibrium bond length on electronic excitation, and that the bands originate from the ground state zero-point level. Based on the behavior of the numerous excited states characterized by Heidecke et al.[3], it is almost certain that the excited state has a smaller equilibrium bond length. For this situation the remaining problem is to determine the vibrational numbering. A search for a doublet band of the transition at energies below 32618.5 cm^{-1} did not produce any promising candidates, suggesting that the first observed level is v'=0. The vibrational assignment was further explored by calculating excited state vibrational intervals and Franck Condon factors. For this

purpose, the ground state potential energy curve was represented by a Lennard-Jones potential of the form,

$$V_X(R) = D_e\left(\left(\frac{R_e}{R}\right)^{12} - 2\left(\frac{R_e}{R}\right)^{6}\right) \qquad (1)$$

with R_e=3.79 Å and D_e=141.0 cm^{-1} chosen to reproduce the existing experimental data. For development of the excited state potential energy curve, the spin orbit interaction was removed from the experimental data by considering the mean energies for each doublet. The relative intensities were taken as the mean values for the doublets. To provide flexibility, the Extended Morse Oscillator function was used to represent the excited state potential energy curve. This is defined by the expression[8]

$$V_\Pi(R) = D_e\left(1 - \exp\left(-\phi(R)(R - R_e)\right)\right)^2 \qquad (2)$$

with $\phi(R) = \phi_0 + \phi_1 y(R)$ and $y(R) = \left(R^4 - R_e^4\right)/\left(R^4 + R_e^4\right)$. The computer code Level 8.0[8] was used to compute the vibrational energies and Franck-Condon factors for potentials 1 and 2. Trial-and-error fitting to the relative intensities and vibrational intervals yielded excited state potential parameters of D_e=495(5) cm^{-1}, R_e=3.33(4) Å, ϕ_0=1.78(3) $Å^{-1}$ and ϕ_1=-1.15(4) $Å^{-1}$. These parameters lead to a bond dissociation energy of D_0=456 cm^{-1}. The calculated vibrational intervals and Franck-Condon factors are compared with the experimental data in Table 2. We note that the well-depth estimated for $^2\Pi$(4*p*) is quite similar to that of the most deeply bound Al(3*d*)-Ar state, D_0(3*d*, $^2\Delta$)=525 cm^{-1} (ref. [3]), while the equilibrium distance is somewhat larger than that of

Table 2. Observed and calculated properties for the $^2\Pi(4p)$-$X^2\Pi_{1/2}(3p)$ transition of AlAr

v'	$\Delta G_{v'+1/2}$ (obs)[a]	$\Delta G_{v'+1/2}$ (calc)	Relative Intensity[b]	FCF
0	69.1	69.5	0.09	0.06
1	57.2	58.4	0.29	0.31
2	50.9	48.9	0.44	0.44
3	-	40.7	0.09	0.17

[a.] In units of cm^{-1}, these intervals are derived from the mid-points of the spin-orbit doublets.

[b.] These are the mean relative intensities for the spin-orbit doublets. They have been scaled to produce agreement with the calculated Franck-Condon factor (FCF) for the 2-0 band. It is likely that the experimental intensity for the 3-0 band is underestimated due to the lower power from the dye laser at this wavelength.

the $B^2\Sigma^+$ state (R_e=3.05(1) Å)[4]. The agreement between the observed and predicted band intensities supports assignment of the lowest energy band as the v'=0-v''=0 origin.

Heidecke et al.[3] observed a progression starting at 32328.16(32) that was very tentatively considered as a candidate for the $^2\Pi(4p)$-$X^2\Pi$ transition. We did not observe those bands in our two-photon excitation scan. Professor Morse has suggested that these extra features may belong to a larger cluster (e.g., $AlAr_2$) that fragmented to produce signals in the $AlAr^+$ detection channel.

2.4 Postscript

In the process of soliciting comments on this note we learned that the band systems we observed had been recorded previously by Professor Okumura and his co-workers. Their results were presented at an ACS meeting (M. Okumura, J. M. Spotts, Chi-Kin Wong, J. A. Boatz, J. A. Sheehy, P. W. Langhoff, and R. J. Hinde, *"Electronic state mixing in AlAr clusters,"* Book of Abstracts, 218th ACS National Meeting, New Orleans, Aug. 22-26 (1999), PHYS-194).

2.5 Acknowledgement

We thank Professor's Michael Morse and Mitchio Okumura for their very helpful comments on the first draft of this note. We gratefully acknowledge the support of this work by the National Science Foundation under the grant CHE-0956442.

2.6 References to Chapter 2

[1] C.L. Callender, S.A. Mitchell, P.A. Hackett, J. Chem. Phys. 90 (1989) 5252-61.

[2] J.M. Gardner, M.I. Lester, Chem. Phys. Chem. 137 (1987) 301-5.

[3] S.A. Heidecke, Z. Fu, J.R. Colt, M.D. Morse, J. Chem. Phys. 97 (1992) 1692-710.

[4] M.J. McQuaid, J.L. Gole, M.C. Heaven, J. Chem. Phys. 92 (1990) 2733-9.

[5] J.M. Merritt, A.L. Kaledin, V.E. Bondybey, M.C. Heaven, Phys. Chem. Chem. Phys. 10 (2008) 4006-13.

[6] M.A. Duncan, Rev. Sci. Instrum. 83 (2012) 041101/1-01/19.

[7] Kramida, A., Ralchenko, Yu., Reader, J., and NIST ASD Team (2013). NIST Atomic Spectra Database (ver. 5.1), [Online]. Available: http://physics.nist.gov/asd [2013, November 3]. National Institute of Standards and Technology, Gaithersburg, MD.

[8] R.J. LeRoy, LEVEL 8.0: *A Computer Program for Solving the Radial Schrödinger Equation for Bound and Quasibound Levels*, University of Waterloo Chemical Physics Research Report CP-663 (2007); see http://leroy.uwaterloo.ca/programs/.

Chapter 3

Experimental and Theoretical Characterization of the $2^2A'$-$1^2A'$ Transition of BeOH/D

The hydroxides of Ca, Sr and Ba are known to be linear molecules, while MgOH is quasilinear. High-level *ab initio* calculations for BeOH predict a bent equilibrium structure with a bond angle of 140.9°, indicating a significant contribution of covalency to the bonding. However, experimental confirmation of the bent structure is lacking. In the present study we have used laser excitation techniques to observe the $2^2A'$-$1^2A'$ transition of BeOH/D in the energy range 30300-32800 cm^{-1}. Rotationally resolved spectra were obtained, with sufficient resolution to reveal spin splittings for the electronically excited state. Two-color photoionization was used to determine an ionization energy of 66425(10) cm^{-1}. Ab initio calculations were used to guide the analysis of the spectroscopic data. Multi-reference configuration interaction calculations were used to construct potential energy surfaces for the $1^2A'$, $2^2A'$ and $1^2A''$ states. The ro-vibronic eigenstates supported by these surfaces were determined using the Morse oscillator rigid bender internal dynamics Hamiltonian. The theoretical results were in sufficiently good agreement with the experimental data to permit unambiguous assignment. It was confirmed that the equilibrium geometry of the ground state is bent,

and that the barrier to linearity lies below the zero-point energies for both BeOH and BeOD.

3.1 Introduction

The monohydroxides of the alkaline earth metals (MOH, M=Be, Mg, Ca, Sr, Ba) have been the subject of numerous theoretical[1-11] and experimental studies[12-26]. One of the motivations for this work has been the question of how the M-O bonding changes as a function of the atomic number of the metal. Theoretical studies[1,11] indicate that the heavier members of the group, M=Ca, Sr and Ba, have ionic bonds that are formally M^+-OH^-. This results in a linear equilibrium geometry, as observed for the alkali metal hydroxides[1]. The M^+-OH^- partial charge separation becomes more difficult to accomplish for the lighter alkaline earth metals Be and Mg due to their higher ionization energies (in eV units, 9.323 (Be) 7.646 (Mg), 6.113 (Ca), 5.965 (Sr) and 5.212 (Ba))[27]. Electronic structure calculations indicate that the bonding in BeOH and MgOH has significant contributions from covalent interactions that favor bent geometries[1,3,4,6]. In the case of MgOH, the interplay between ionic and covalent forces results in a potential energy surface that has a linear equilibrium structure, but is almost flat with respect to angular displacement near the minimum[18].

High-level electronic structure calculations have consistently predicted bent equilibrium structures for BeOH, with low barriers to linearity[1,6,8]. For example, the RCCSD(T) calculations of Koput and Peterson[6], performed using a basis set of 5-zeta quality, yielded an equilibrium bond angle of 140.9 degrees, with a barrier to linearity of

136 cm^{-1}. Unfortunately, the existing experimental data could not be used to determine the geometry. The earliest spectroscopic observations of BeOH were obtained for samples isolated in cryogenic rare gas matrices. Brom and Weltner[16] recorded the ESR spectrum, and concluded that the molecule was most probably linear. Thompson and Andrews[28] trapped the products resulting from the laser ablation of Be in the presence of H_2O. An IR absorption band at 1245.5 cm^{-1} was tentatively assigned to BeOH, but this did not provide any insight concerning the bond angle. Gas-phase emission spectra (300-332 nm) for BeOH and BeOD were reported by Antic-Jovanovic et al.[12] Chemical evidence was used to identify the carrier of the band systems, but there was no attempt to assign the highly congested structure. More recently, electronic spectra for jet-cooled BeOH were obtained by Heaven et al.[29] Partially resolved rotational structure was observed, yielding a first estimate for the ground state rotational constant. The result was in agreement with the predictions of the highest level theoretical calculations, but the bands that might be used to probe the question of the bond angle were not identified.

The group IIa MOH species all exhibit allowed electronic transitions that can be approximately described as metal-centered np←ns electron promotions. The lowest energy state arising from this excited configuration is of $^2\Pi$ symmetry for the linear geometry. The orbital degeneracy of this state is broken when the molecule is bent, resulting in states of $^2A'$ and $^2A''$ symmetry. For Ca, Sr and Ba, the states separate on bending, but both retain the linear equilibrium structure[19,26,30-32]. Spectra for MgOH[17] show that the $2^2A'$ state has a bent equilibrium structure ($\theta_e \approx 119$ degrees) and a barrier to linearity of 1970 cm^{-1}. Theoretical calculations[8] also predict a bent structure for the $1^2A''$ state. As would be expected from these trends, calculations for BeOH predict that both

the $2^2A'$ and $1^2A''$ states will have bent equilibrium geometries. The calculations of Theodorakopoulos et al.[8] yielded an approximate barrier to linearity for the $2^2A'$ state of 3710 cm^{-1}.

In the present study we have examined the $2^2A'$-$1^2A'$ transitions of BeOH and BeOD using laser excitation techniques. Jet-cooling was used to minimize the spectral congestion. Laser induced fluorescence (LIF) measurements provided the best resolution, while resonantly enhanced multi-photon ionization (REMPI) with mass-resolved ion detection was used to confirm the attribution of bands to BeOH or BeOD. A two-color ionization technique was used to determine the ionization energy (IE) of BeOH.

Theoretical calculations were carried out to guide the interpretation of the spectra. New potential energy surfaces for the $1^2A'$, $2^2A'$ and $1^2A''$ states were constructed using a multi-reference configuration interaction method. The ro-vibronic eigenstates of the surfaces were calculated and detailed comparisons with the spectroscopic data are reported.

3.2 Experimental

The apparatus used for these experiments has been described in detail previously[33,34]. Gas phase samples of BeOH/D were generated by pulsed laser ablation. The output of a pulsed Nd/YAG laser (Continuum Minilite II, operating at ~20 mJ per pulse at 1064 nm) was focused onto the surface of a beryllium rod, which was continuously rotated and translated to expose a fresh surface to each laser shot. The hot

plasma produced by the laser vaporization was entrained in a pulse of high pressure helium carrier gas, which was then expanded as a free jet. To promote the formation of BeOH, HNO_3 vapor was added to the He by passing the carrier gas over the surface of nitric acid. Deuterated nitric acid was used for synthesis of BeOD. The gas pulse was produced by a Jordan valve (0.5 mm orifice diameter) that was operated at source pressures over the range of 20-65 psia, with a pulse duration of 60 μs.

LIF, REMPI and photoionization efficiency (PIE) spectra were recorded to investigate the electronic structure and bonding of BeOH/D. LIF spectra were recorded with the excitation laser beam positioned 7.5 cm downstream from the nozzle orifice. For the recording of REMPI spectra and photoionization efficiency curves, the core of the expansion was sampled by a 5 mm diameter skimmer into a differentially pumped chamber that housed a time-of-flight mass spectrometer. A two-color excitation scheme was used to record REMPI spectra with mass-resolved ion detection. The ionizing photon was provided by a KrF laser operating at 248 nm (Lambda Physik Compex 102). The counter-propagating laser beams were overlapped in time and space in the ionization region of the time-of-flight mass spectrometer, along an axis perpendicular to both the molecular beam and the flight tube of the mass spectrometer.

PIE curves were recorded using two tunable dye lasers in order to locate the ionization energy. The first dye laser was set to excite a particular resonant transition of BeOH while the second dye laser was scanned to locate the onset of ionization, registered by the mass-resolved detection of $BeOH^+$ ions.

The tunable lasers used for these measurements consisted of a Nd/YAG pumped system (frequency doubled Continuum 7010 Nd/YAG with a Quanta Ray PDL1e dye

laser) and an excimer pumped dye laser (Lambda Physik Lextra pumping a FL3001 dye laser). Both dye lasers, operated without intracavity etalons, yielded fundamental linewidths close to 0.3 cm^{-1} (FWHM). For a few measurements, an etalon was used to reduce the linewidth of the Lambda Physik laser to approximately 0.06 cm^{-1}. Frequency doubling of the outputs from both dye lasers was used to generate tunable light in the near UV spectral range. Several laser dyes were used to record the spectra, and the intensities were not corrected for variations in the laser powers. Absolute wavelength calibration of the dye laser fundamentals was provided by a Bristol Instruments wavemeter (model 821) and the simultaneous recording of the I_2 B-X LIF spectrum[35].

3.3 Theoretical Calculations

Potential energy surfaces for the three lowest energy electronic states of BeOH were generated using ab initio electronic structure methods. The MOLPRO 2010.1 suite of programs[36] was used for these calculations. Roos atomic natural orbital basis sets[37] were used for Be, O and H ((14s, 9p, 4d, 3f) contracted to [5s, 4p, 3d, 2f] for Be and O, (8s, 4p, 3d)/[4s, 3p, 2d] for H). State averaged complete active space self- consistent field (sa-CASSCF) calculations were carried out for 13 electrons distributed among 11 valence orbitals. The Cartesian axes were chosen with the molecule in the y-z plane, such that z corresponds to the inertial a-axis. To ensure a smooth transition from linear to bent geometries, the calculations did not employ symmetry (C_1 point group). We found that calculations performed using C_s symmetry yielded a larger artificial splitting between the A' and A" components of the $\tilde{A}^2\Pi$ state for the linear geometry. Trial calculations were performed with the first four orbitals (O1s, Be1s, O2s and $O2p_z$+H1s) constrained to be

doubly occupied, leaving an active space of 5 electrons in 7 orbitals (5e/7o; 490 configuration state functions, with active orbital leading contributions of $O2p_y$, $O2p_x$, $Be2s\text{-}O2p_z+H1s$, $Be2p_y+H1s\text{-}O2p_y$, $Be2p_x\text{-}O2p_x$, $Be2p_z+H1s$, $Be2p_z\text{-}H1s+O2p_z$). The sa-CASSCF results were subsequently used as the starting point for multi-reference configuration interaction[38,39] calculations that included the Davidson correction[40] (MRCI+Q). In the following we denote this treatment as sa-CASSCF-MRCI+Q. As the 5e/7o active space proved to be computationally demanding for the generation of a sufficiently fine grid of single point energies, we examined the consequence of reducing the active space to 3 electrons in 6 orbitals (70 configuration state functions). Within the range of coordinate space that was relevant to the present study, the effect of reducing the active space was marginal. Consequently, the potential energy surfaces were generated using the 3e/6o active space, with all electrons correlated in the MRCI step. The highest energy molecular orbital held closed in this scheme (orbital 5) was predominantly composed of the in-plane $O2p_y$, with small contributions from Be2s, O2s and H1s. As a point of comparison, previous sa-CASSCF-MRCI calculations yielded excitation energies for the first excited state of 3.92 (adiabatic for the linear geometry[8]) and 3.96 eV (vertical[10]), while the present calculations yielded 3.89 eV (adiabatic).

The singly occupied molecular orbital (SOMO) for the ground state is mostly Be 2s, while the $2^2A'$ and $1^2A''$ states are the Renner-Teller split components of a $^2\Pi$ state for the linear geometry. The SOMO's for the latter are predominantly $Be2p_y+H1s\text{-}O2p_y$ $Be2p_x\text{-}O2p_x$. To facilitate modeling for the excited state ro-vibronic structure, the spin-orbit coupling constant was calculated for the $^2\Pi$ state with $R_{H\text{-}O}$=0.95 and $R_{O\text{-}Be}$=1.40 Å by diagonalization of the matrix for the Breit-Pauli Hamiltonian[41]. The spin-orbit matrix

elements were evaluated using the CASSCF wavefunctions for the $\tilde{X}^2\Sigma^+$, $\tilde{A}^2\Pi(A')$ and $\tilde{A}^2\Pi(A'')$ states (6x6 matrix). This yielded a value for A_{SO} of 13.4 cm^{-1}. Note that the value is greater than that of $Be^+(2p)$ (A_{SO}=4.38 cm^{-1})[42] due to mixing with the O2pπ orbitals.

Equilibrium structures for the ground state $1^2A'$ and the first two excited states, $2^2A'$ and $1^2A''$, are listed in Table 1. Two-dimensional cuts through the potential energy surfaces were produced with the H-O distance held at 0.95 Å. Single point energies were calculated on a grid with the bond angle (θ) varied from 80 to 180 degrees, in 10 degree steps. The O-Be bond length was varied from 1.20 to 1.78 Å in 0.02 Å steps. This combination yielded a grid of 330 coordinate points. Calculations were also carried out for variation of R_{H-O} (0.86 to 1.05 Å in 0.01 Å steps) and θ (125 to 150 degrees in 5 degree steps) with R_{Be-O} held at 1.40 Å. Variation of the R_{H-O} distance, over the range sampled by the zero-point motion, resulted in minor changes in the dependencies of the surfaces on R_{O-Be} and θ.

Two-dimensional cuts through the potential energy surfaces for R_{H-O}=0.95 Å are shown in Figures 1 and 2. The ground state surface (Fig. 1) corresponds to a bent equilibrium structure with a barrier to linearity of 262 cm^{-1}. In comparison to the ground state, the $2^2A'$ state has a much higher barrier to linearity and a more strongly bent equilibrium structure.

The ro-vibronic eigenstates of the three potential energy surfaces were calculated using the programs MORBID[43,44] ($1^2A'$) and RENNER[45-47] ($2^2A'$ and $1^2A''$). The analytical potential energy expressions used by these programs are defined in references [18] and [47]. Non-linear least squares fits to the single point energies were used to determine

Table 1. Calculated stationary points for the potential energy surfaces of BeOH

	$1^2A'$	$2^2A'$	$1^2A''$
R_{O-H}(Å)	0.944	0.948	0.943
R_{Be-O}(Å)	1.401	1.446	1.434
Θ (degrees)	139.0	118.2	133.4
Barrier (cm^{-1}) [a]	262	2322	129

[a.] Energy below the minimum energy linear structure

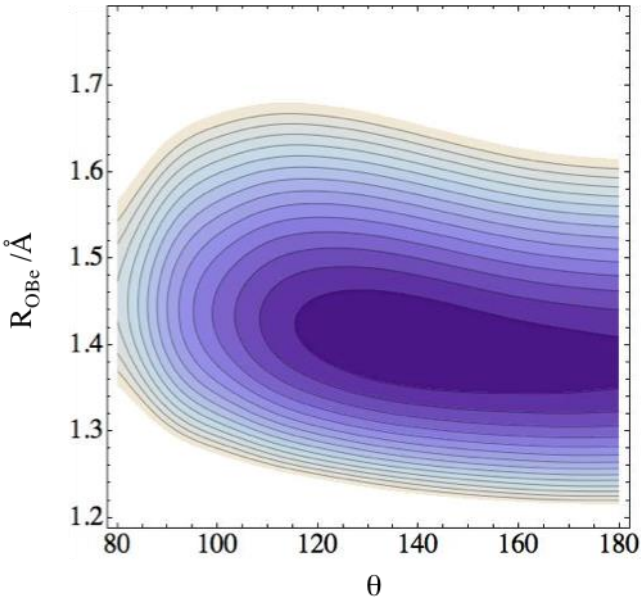

Figure 1. Potential energy contour plot for the $1^2A'$ state of BeOH (R_{HO}=0.95 Å). The contour lines are drawn at 400 cm^{-1} intervals.

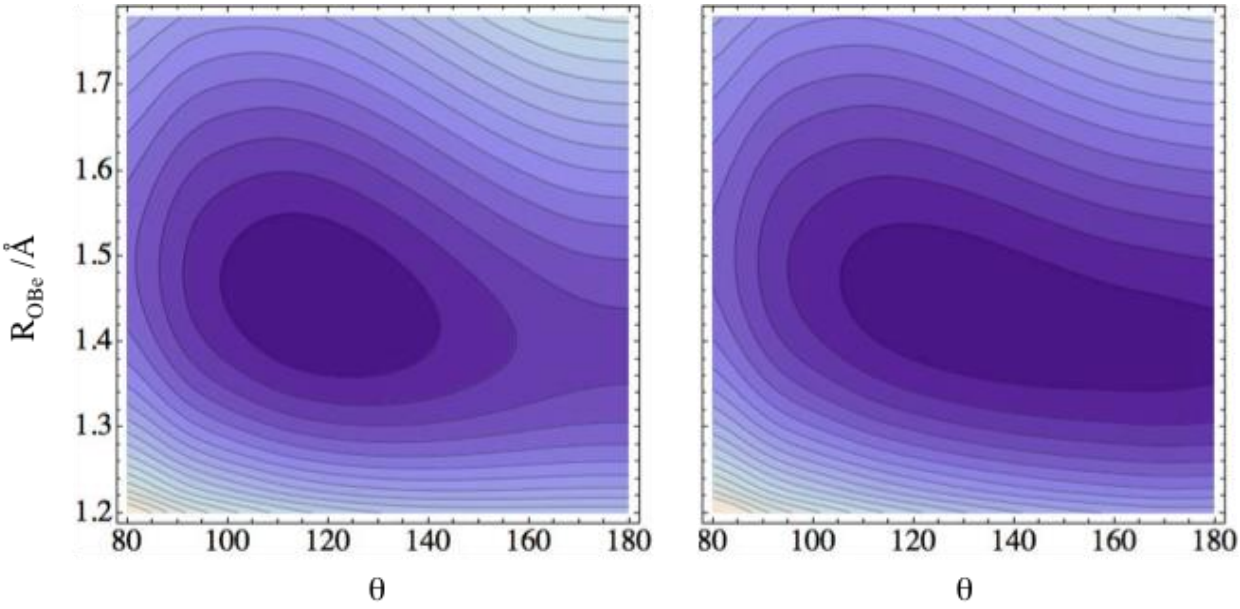

Figure 2. Potential energy contour plots for the $2^2A'$ (left) and $1^2A''$ (right) states of BeOH (R_{HO}=0.95 Å). The contour lines are drawn at 1000 cm^{-1} intervals, relative to the minimum of the $2^2A'$ state. The lowest energy contour line of the $1^2A'$ surface corresponds to 3000 cm^{-1}.

the potential function expansion coefficients. As the data obtained in the experimental part of this study mostly characterize the electronically excited state, we provide the coefficients for the $2^2A'$ and $1^2A''$ state surfaces in Table 2. The standard deviation for the simultaneous fit to all 660 points of the two surfaces was 33 cm^{-1}.

Calculations for the ground state yielded a pattern of energy levels that was similar to that obtained by Koput and Peterson[6]. Here we label the H-O stretch, the bend, and the O-Be stretch using the quantum number labels v_1, v_2, and v_3. As the molecule executes a large amplitude bend in this state, the levels are approximately equivalent to those of a linear molecule. The fundamental vibrational intervals for the H-O and O-Be stretches were 3975, and 1267 cm^{-1}, respectively (2931 and 1251 cm^{-1} for BeOD). Excitation of the bending mode (v_2=1) yields a state with a projection of the angular momentum along the a-axis of ±1 (denoted by the unsigned quantum number K_a in the following). This state was at 90 (BeOH) and 50 cm^{-1} (BeOD). These values were somewhat lower than Koput and Peterson's[6] predictions of 100 and 58 cm^{-1}. Zero-point energies from the MORBID calculations were 2836 (BeOH) and 2246 cm^{-1} (BeOD).

To facilitate discussion of the rotational structure we define N as the quantum number for angular momentum, exclusive of electron and nuclear spin. The total angular momentum, $\vec{J}$ (exclusive of nuclear spin), is given by the vector sum of $\vec{N}$ and the electron spin, $\vec{S}$.

The levels with J=N+1/2 and J=N-1/2 are labeled as $F_1(J)$ and $F_2(J)$, respectively. Our analysis of the predicted rotational structure pertains to levels with N=0 - 5, as this was the range observed for jet-cooled BeOH/D. Spin-rotation coupling was not included

Table 2. Potential energy surface expansion coefficients for the 2^2A' and 1^2A" states of BeOH.

$R_{HO}^{(ref)}$/Å	0.936914	$R_{OBc}^{(ref)}$/Å	1.393966
a_1/Å^{-1}	2.20	a_3/Å^{-1}	1.76
f_{11}	52616.506	f_{33}	47146.401
f_{111}	−442.11135	f_{333}	−115.38494

	A′ surface	A″ surface
$f_0^{(1)}$	−9929.3062	−3002.7012
$f_0^{(2)}$	11785.571	9020.317
$f_0^{(3)}$	−2465.1859	−6532.0545
$f_0^{(4)}$	1205.8996	3998.4399

	A′ surface	A″ surface		A′ surface	A″ surface
$f_1^{(1)}$	−6549.6897	−3921.3821	$f_3^{(1)}$	−20229.524	−23422.812
$f_1^{(2)}$	3330.3246	−2387.789	$f_3^{(2)}$	7955.0694	11422.061
$f_1^{(3)}$	0	0	$f_3^{(3)}$	409.95981	−796.38732
$f_1^{(4)}$	0	0	$f_3^{(4)}$	−1459.6534	−1413.1003
$f_{11}^{(1)}$	−14883.412	1285.3227	$f_{33}^{(1)}$	5058.5048	−6764.3697
$f_{11}^{(2)}$	15469.468	−12006.303	$f_{33}^{(2)}$	−5470.9831	12966.755
$f_{11}^{(3)}$	0	0	$f_{33}^{(3)}$	542.46579	−7456.1833
$f_{111}^{(1)}$	0	0	$f_{333}^{(1)}$	−873.0604	−2868.671
$f_{111}^{(2)}$	0	0	$f_{333}^{(2)}$	768.59156	1343.1058

[a]Parameters are in cm^{-1} unless otherwise specified. The coefficients are defined in ref 47.

in the model, and the rotational structure for the zero-point level was well represented by the expression

$$E_{rot}(N) = \overline{B}N(N+1) \quad (1)$$

with $\overline{B}$ (formally (B+C)/2) values of 1.2948 (BeOH) and 1.1553 cm^{-1} (BeOD). The effective Hamiltonian for a near-prolate asymmetric rotor,

$$\hat{H}_{AR} = A\hat{N}_a^2 + \overline{B}(\hat{N}^2 - \hat{N}_a^2) + \frac{\delta B}{4}(\hat{N}_+^2 + \hat{N}_-^2) \quad (2)$$

where $\delta B=(B-C)$, was used as a model to parameterize the $v_2=1$ levels. The eigenvalues of Eq. 2 were obtained using the spectral simulation program PGOPHER[48]. The energy levels predicted by the MORBID calculations were consistent with the $\overline{B}$ constants given above and values for δB of 0.045 (BeOH) and 0.060 cm^{-1} (BeOD). The energies of the $v_2=1$, N=1 levels were reproduced using values for the A constants of 89.0 (BeOH) and 48.9 (BeOD) cm^{-1}. It is important to recognize these ground state A constants are fitting parameters that are useful for comparison to experimental data. They do not provide a well defined reflection of simple physical properties such as the bending frequency or the a-axis moment of inertia, but are influenced by both.

The potential energy surface for the $2^2A'$ surface has a substantial barrier to linearity, such that the lower energy vibrational levels can be described in terms of a bent molecule model. The fundamental vibrational intervals were predicted to be 3842, 782, and 1182 cm^{-1} (BeOH, zero-point energy = 2993 cm^{-1}) and 2835, 600 and 1156 cm^{-1} (BeOD, zero-point energy = 2349 cm^{-1}). The RENNER calculations included spin-orbit coupling using a single value of 13.4 cm^{-1} for the coupling constant. As for the ground

state, spin-rotation interactions were not included. The spectroscopic data included transitions that accessed excited state K_a=0, 1, and 2 levels. Predicted rotational energies for the $2^2A'$ (0,0,0) levels of BeOH and BeOD are presented in Tables 3 and 4. The spin-orbit coupling was mostly quenched near the equilibrium bond angle, so the angular momentum coupling was close to the Hund's case b limit. The effective zero-point rotational constants were A=27.0, $\overline{B}$ =1.257, δB=0.05 (BeOH) and A=15.2, $\overline{B}$ =1.153, δB=0.08 cm^{-1} (BeOD). The values for δB were close to those estimated using the equilibrium coordinates (0.060 and 0.090 cm^{-1}).

The energy of the zero-point level of $1^2A''$, relative to that of the $2^2A'$ state was predicted to be 2103 (BeOH) and 2118 cm^{-1} (BeOD). As this energy range was not accessed in our experiments, we do not describe the energy level characteristics of $1^2A''$ potential energy surface here.

At the ground state equilibrium geometry, the sa-CASSCF calculations yielded values for the electric dipole transition moments of $\left|\langle 2\ ^2A'|\mu_b|1\ ^2A'\rangle\right|$=3.8 D and $\left|\langle 2\ ^2A'|\mu_a|1\ ^2A'\rangle\right|$=0.14 D. Hence, the transition is expected to follow b-type selection rules ($\Delta K_a=\pm1$, $\Delta J=0, \pm1$), and the allowed bands originating from cold BeOH/D should correspond to $K_a'=1\leftarrow K_a''=0$. When this selection rule is taken into account, the calculations described above predict that the lowest energy feature arising from the zero-point level of the ground state will be at 31532 (BeOH) and 31466 cm^{-1} (BeOD), defining an isotope shift of 66 cm^{-1}.

Table 3. Calculated and fitted rotational energy levels of the 2^2A' (0,0,0) state of BeOH

		F_1(A')	F_1(A")	F_2(A')	F_2(A")
K_a=0,	N				
	0			0.00	
	1		2.51 (2.50)		2.51 (2.50)
	2	7.54 (7.50)		7.54 (7.50)	
	3		15.08 (15.01)		15.08 (15.01)
	4	25.13 (25.01)		25.13 (25.01)	
K_a=1,	N				
	1	28.41 (27.39)	28.36 (27.35)	27.91 (27.01)	27.85 (26.97)
	2	33.27 (32.40)	33.44 (32.54)	33.01 (32.06)	33.19 (32.21)
	3	41.04 (39.96)	40.69 (39.67)	40.86 (39.82)	40.52 (39.54)
	4	50.61 (49.57)	51.19 (50.05)	50.47 (49.46)	51.05 (49.94)
K_a=2,	N				
	2	110.28 (106.82)	110.28 (106.82)	109.19 (105.98)	109.19 (105.98)
	3	117.70 (114.24)	117.70 (114.24)	116.98 (113.68)	116.98 (113.68)
	4	127.67 (124.20)	127.67 (124.20)	127.13 (123.77)	127.13 (123.77)

Energies are in cm^{-1} units. The numbers in parentheses were generated from fitted molecular constants. See text for details.

Table 4. Calculated and fitted rotational energy levels of the 2^2A' (0,0,0) state of BeOD

		F_1(A')	F_1(A'')	F_2(A')	F_2(A'')
K_a=0,	N				
	0			0.00	
	1		2.31 (2.30)		2.31 (2.30)
	2	6.92 (6.91)		6.92 (6.91)	
	3		13.84 (13.82)		13.84 (13.82)
	4	23.05 (23.03)		23.05 (23.03)	
K_a=1,	N				
	1	16.56 (16.00)	16.47 (15.91)	16.28 (15.81)	16.19 (15.72)
	2	20.96 (20.40)	21.23 (20.67)	20.81 (20.31)	21.08 (20.58)
	3	28.27 (27.71)	27.72 (27.17)	28.16 (27.64)	27.62 (27.10)
	4	36.75 (36.20)	37.66 (37.10)	36.68 (36.15)	37.58 (37.05)
K_a=2,	N				
	2	63.41 (61.42)	63.41 (61.42)	62.81 (61.01)	62.81 (61.01)
	3	70.26 (68.30)	70.26 (68.30)	69.85 (68.02)	69.85 (68.02)
	4	79.45 (77.49)	79.45 (77.49)	79.14 (77.28)	79.14 (77.28)

Energies are in cm^{-1} units. The numbers in parentheses were generated from fitted molecular constants. See text for details.

Here we correct a misstatement concerning the transition type made in the preliminary discussion of the spectrum by Heaven et al.[29] It was noted that the prominent Q-branches seen in the spectra were indicative of a perpendicular transition (relative to the a-axis), which therefore constrained the upper state to be of A" symmetry. The first part of this assertion was correct, but the symmetry implication is not. As demonstrated below, the Q-branch intensities are consistent with b-type selection rules for a ^{2}A'-^{2}A' transition.

3.4 Experimental Results and Analyses

Figure 3 shows low-resolution survey scans for BeOH and BeOD recorded using REMPI detection. Over the energy range examined (30300-32800 cm^{-1}), the spectra exhibited a dominant vibrational progression with average intervals of 730 cm^{-1} (BeOH) and 560 cm^{-1} (BeOD). Weaker features were present, in positions that were consistent with those predicted for the sub-bands associated with the main progression. From the band spacings and the isotope shifts, the main progression could be unambiguously assigned to the bending mode. Transitions involving excitation of the H-O stretch were not observed in this study, so we label the excited state vibrational levels using the notation (v_2, v_3)K_a.

An expanded scan of the 30840-31015 cm^{-1} region, recorded using LIF, is shown in Fig. 4. DNO_3 was used as the hydroxyl source for this experiment, but bands of both BeOD and BeOH were clearly present. For these conditions the bands showed partially resolved rotational structure. The central feature of this trace is the $K_a'=1\leftarrow K_a''=0$ sub-

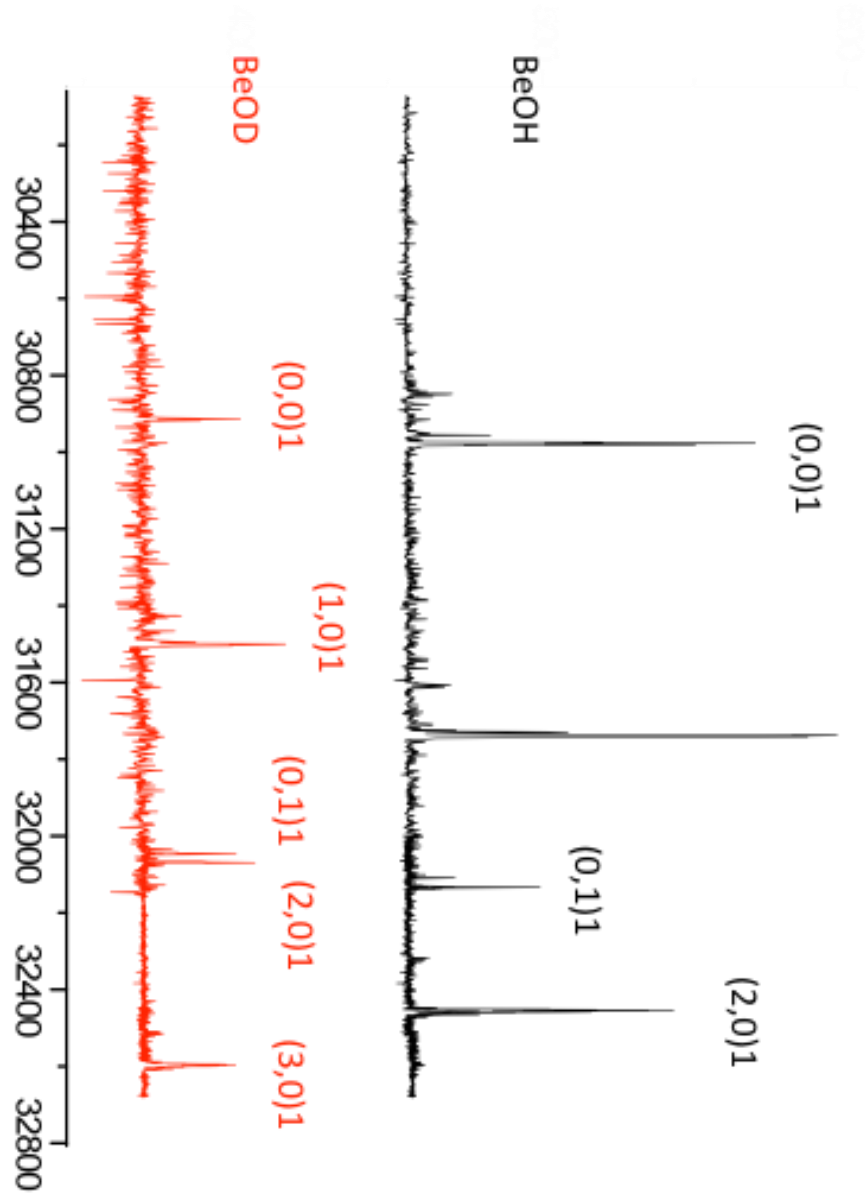

Figure 3. Low resolution REMPI survey spectra for BeOH and BeOD

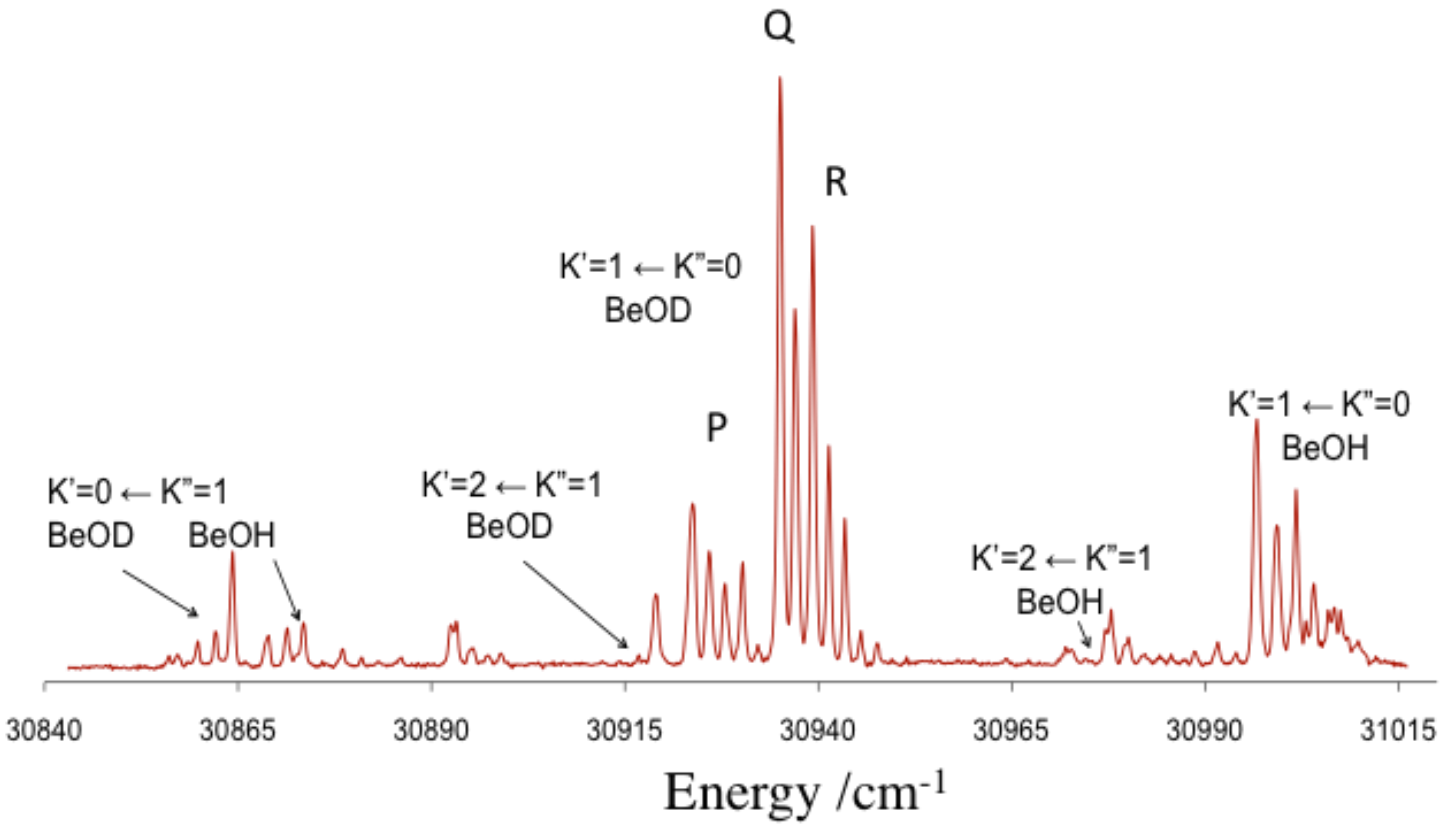

Figure 4. Laser induced fluorescence spectrum for a mixture of BeOH and BeOD

band of the BeOD origin transition. The P-, Q-, and R-branch structure of this band, along with the relative branch intensities, confirm that this is a ΔK_a=+1 transition. The equivalent band for BeOH can be seen at the high frequency end of Fig. 4. As discussed below, the P-branch regions of the K_a'=1←K_a''=0 sub-bands also include additional lines that belong to the K_a'=2←K_a''=1 sub-bands. The ΔK_a=-1 transitions arising from K_a''=1 are also present in this trace, with Q-branch features near 30874 (BeOH) and 30864 cm^{-1} (BeOD). As expected for ΔK_a=-1, the P-branch lines were more intense than those of the R-branch. The first lines of each branch, labeled using the N quantum number, were P(1) and R(1) for the ΔK_a=-1 sub bands and P(2) and R(0) for the K_a'=1←K_a''=0 sub-bands, confirming the K_a assignments.

Higher resolution spectra for the origin bands were recorded using an intracavity etalon to reduce the laser linewidth. Figures 5 and 6 present the more intense lines of the K_a'=1←K_a''=0 sub-bands, where the low-N lines show spin splitting. Modeling of the higher resolution spectra was carried out using the program PGOPHER[48]. Both the ground and excited states were represented using the rigid near prolate top Hamiltonian given by Eq. 2. The spin-splitting in the 2^2A' state was reproduced by adding the term arising from the a-axis spin-rotation interaction (ε_{aa})[48,49]. Examples of the fitting are shown as the downward-going traces in Fig.'s 5 and 6. All fits were carried out using the least squares fitting capabilities of PGOPHER[48]. The rotational temperature was set to 8 K. Initial fitting of the K_a'=1←K_a''=0 sub-bands was accomplished by varying ν_0 (the band origin), $\overline{B}''$, $\overline{B}'$ and ε'_{aa}. The parameters A', A'', δB' and δB'' were held at the values derived from the theoretical calculations. This yielded fits with standard deviation below 0.05 cm^{-1}. In the next step, data for the K_a'=0←K_a''=1 and K_a'=2←K_a''=1 sub-bands were

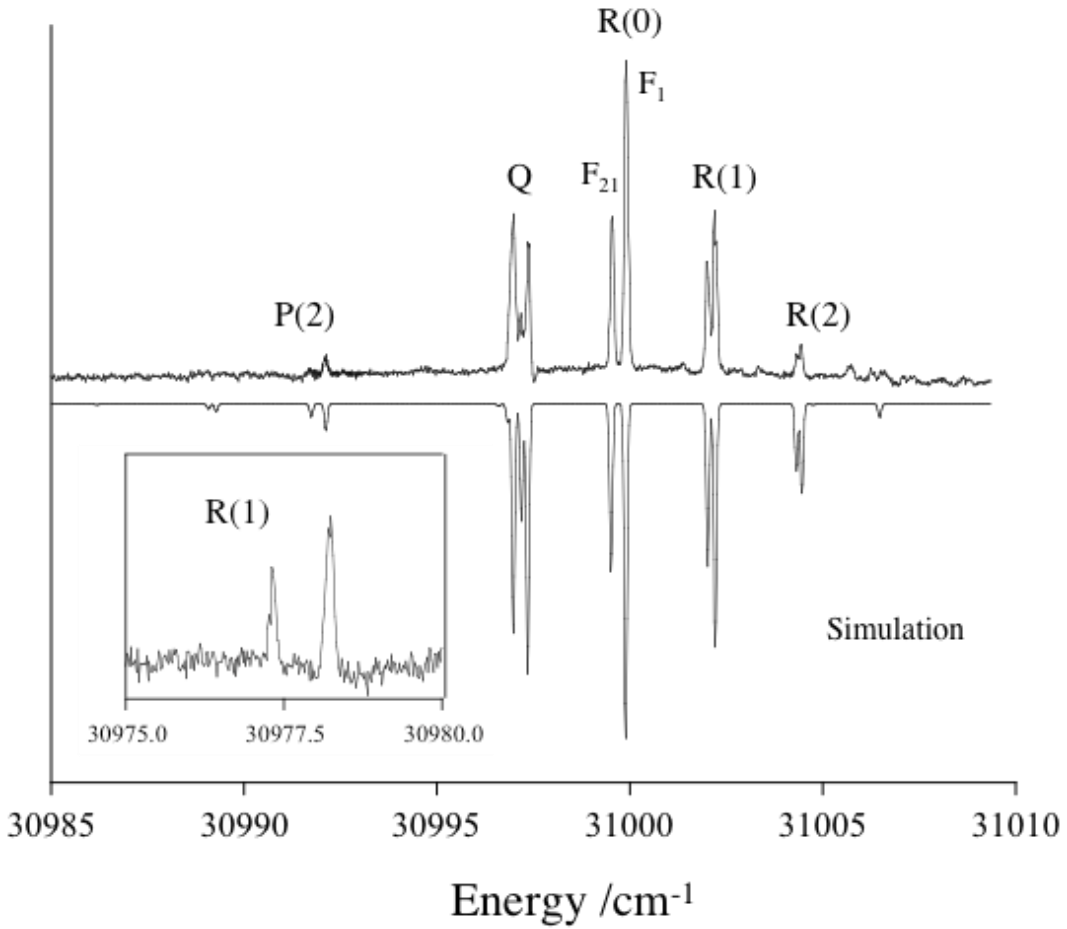

Figure 5. High-resolution LIF spectrum for the origin band of the $2^2A'$-$1^2A'$ transition of BeOH. The upper trace shows the rotational lines of the K_a=1-K_a=0 sub-band, while the insert show the R(1) feature of the the K_a=2-K_a=1 sub-band. The downward-going trace is a simulation based on the constants given in Tables 5 and 6.

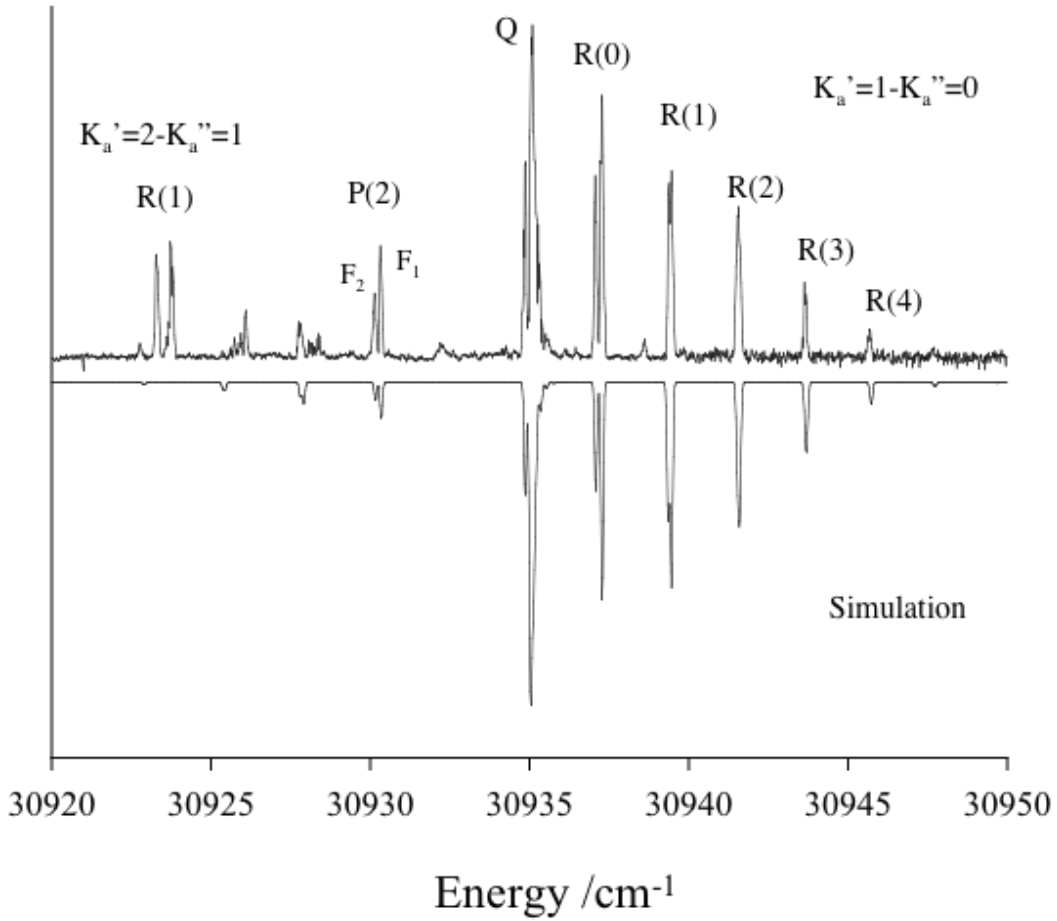

Figure 6. High-resolution LIF spectrum for the origin band of the $2^2A'$-$1^2A'$ transition of BeOD. The upper trace shows the rotational lines of the K_a=1-K_a=0 and 2-1 sub-bands, The downward-going trace is a simulation based on the constants given in Tables 5 and 7.

included, and all of the parameters listed above were treated as variables. In this model the spin-splittings were determined by ε'_{aa} while the combination defect (displacement of the Q-branch relative to the P- and R- branches) was controlled by δB' and δB". At this stage the dependence of $\overline{B}$ on K_a was neglected. For the ground state, this proved to be an acceptable approximation. However, for the BeOH origin the fits were improved when the excited state $\overline{B}$ constant was slightly decreased for K_a'=0.

Due to correlations between the upper and lower state constants, fits where all of the constants were allowed to vary simultaneously were often unstable, yielding physically unreasonable parameter values. Consequently, multiple fits were carried out to systematically refine the constants by freezing out different sub-groups. With this approach the standard deviation for the constants from the constrained fits were artificially low. The uncertainties given in Tables 5, 6 and 7 were estimated by exploring the range of value choices for a given constant that could be accommodated by physically reasonable adjustments of correlated constants.

The best fit molecular constants for the ground states of BeOH and BeOD, derived from the higher resolution spectra, are presented in Table 5. Note the large values for the A" constants, which are consistent with the present theoretical calculations and those of Koput and Peterson[6]. The observation of transitions from K_a"=1 indicates that the K_a population distribution was not in thermal equilibrium with the N-based rotational distributions.

The system of K_a'= 0, 1, and 2 sub-bands described for the origin was also observed in association with the v_2= 1 and 2 levels of BeOH, and the v_2=1, 2, and 3 levels of BeOD. In addition, the sub-bands of the v_3=1 O-Be stretch were recorded for both isotopologues.

Table 5. Ground state properties of BeOH and BeOD

Property	BeOH	BeOD	Source
A	99.9(1)	57.9(1)	*a*
$\overline{B}$	1.295(4)	1.155(4)	*a*
δB	0.04(2)	0.06(2)	*a*
$E(K_a=1, N=1)$	101.2(2)	59.0(2)	*a*
$E(K_a=1, N=1)$	99.9	58.1	*b*
$E(K_a=1, N=1)$	90.1	49.9	*c*

a. Experimental values in units of cm^{-1}.

b. Theoretical calculations of Koput and Peterson[6]

c. Present theoretical calculations

Table 6. Molecular constants for the 2^2A' state of BeOH

$(v_2,v_3)K_a$	ν_0	A	$\overline{B}$	δB	ε_{aa}
(0,0)0	30972.6(1)	26.0(1)	1.251(4)	0.05(1)	0.52(6)
(0,0)1	"	"	"	"	"
(0,0)2	"	"	1.261(4)	"	"
(1,0)0	31719.9(2)	30.2(2)	1.260(5)	0.07(2)	0.70(8)
(1,0)1	"	"	1.240(5)	"	"
(1,0)2	"	"	1.240(5)	"	"
(0,1)1	32106.2(2)	27.2(2)	1.257(5)	0.05(2)	0.5(1)
(2,0)0	32425.6(2)	32.3(2)	1.220(5)	0.05(2)	1.7(1)
(2,0)1	"	"	1.261(5)	"	"
(2,0)2	"	"	1.261(5)	"	"

Constants in units of cm^{-1}

Table 7. Molecular constants for the 2^2A' state of BeOD

$(v_2,v_3)K_a$	ν_0	A	$\overline{B}$	δB	ε_{aa}
(0,0)0	30921.4(1)	14.7(1)	1.152(4)	0.09(1)	0.25(6)
(0,0)1	"	"	"	"	"
(0,0)2	"	"	"	"	"
(1,0)0	31499.2(2)	16.8(2)	1.160(5)	0.09(2)	0.25(8)
(1,0)1	"	"	1.152(5)	"	"
(1,0)2	"	"	1.152(5)	"	"
(0,1)0	32038.6(2)	15.4(2)	1.139(5)	0.06(2)	0.25(8)
(0,1)1	"	"	"	"	"
(0,1)2	"	"	"	"	"
(2,0)0	32058.5(2)	18.5(2)	1.140(5)	0.09(2)	0.25(8)
(2,0)1	"	"	"	"	"
(2,0)2	"	"	"	"	"
(3,0)1	32572.2(2)	22.1(2)	1.152(5)	0.10(2)	0.25(8)
(3,0)2	"	"	"	"	"

Constants in units of cm^{-1}

Table 8. Vibrational intervals for the 2^2A' state of BeOH/D

Isotopologue	Interval	Observed	Calculated
BeOH	(1,0)-(0,0)	747.3(3)	782.4
"	(2,0)-(1,0)	705.7(3)	736.3
"	(0,1)-(0,0)	1140.0(3)	1181.9
BeOD	(1,0)-(0,0)	577.8(3)	600.5
"	(2,0)-(1,0)	559.3(3)	573.7
"	(3,0)-(2,0)	513.7(3)	536.1
"	(0,1)-(0,0)	1117.2(3)	1156.5

Energies in units of cm^{-1}.

These vibrationally excited levels were recorded at a resolution of 0.5 cm^{-1}, which was sufficient to resolve the rotational lines, and partially resolve some of the spin-splittings. In fitting these data the molecular constants for the ground states were held fixed at the values given in Table 5. Excited state molecular constants are listed in Table 6 for BeOH and Table 7 for BeOD. The band origin (ν_0) values in these Tables correspond to the hypothetical $N'=K_a'=0 \leftarrow N''=K_a''=0$ transitions. Vibrational intervals for the $2^2A'$ state, derived from the ν_0 values, are listed in Table 8.

The ionization energy (IE) of BeOH was determined by recording the two-photon ionization efficiency spectrum. For this measurement the first laser was tuned to the R(0) line of the $K_a'=1 \leftarrow K_a''=0$ origin band at 30999.5 cm^{-1}. The second laser, which was temporally overlapped with the first, was tuned through the energy range where ionization was expected[8,10]. The result of this scan is shown as the upper trace in Fig. 7, where the lowest energy feature observed is marked with an arrow. The lower trace in Fig. 7 was recorded with a delay of 20 ns between the two laser pulses. This was done to check for features that might have arisen from one-color, two-photon ionization. None were detected at the threshold energy. The ionization spectrum shows resolved structure resulting from autoionizing resonances. The first prominent feature, used here to determine the IE, also appears to be a resonance. This spectrum was recorded in an electric field of F=145 V/cm. Correcting the threshold energy for the field, by means of the expression[50] $\Delta E(cm^{-1}) = 6\sqrt{F(V/cm)}$, yielded an IE of 66425 cm^{-1}. Taking into account the uncertainties associated with the determination of the low-energy edge of the first feature, we estimate that the error range for IE is ± 10 cm^{-1}.

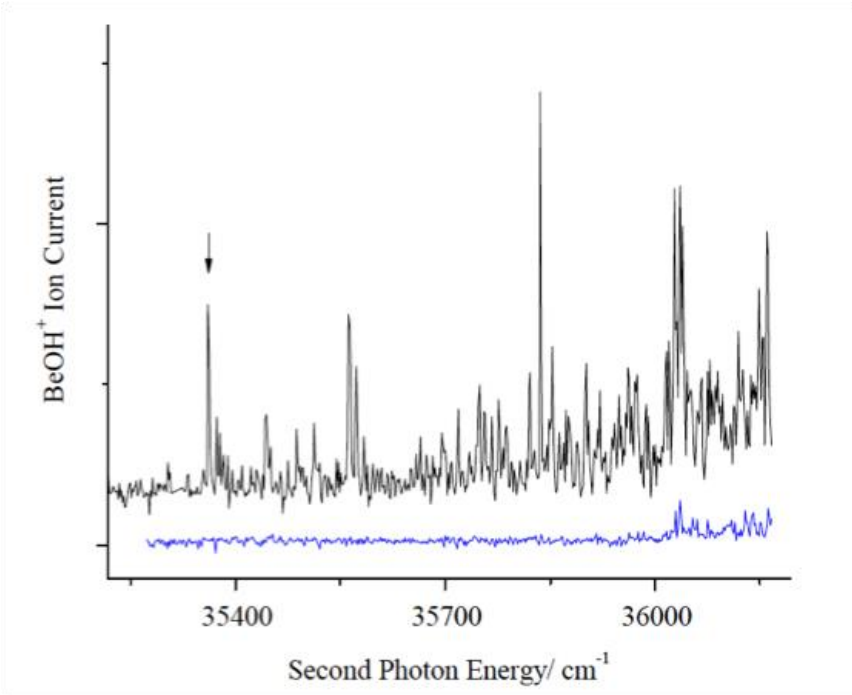

Figure 7. Photoionization efficiency spectrum for BeOH. The first laser was tuned to the R(0) line of the K_a'=1-K_a"=0 band at 30999.5 cm^{-1}

3.5 Discussion

The level of agreement between the theoretically predicted properties of BeOH/D and the near UV band system was sufficient to achieve unambiguous assignment of the observed ro-vibronic features. The ground state $\overline{B}$ constants derived from both the present calculations and those of Koput and Peterson[6] were within the error limits of the values determined from our highest resolution spectra. The measured intervals between the K_a"=1 and K_a"=0 levels were higher than both the predictions of Koput and Peterson[6] and the present calculations, with the former being closer to the experimental values. Although the present calculations yielded a higher barrier to linearity, we found that it was primarily the behavior of the effective bending potential at the outer turning points (smaller values for θ) that determined the K_a" 1-0 intervals. One-dimensional cuts through the potential energy surfaces showed that the surface of Koput and Peterson[6] was steeper at smaller angles, producing larger spacings. Based on this analysis, it seems that the surface generated from the RCCSD(T) calculations of Koput and Peterson[6] is of better quality than our CASSCF/MRCI+Q results. This may be attributed to the larger size basis sets used in the former study (up to aug-cc-pV5Z) combined with optimization that was focused on just the ground state. The agreement between the experimental and theoretical results is close enough to confirm that the ground state zero-point level of BeOH/D is quasilinear.

Our theoretical calculations predicted that the first Q-branch line of the $2^2A'$-$1^2A'$ origin transition (K_a'=1-K_a"=0 sub-band) would be observed at 31497 (BeOH) and 31443 cm^{-1} (BeOD). These values overestimated the experimental results by 500 and 508 cm^{-1}, which is an acceptable level of agreement for an electronic transition energy of this

magnitude. The measured and calculated isotopic shifts (62 vs. 54 cm^{-1}, determined using the Q(1) lines) were also in respectable agreement. The adiabatic excitation energy predicted by Theodorakopoulos et al.[8] (31620 cm^{-1}) and the vertical energy of Zaidi et al.[10] (31940 cm^{-1}) are also consistent with the experimental results.

For the zero-point levels of BeOH/D $2^2A'$, comparisons of the observed and predicted rotational energies are presented in Tables 3 and 4. The experimentally determined energies, which are given in parentheses, were generated using the fitted molecular constants from Tables 3 and 4. Energy intervals associated with the $\overline{B}'$ molecular constant were found to be very close to the measured values. The predicted spacings between the K_a'=0, 1, and 2 manifolds were slightly too large. As noted above, BeOH/D can be treated as a bent molecule for levels near the bottom of the $2^2A'$ state. Consequently, the K_a' spacings can be related, via the A rotational constant, to the average bond angle. The calculated A constants were overestimated by an amount which indicated that the vibrationally averaged bond angle of the theoretical calculation was too large by 1.5 (BeOH) and 1.3 degrees (BeOD). The $2^2A'$ state spin splittings were adequately reproduced by the RENNER calculations using A_{SO}=13.4 cm^{-1}.

From Tables 6 and 7 it can be seen that the A constants increased with increasing excitation of the bending mode. This trend was also exhibited by the theoretical calculations, which yielded A constants for $2^2A'$ BeOH(D) of 27.2(15.4), 31.9(17.8), 32.4(19.4) and (22.2) cm^{-1} for v_2=0, 1, 2, and 3. The calculated and measured intervals between successive bending levels, and the frequencies for the O-Be stretch fundamental are presented in Table 8. Here it can be seen that the bending mode was markedly anharmonic. The frequencies of both the bending levels and the O-Be stretch

fundamentals were overestimated by the calculations, indicating that the potential energy surface is somewhat too steep for motions along these vibrational coordinates. Despite this shortcoming, the predictions for vibrationally excited levels were close enough to the experimental data to provide the correct ordering for the nearby (0,1) and (2,0) states of BeOD (c.f. Fig. 3). Assignment of the experimental data for these two bands was based on the behavior of the A constants.

As part of their study of the HBeO isomer, Zaidi et al.[10] reported a vertical excitation energy for BeOH of 31940 cm^{-1} for the $2^2A'$-$1^2A'$ transition, derived from a large-scale sa-CASSCF/MRCI+Q calculation that included correlation of the Be 1s electrons. The present calculations are in reasonably good agreement with this result and both are consistent with the experimental observations. Theodorakopoulos et al.[8] carried out a more extensive study of the $2^2A'$ potential energy surfaces. Their equilibrium parameters (determined with R_{H-O} fixed at 0.9435 Å) were R_{O-Be}=1.48 Å and θ=116 degrees, with a barrier to linearity of 3710 cm^{-1}. Compared with the properties given in Table 1, the smaller bond angle of Theodorakopoulos et al.[8] is in better agreement with the experimentally determined A constants, while the equilibrium bond length provided by the present calculations is in better agreement with the observed $\overline{B}$ constants. The barrier heights predicted by the present calculations and those of Theodorakopoulos et al.[8] are significantly different. As the latter study did not report vibrational energies, it is difficult to know if their potential energy surface is consistent with the spectroscopic data. Although the present calculations yielded a lower energy barrier, the potential surface led to bending frequencies that were too high. Examination of the angular cut through the potential energy surface of Theodorakopoulos et al. (Fig. 4 of ref. [8]) indicate

that this surface will also overestimate the bending frequency, and that the irregular shape of the curve near 140 degrees may produce erratic vibrational intervals.

Theodorakopoulos et al.[8] estimated the IE of BeOH by considering the energy difference between the minimum energy linear structures for BeOH and $BeOH^+$. Geometry optimization confirmed the expected linear geometry of the cation. Given the low barrier to linearity for the ground state of BeOH, the IE of the linear molecule should provide a good approximation for the adiabatic IE. The present measurements established an IE of 66425(10) cm^{-1}. Assuming that the zero-point energies of BeOH and $BeOH^+$ are comparable, the calculated value of 65330 cm^{-1} is found to be reasonably accurate.

3.6 Conclusions

Comparison of the spectroscopic data and theoretical calculations for BeOH/D confirms earlier predictions that the molecule is quasilinear in the ground state. The potential energy surface has a bent equilibrium geometry, but the zero-point vibrational level lies well above the barrier to linearity. These findings support the expectation that bonding in BeOH has a greater degree of covalency than is found for any of the other alkaline earth monohydroxides[1]. The ground state potential energy surface and ro-vibronic eigenstate calculations of Koput and Peterson[6] were found to be in very good agreement with the experimental data.

The electronic transition observed in this study, $2^2A'$-$1^2A'$, can be attributed to a mostly Be-centered 2p-2s electron promotion. The $2^2A'$ potential energy surface has a

bent equilibrium structure with a moderately high barrier to linearity. As a consequence, the lower energy ro-vibronic levels follow the behavior expected for a bent molecule. Theoretical calculations were used to predict the potential energy surface and the ro-vibronic eigenstates of the 2^2A' state. The results were in respectable agreement with the spectroscopic data and the characteristics of the surface were broadly in agreement with the results from a previously published MRCI calculation[8]. The favorable comparison indicates that the low-lying electronically excited states of BeOH can be predicted with a useful level of confidence using multi-reference electronic structure techniques.

3.7 Acknowledgements

The work conducted at Emory University was supported by the NSF under grant CHE-0956442. The electronic structure calculations reported here were carried out using the resources of the Cherry Emerson Center for Scientific Computation, which is supported by the NSF MRI-R2 grant CHE-0958205. The work of Per Jensen is supported in part by the Deutsche Forschungsgemeinschaft and the Fonds der Chemischen Industrie

3.8 References to Chapter 3

(1) Bauschlicher, C.W., Jr.; Langhoff, S.R.; Partridge, H. "Ab Initio Study of the Alkali and Alkaline-Earth Monohydroxides", *J. Chem. Phys.* **1986**, *84*, 901-909.
(2) Bauschlicher, C.W., Jr.; Langhoff, S.R.; Steimle, T.C.; Shirley, J.E. "The Permanent Electric Dipole Moment of Calcium Hydroxide (CaOH)", *J. Chem. Phys.* **1990**, *93*, 4179-4186.
(3) Hinchliffe, A. "Structure and Electronic Properties of the Radicals BeOH and MgOH", *J. Mol. Struct.* **1980**, *64*, 289-292.
(4) Koput, J.; Carter, S.; Peterson, K.A.; Theodorakopoulos, G. "The Ab Initio Potential Energy Surface and Vibrational-Rotational Energy Levels of $X^2\Pi^+$ MgOH", *J. Chem. Phys.* **2002**, *117*, 1529-1535.
(5) Koput, J.; Peterson, K.A. "Ab Initio Potential Energy Surface and Vibrational-Rotational Energy Levels of $X^2\Pi^+$ CaOH", *J. Phys. Chem. A* **2002**, *106*, 9595-9599.
(6) Koput, J.; Peterson, K.A. "Ab Initio Prediction of the Potential Energy Surface and Vibrational-Rotational Energy Levels of X^2A' BeOH", *J. Phys. Chem. A* **2003**, *107*, 3981-3986.
(7) Palke, W.E.; Kirtman, B. "Calculations of the Bending Potentials of Magnesium Hydroxide (MgOH) and Beryllium Hydroxide (BeOH)", *Chem. Phys. Lett.* **1985**, *117*, 424-426.
(8) Theodorakopoulos, G.; Petsalakis, I.D.; Hamilton, I.P. "Ab Initio Calculations on the Ground and Excited States of BeOH and MgOH", *J. Chem. Phys.* **1999**, *111*, 10484-10490.
(9) Theodorakopoulos, G.; Petsalakis, I.D.; Liebermann, H.-P.; Buenker, R.J.; Koput, J. "Ab Initio Calculations on Electronic States of CaOH", *J. Chem. Phys.* **2002**, *117*, 4810-4819.
(10) Zaidi, A.; Lahmar, S.; Ben Lakhdar, Z.; Rosmus, P.; Chambaud, G. "Theoretical Study of HBeO", *Chem. Phys.* **2006**, *321*, 41-47.
(11) Vasiliu, M.; Feller, D.; Gole, J.L.; Dixon, D.A. "Structures and Heats of Formation of Simple Alkaline Earth Metal Compounds: Fluorides, Chlorides, Oxides, and Hydroxides for Be, Mg, and Ca", *J. Phys. Chem. A* **2010**, *114*, 9349-9358.
(12) Antic-Jovanovic, A.; Bojovic, V.; Pesic, D. "Electronic Bands of Beryllium Hydroxide (BeOH and BeOD)", *Spectrosc. Lett.* **1988**, *21*, 757-765.
(13) Ziurys, L.M.; Fletcher, D.A.; Anderson, M.A.; Barclay, W.L., Jr. "Rest Frequencies for Alkaline Earth Hydroxide Radicals ($X^2\Pi^+$)", *Astrophys. J., Suppl. Ser.* **1996**, *102*, 425-434.
(14) Fletcher, D.A.; Anderson, M.A.; Barclay, W.L., Jr.; Ziurys, L.M. "Millimeter-Wave Spectroscopy of Vibrationally Excited Ground State Alkaline-Earth Hydroxide Radicals ($X^2\Pi^+$)", *J. Chem. Phys.* **1995**, *102*, 4334-4339.
(15) Brom, J.M., Jr.; Weltner, W., Jr. "ESR Spectrum and Structure of the Magnesium Hydroxide Radical", *J. Chem. Phys.* **1973**, *58*, 5322-5330.
(16) Brom, J.M., Jr.; Weltner, W., Jr. "ESR Spectrum of the Beryllium Hydroxide (BeOH) Molecule", *J. Chem. Phys.* **1976**, *64*, 3894-3895.
(17) Ni, Y., "Laser Spectroscopy and Structure of Magnesium Hydroxide and Deuterated Magnesium Hydroxide: The A-X System", Ph.D. Thesis, Chemistry, University of California, Santa Barbara: Santa Barbara, CA. **1986**, pp. 127.

(18) Bunker, P.R.; Kolbuszewski, M.; Jensen, P.; Brumm, M.; Anderson, M.A.; Barclay, W.L., Jr.; Ziurys, L.M.; Ni, Y.; Harris, D.O. "New Rovibrational Data for MgOH and MgOD and the Internuclear Potential Function of the Ground Electronic State", *Chem. Phys. Lett.* **1995**, *239*, 217-222.
(19) Tandy, J.D.; Wang, J.G.; Bernath, P.F. "High-Resolution Laser Spectroscopy of BaOH and BaOD: Anomalous Spin-Orbit Coupling in the $A^2\Pi$ State", *J. Mol. Spectrosc.* **2009**, *255*, 63-67.
(20) Wang, J.G.; Dick, M.J.; Sheridan, P.M.; Yu, S.; Bernath, P.F. "Further Spectroscopic Investigations of the High Energy Electronic States of SrOH: The $B'^2\Pi^+$(0 0 0)-$A^2\Pi$(0 0 0) and the $D^2\Pi^+$(0 0 0)-$A^2\Pi$(0 0 0) Transitions", *J. Mol. Spectrosc.* **2007**, *245*, 26-33.
(21) Beardah, M.S.; Ellis, A.M. "Observation of a New $^2\Pi^+$-$^2\Pi^+$ Transition of the SrOH Free Radical", *J. Mol. Spectrosc.* **2003**, *218*, 80-84.
(22) Li, M.; Coxon, J.A. "Dye Laser Excitation Studies of the $A^2\Pi$(100)/(020)-$X^2\Pi^+$(020)/(000) Bands of CaOD: Analysis of the $A^2\Pi$(100)/(020) Fermi Resonance", *J. Chem. Phys.* **1996**, *104*, 4961-4977.
(23) Presunka, P.I.; Coxon, J.A. "Laser Excitation and Dispersed Fluorescence Investigations of the $A^2\Pi$-~$X^2\Pi^+$ System of SrOH", *Chem. Phys.* **1995**, *190*, 97-111.
(24) Anderson, M.A.; Allen, M.D.; Barclay, W.L., Jr.; Ziurys, L.M. "The Millimeter and Sub-Millimeter Spectrum of the BaOH Radical", *Chem. Phys. Lett.* **1993**, *205*, 415-422.
(25) Coxon, J.A.; Li, M.; Presunka, P.I. "Laser Fluorescence Excitation Spectroscopy of Calcium Monohydroxide and Calcium Monodeuteroxide: the $A^2\Pi$-~$X^2\Pi^+$ (100)-(000) Band System and the (100)-(020) Fermi Resonance", *J. Mol. Spectrosc.* **1991**, *150*, 33-45.
(26) Fernando, W.T.M.L.; Douay, M.; Bernath, P.F. "Vibrational Analysis of the $A^2\Pi$-~$X^2\Pi^+$ and $A'^2\Pi$-~$X^2\Pi^+$ Transitions of Barium Hydroxide (BaOH) and Barium Deuteroxide (BaOD)", *J. Mol. Spectrosc.* **1990**, *144*, 344-351.
(27) Kramida, A., Ralchenko, Yu., Reader, J., and NIST ASD Team (2011). NIST Atomic Spectra Database (ver. 5.0). Available: http://physics.nist.gov/asd
(28) Thompson, C.A.; Andrews, L. "Reactions of Laser Ablated Be Atoms with H_2O: Infrared Spectra and Density Functional Calculations of HOBeOH, HBeOH, and HBeOBeH", *J. Phys. Chem.* **1996**, *100*, 12214-12221.
(29) Heaven, M.C.; Bondybey, V.E.; Merritt, J.M.; Kaledin, A.L. "The Unique Bonding Characteristics of Beryllium and the Group IIA Metals", *Chem. Phys. Lett.* **2011**, *506*, 1-14.
(30) Yu, S.; Wang, J.-G.; Sheridan, P.M.; Dick, M.J.; Bernath, P.F. "Laser Spectroscopy of the $A^2\Pi$-$X^2\Pi^+$ 000 and $C^2\Pi$--$A^2\Pi$ 000 Transitions of SrOD", *J. Mol. Spectrosc.* **2006**, *240*, 26-31.
(31) Wang, J.G.; Tandy, J.D.; Bernath, P.F. "High-Resolution Laser Excitation Spectroscopy of the $A^2\Pi$(000)-~$X^2\Pi^+$(000) Transition of BaOH", *J. Mol. Spectrosc.* **2008**, *252*, 31-36.
(32) Li, M.; Coxon, J.A. "High-Resolution Analysis of the Fundamental Bending Vibrations in the $A^2\Pi$ and $X^2\Pi^+$ States of CaOH and CaOD: Deperturbation of Renner-Teller, Spin-Orbit and K-Type Resonance Interactions", *J. Chem. Phys.* **1995**, *102*, 2663-2674.

(33) Merritt, J.M.; Kaledin, A.L.; Bondybey, V.E.; Heaven, M.C. "The Ionization Energy of Be_2, and Spectroscopic Characterization of the (1) $^3\Sigma_u^+$, (2)$^3\Box_g$, and (3)$^3\Box_g$ States", *Phys. Chem. Chem. Phys.* **2008**, *10*, 4006-4013.
(34) Merritt, J.M.; Bondybey, V.E.; Heaven, M.C. "Experimental and Theoretical Study of the Electronic Spectrum of BeAl", *Phys. Chem. Chem. Phys.* **2008**, *10*, 5403-5411.
(35) Salami, H.; Ross, A.J. "A Molecular Iodine Atlas in ASCII Format", *J. Mol. Spectrosc.* **2005**, *233*, 157-159.
(36) MOLPRO, version 2010.1, a package of ab initio programs, H.-J. Werner, P. J. Knowles, R. Lindh, F. R. Manby, M. Schütz, and others.
(37) Widmark, P.O.; Malmqvist, P.; Roos, B.O. "Density Matrix Averaged Atomic Natural Orbital (ANO) Basis Sets for Correlated Molecular Wave Functions. I. First Row Atoms", *Theor. Chim. Acta.* **1990**, *77*, 291-306.
(38) Werner, H.J.; Knowles, P.J. "An efficient internally contracted multiconfiguration-reference configuration interaction method", *J. Chem. Phys.* **1988**, *89*, 5803-5814.
(39) Knowles, P.J.; Werner, H.J. "An efficient method for the evaluation of coupling coefficients in configuration interaction calculations", *Chem. Phys. Lett.* **1988**, *145*, 514-522.
(40) Langhoff, S.R.; Davison, E.R. "Configuration interaction calculations on the nitrogen molecule", *Int. J. Quantum Chem.* **1974**, *8*, 61-72.
(41) Berning, A.; Schweizer, M.; Werner, H.-J.; Knowles, P.J.; Palmieri, P. "Spin-orbit matrix elements for internally contracted multireference configuration interaction wavefunctions", *Mol. Phys.* **2000**, *98*, 1823-1833.
(42) Kramida, A., Ralchenko, Yu., Reader, J., and NIST ASD Team (2013). NIST Atomic Spectra Database (ver. 5.1), Available: http://physics.nist.gov/asd.
(43) Jensen, P. "Hamiltonians for the internal dynamics of triatomic molecules", *J. Chem. Soc., Faraday Trans. 2* **1988**, *84*, 1315-1340.
(44) Jensen, P. "A new Morse oscillator-rigid bender internal dynamics (MORBID) Hamiltonian for triatomic molecules", *J. Mol. Spectrosc.* **1988**, *128*, 478-501.
(45) Jensen, P.; Brumm, M.; Kraemer, W.P.; Bunker, P.R. "A treatment of the Renner effect using the MORBID Hamiltonian", *J. Mol. Spectrosc.* **1995**, *171*, 31-57.
(46) Jensen, P.; Odaka, T.E.; Kraemer, W.P.; Hirano, T.; Bunker, P.R. "The Renner effect in triatomic molecules with application to CH_2^+, MgNC and NH_2", *Spectrochim. Acta, Part A* **2002**, *58A*, 763-794.
(47) Hirano, T.; Bunker, P.R.; Patchkovskii, S.; Nagashima, U.; Jensen, P. "The Predicted Spectrum of FeOH in its Renner-Degenerate X^6A' and A^6A'' Electronic States", *J. Mol. Spectrosc.* **2009**, *256*, 45-52.
(48) Western, C.M., PGOPHER, A Program for Simulating Rotational Structure. 2007, University of Bristol: Bristol.
(49) Tackett, B.S.; Clouthier, D.J. "Observation of a new phosphorus-containing reactive intermediate: Electronic spectroscopy and excited-state dynamics of the HPBr free radical", *J. Chem. Phys.* **2005**, *123*, 144304/144301-144304/144314.
(50) Schlag, E.W., ZEKE Spectroscopy. 1998. 256 pp.

Chapter 4

Autodetachment Spectroscopy of the Aluminum Oxide Anion Dipole Bound State

The $^1\Sigma^+ \leftarrow X\ ^1\Sigma^+$ ground state to dipole bound state (DBS) electronic transition of AlO^- has been studied by means of autodetachment spectroscopy. Vibrational and rotational molecular constants for AlO^- have been determined for both the ground state (υ''=0,1) and the excited DBS (υ'=0,1). These data provide an improved determination of the electron affinity for AlO (2.6110(7) eV) that is consistent with an earlier measurement. The electron binding energy of the DBS was found to be 52±6 cm^{-1}. Experimental results are compared with the predictions from high level *ab initio* calculations.

4.1 Introduction

Studies of anions in the gas phase are relatively scarce compared to those of neutral species and positive ions. Of the existing studies, photodetachment spectroscopy has been the most common method for the characterization of anion ground states. Much of the geometric information (bond lengths and angles) extracted from these studies has been derived from Franck-Condon simulations of the vibrational band intensity envelopes. Higher resolution techniques, such as resonant two-photon photodetachment spectroscopy[1,2], could reveal the rotational structure needed for the determination of

geometric parameters for small anions. Unfortunately, the electronically excited states needed for these studies typically lie above the electron detachment threshold.

A solution that can be applied to some systems is near threshold autodetachment spectroscopy of excited dipole bound states (DBS)[3-24]. These states exist near the detachment threshold of an anion whose neutral counterpart has a dipole moment that is sufficient to bind the electron[25]. This excited electron can be described as being in a very diffuse orbital situated far from the molecular core, bound by the attraction to the positive end of the molecular dipole moment. DBSs of anions are analogous to Rydberg states of neutrals, where the Coulomb interaction of a Rydberg bound state is replaced with a dipole-electron interaction. Since the excited electron is believed to reside ~twenty to hundreds of Ångstroms from the molecular core, the dipole-electron interaction is expected to be very weak, ranging from a few to a couple of hundred wavenumbers in binding energy. The geometry of a DBS of an anion is expected to mimic that of the corresponding neutral molecule, just as molecules in Rydberg states adopt the geometry of the cation.

Extensive theoretical studies of DBSs have been conducted[17,25-29]. One of the points of interest has been the determination of the minimum dipole moment needed to support at least one DBS, often called the critical value. It was estimated that the minimum dipole moment needed to bind an electron to a non-rotating dipole moment is 1.625 D ([25] and references therein), giving rise to an infinite number of excited states within the stationary field. With the inclusion of the rotational operator $\widehat{H}_R = (\hbar^2/2I)\hat{J}^2$ the number of excited states becomes finite and the critical value increases to about 2 D.

Several examples of dipole bound states have been reported in past decades. Lineberger and co-workers were among the first to obtain rotationally resolved spectra for dipole bound states of several small molecules using autodetachment spectroscopy. The observed anions included FeO^- ($\mu \approx 3.2$ D)[3], CH_2CHO^-,[9,10,12] CH_2CN^- and CD_2CN^-,[6,11] H_2CCC^-,[8,13] and CH_2COF^-[7] (with μ = 3-5 D), amongst others.[4] More recent studies of DBSs include AuF^-,[5] $C_6H_5O^-$,[14] and the dehydrated uracil radial.[15]

In the present study we have investigated the AlO^- anion by characterizing the electronic transition between the ground state and an excited DBS. AlO^- was chosen because it has (1) a known electron affinity from photoelectron experiments[30,31], (2) a dipole moment[32,33] that is well above the critical value needed to support a DBS, and (3) a rotational constant B that is large enough to facilitate rotationally resolved measurements[34,35]. The first and only gas phase experimental studies of AlO^- were conducted using photodetachment spectroscopy in a magnetic bottle time-of-flight apparatus.[30,31] A detachment threshold of 2.60(1) eV and an anion vibrational frequency of 900(50) cm^{-1} were reported (1σ uncertainties are given in parentheses). Several computational studies of AlO^- have been published[26,36-39], providing estimates of the bond length, vibrational frequency and photodetachment threshold.

The characteristics of neutral AlO $X^2\Sigma^+$ are of importance for the present study as they predominantly define the properties of the AlO^- DBS. Calculations for neutral AlO(X) predict a dipole moment of approximately 4.4 D at the equilibrium distance[32,33]. Interestingly, these calculations indicate that the dipole moment is almost independent of the internuclear separation, at distances close to the equilibrium value. In formal terms, this effect was attributed to the evolution from $Al^{2+}O^{2-}$ to Al^+O^- as the bond distance

increases. There have been many gas phase spectroscopic studies of neutral AlO[40-46]. Recent work includes a high-resolution survey of the $B^2\Sigma^+$- $X^2\Sigma^+$ transition[34,35], and a millimeter wave study of the pure rotational transitions of the $X^2\Sigma^+$ υ=0, 1, and 2 levels[47].

In the experiments presented here, near threshold autodetachment spectroscopy of AlO^- was used to record rotationally resolved data for the DBS-$X^1\Sigma^+$ transition. Determination of the rotational constants for the υ=0 and 1 vibrational levels of both the anion ground state and DBS state was achieved through observation of the $0-0$ and $1-1$ sequence bands. These data also provided an accurate value for the electron affinity of AlO and the first vibrational interval of ground state AlO^-.

4.2 Experimental

Fig. 1 shows the main components of the apparatus used to generate AlO^- and record the photodetachment spectrum. AlO^- was produced through laser ablation of an aluminum rod (6061 Al, McMaster-Carr) in a Smalley style laser ablation source[48]. The frequency-doubled output of a Q-switched Nd:YAG laser (Minilite II, 532 nm, ~5-10 mJ) was focused onto the continuously rotating and translating Al rod. Helium seeded with 10% oxygen was pulsed through a supersonic valve (R.M. Jordan PSV C-211, 0.5 mm nozzle diameter, backing pressures of 4 – 20 psig), entraining the ablated material. The gas and ablated material was supersonically expanded into a vacuum chamber held at a working pressure of ~$1x10^{-5}$ Torr by a 5200 l/s diffusion pump.

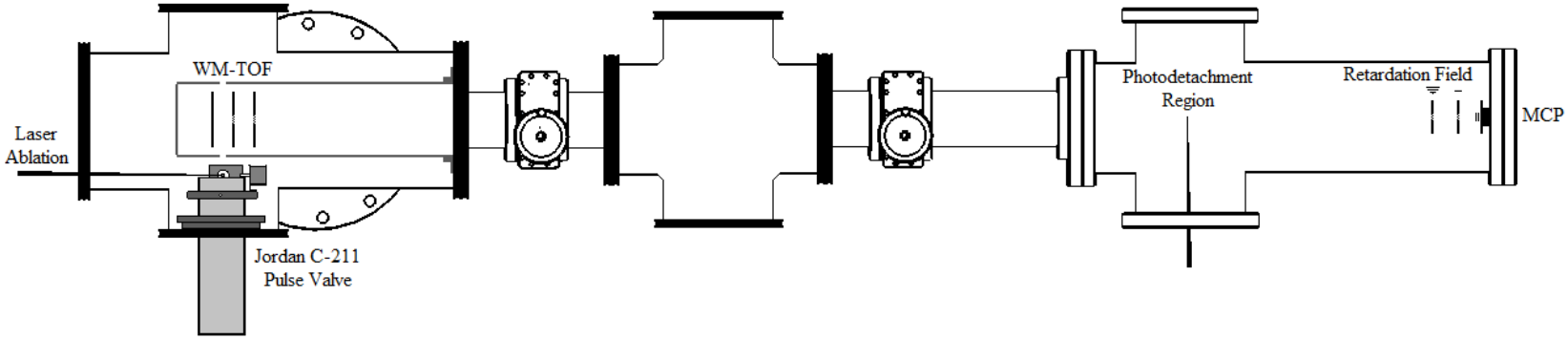

Figure 1. Schematic of the autodetachment spectrometer. WM-TOF: Wiley-McLaren Time of Flight, MCP: Microchannel Plates.

The core of the expansion entered a differentially pumped metal sleeve through a 6 mm diameter hole about 20 mm from the exit channel of the ablation source. This region, maintained at a working pressure of ~$1x10^{-6}$ Torr, housed a Wiley-McLaren time of flight mass spectrometer (WM-TOFMS) in a perpendicular orientation with respect to the direction of the expansion. Fast rising, negative pulsed voltages were applied to the repeller and extractor of the WM-TOFMS by high voltage switches (Directed Energy, Inc. PVX-4140), accelerating the anions into a drift region (working pressure $5x10^{-7}$ Torr) to allow for mass separation. The resolution of the mass spectrometer was $t/\Delta t$ = 690.

After mass selection, the anions entered a photodetachment region 1.9 meters from the repeller plate of the WM-TOFMS. The anions were intersected by the output of an excimer pumped dye laser (Lambda Physik Lextra 200 (308 nm) pumping a Lambda Physik FL3002 dye laser), operating at wavelengths expected to induce photodetachment of AlO^-. The pulsed laser was synchronized with the arrival of the AlO^- ions (see below) and propagated along an axis that was perpendicular to the molecular beam. Typical detachment laser pulse energies were in the range of 2 – 6 mJ, with a beam diameter of about 5 mm. Wavelength calibration of the laser was established using a commercial wavemeter (Bristol Instruments model 821). After photodetachment the resulting AlO and the undetached AlO^- continued their field free drift towards a microchannel plate detector (R.M. Jordan, 18mm Chevron stack), 0.58 m downstream. Just before detection, the neutral/anion packet traveled through a retardation zone consisting of a ground plate and negatively charged plate separated by 7.6 cm. This zone slowed the anions with respect to the neutrals, separating the two species. Both species were then detected and a

spectrum of detached anions verses laser frequency was recorded. Corrections for source fluctuations were made using the signals from the anions. All signals were captured by a digital oscilloscope (Agilent Technology DSO1024A) and integrated using a homemade LabVIEW 8.6 program. The experiments were conducted at a pulse repetition rate of 10 Hz. Note that the AlO^- ions were selectively photodetached by timing the laser pulses to coincide with the arrival of the AlO^- pulse. To set the timing, the time-of-flight spectrum was measured using the microchannel plate detector without applying the retardation field. The arrival time for AlO^- was then scaled by the distance ratio (5.8/7.7) to set the timing for the photodetachment pulse. As there were no other species with m/*e* ratios close to 43, this procedure yielded signals from AlO^- alone.

4.3 Experimental Results and Analysis

Photodetachment of AlO^- was studied within the energy range of 20830 – 21275 cm^{-1} (480 – 470 nm). The most informative region of this spectrum is shown in Fig. 2. This trace was taken with 128 shot averaging, 5-point smoothing, and at a wavelength step size of 0.001 nm (0.044 cm^{-1} at 476.5 nm), well below the linewidth of the laser (0.3 cm^{-1}). Fig. 2 was assembled from two separate scans taken on the same day under similar conditions. They are joined at 21017 cm^{-1}. Note that multiple additional spectra were recorded for this energy range, in runs that were spread over several weeks. The scan shown if Fig. 2 was chosen for presentation as the conditions yielded well-defined lines for both the 0-0 and 1-1 bands. The latter were sometimes weaker due to conditions that yielded lower temperatures. Spectra taken by scanning to energies lower than 20830 cm^{-1}

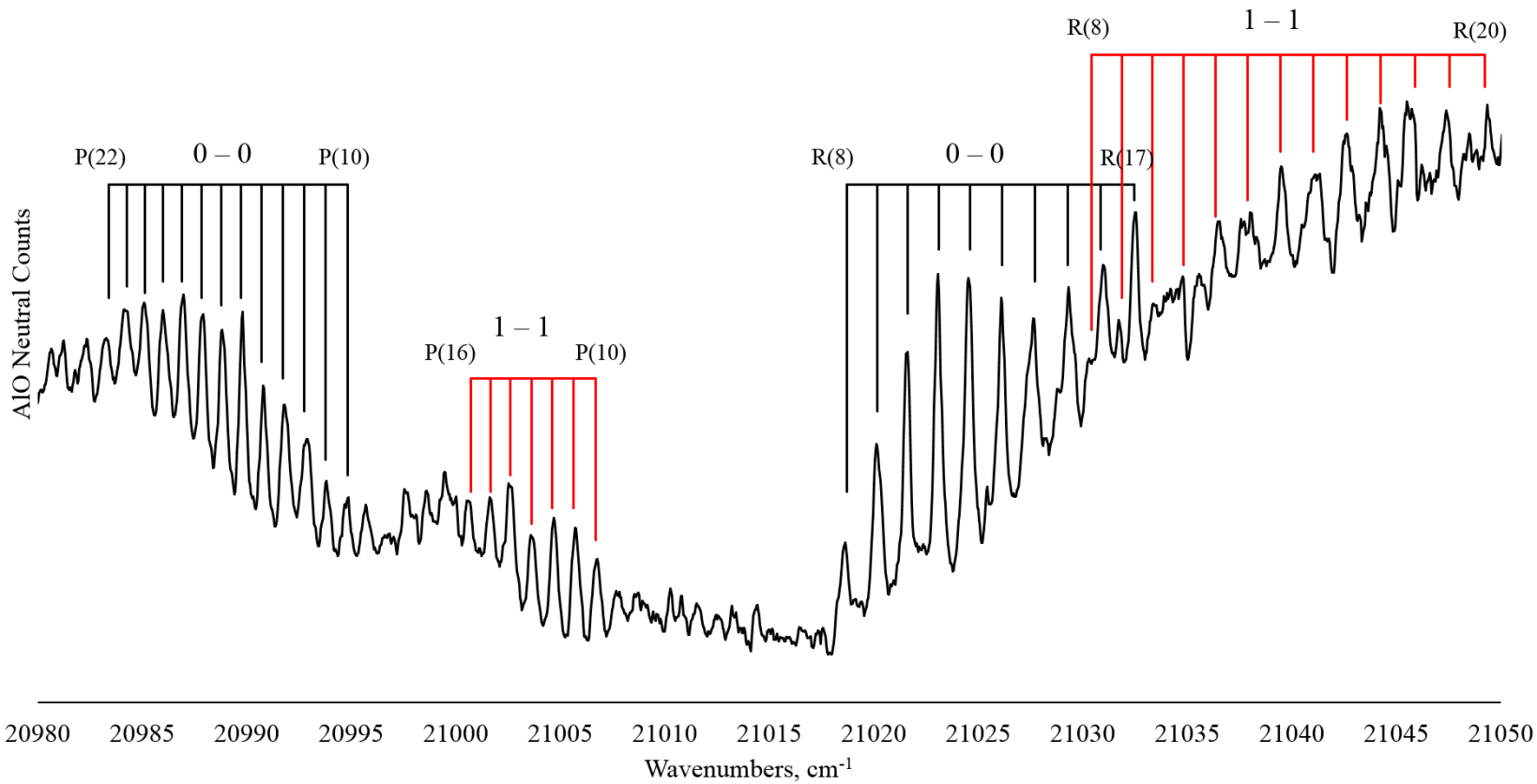

Figure 2. Autodetachment spectrum of AlO^-. Rotational line assignments are indicated by the vertical lines.

revealed no detachment signals, and scans to higher energies yielded signals that were too congested for unambiguous assignment.

Rotational line series consisting of two P- and two R-branches can be identified in Fig. 2. As discussed below, these branches originate from the $0-0$ fundamental band and the $1-1$ sequence band of the $^1\Sigma^+ \leftarrow X\ ^1\Sigma^+$ anion ground state to DBS electronic transition. An electron excited above the detachment threshold will undergo direct detachment to the neutral continuum. This process, which is always present, gives rise to the underlying baseline of the spectrum. Superimposed on this background is a significant increase in fast neutral production when a resonance between a bound state of the anion and a quasibound DBS level was encountered. The widths of these features were determined by the laser linewidth, indicating that the autodetachment rates were below $4x10^{10}$ s^{-1}. The intensities of the lines attributed to the $1-1$ band changed with source conditions, whereas the lines assigned to the 0-0 band remained relatively constant. This provided evidence that the former were part of a hot band. The relatively small energy spacing between the 0-0 and 1-1 features ruled out the possibility that the higher energy lines are from the 1-0 band.

The rotational line assignments indicated in Fig. 2 were established using combination differences. It was assumed that the rotational constants for the DBS would be closely similar to those of the corresponding vibrational levels of the neutral molecule. Note that the rotational branches in Fig. 2 lack transitions to upper state levels with a rotational quantum number (J') less than 9. We interpret this cut-off in the rotational structure of the 0-0 band to be an indication that $\upsilon'=0$, $J'=9$ is the first level of the DBS that is above the AlO(X) + e^- detachment threshold. Close inspection of Fig. 2 shows a

peak at 20995.6 cm^{-1} that could be assigned to P(9). However, the sharp onset of the R-branch at R(8) shows that the *J'*=8 level does not contribute to the spectrum. Hence, we assign the feature at 20995.6 cm^{-1} to the 1-1 band P(22) line. Molecular constants were derived from the autodetachment spectra by means of least squares fitting to the rotational line centers. The program PGOPHER[49] was used for this task. Alternative rotational line assignments were examined, using the criterion that the resulting upper state rotational constants should be suitably close to the values for AlO(X). These calculations confirmed that the numbering shown in Fig. 2 is unique. All parameters (lower and upper rotational *B* constants, and the band origins) were then fitted to the line positions, and the resulting constants are collected in Table 1.

The rotational temperature of the spectrum in Fig. 2 was in the range of 100-150 K. This is a rough estimate since the relative peak intensities were difficult to determine due to the underlying wavelength dependent direct detachment process. Additional uncertainties were contributed by fluctuations of source conditions.

4.4 Electronic Structure Calculations

Single-point energies have been calculated at internuclear separations between 1.3-3Å at the CASSCF/MRCI+Q level[50-54] for the electronic ground states of both AlO^- and AlO. It has been shown that an active space including the 3*s*,3*p* and 2*s*,2*p* orbitals of Al and O, respectively, is insufficient to reliably calculate the potential energy curve (PEC) of the $X^2\Sigma^+$ state of AlO[32]. Including an additional set of *s* and *p* orbitals in the active space allows for better description of the changing electronic structure of AlO over

Table 1. Molecular constants and term energies for the DBS $^1\Sigma \leftarrow X\ ^1\Sigma$ AlO^- transition. All values are in wavenumbers (cm^{-1}). EA = electron affinity, eBE = DBS electron binding energy.

$v' - v''$	DBS $^1\Sigma \leftarrow X\ ^1\Sigma$ AlO^-		$X\ ^2\Sigma$ AlO
$0-0$	T_{00}	21006.5(2)	
	B_0''	0.627(2)	
	B_0'	0.637(2)	$B_0 = 0.63849184$[a]
$1-1$	T_{11}	21018.2(2)	
	B_1''	0.624(2)	
	B_1'	0.635(2)	$B_1 = 0.632691(04)$[a]

	$X\ ^1\Sigma$ AlO^-	DBS $^1\Sigma$	$X\ ^2\Sigma$ AlO
$\Delta G_{1/2}$	953.7(5)	965.4[b]	965.455[a]
eBE		52(6)	
EA	-	-	21059(6)

[a] Valves taken from Ref. 26 [b] Based on the assumption that the vibrational intervals of AlO and the DBS of AlO^- are the same.

the full range of internuclear separations. We utilized an active space in the CASSCF procedure in which all valence electrons of both AlO and AlO^- were distributed among twelve orbitals, viz. CASSCF(10,12) for AlO^-. Core orbitals were constrained to be doubly occupied, but were optimized in the CASSCF procedure. Standard aug-cc-pVXZ (X = Q, 5) basis sets (denoted aVXZ herein) for both Al and O were used, to which a second set of augmented functions were incorporated in order to better describe the diffuse nature of the AlO^- frontier orbitals. The exponents of the added basis functions were determined using an even-tempered expansion of the two lowest exponent functions of the aVXZ basis sets, which yielded,

Al

aVQZ: *s*, 0.006670; *p*, 0.003670; *d*, 0.003469; *f*, 0.021995;*g*, 0.065571.

aV5Z: *s*, 0.006706; *p*, 0.003584; *d*, 0.010290; *f*, 0.019929; *g*, 0.045348; *h*, 0.115536.

O

aVQZ: *s*,0.023429; *p*,0.016343; *d*,0.053414; *f*,0.122207; *g*,0.276163.

aV5Z: *s*,0.023457; *p*,0.015480; *d*,0.048341; *f*,0.093459; *g*,0.224802; *h*,0.452167.

The resulting basis sets are referred to as d-aVXZ. Total interaction energies have been extrapolated to estimate the complete basis set limit using the two-point formula of Halkier et al.[55] We refer to this extrapolated basis set limit as d-aV(Q,5)Z. All calculations were performed using MOLPRO 2010.1[56]. The bound ro-vibrational levels of the resulting PECs were calculated using the LEVEL 8.0 program[57]. The lowest vibrational levels were least squares fit to the standard Morse energy level expression, yielding effective values of ω_e and $\omega_e x_e$. Predictions for the electron affinity were made with the inclusion of the zero point vibrational energies. The results for the ground states of AlO and AlO^- are collected in Table 2, where it can be seen that the agreement

between the observed and calculated properties of AlO was respectable. Fig. 3 shows the AlO ground state potential energy curve and dipole moment, taken from the d-aV(Q,5)Z calculations. Expectation values for the dipole moment ($\langle\mu\rangle_v = \langle v|\mu|v\rangle$) of $\langle\mu\rangle_0$=4.8171 and $\langle\mu\rangle_1$=4.8173 D were obtained using Level 8.0[57].

The EOM-CCSD method was used to calculate the energy of the DBS of AlO^-, at the fixed internuclear distance of 1.618 Å (the experimentally derived R_e of AlO). The electron binding energy (eBE) was determined from the difference between this total energy, and that of AlO calculated at the same internuclear separation at the CCSD level. Further sets of diffuse functions were added to the aVTZ basis sets, the exponents of which were determined from an even-tempered expansion of the lowest two exponent functions of the previous basis set. Table 3 lists the eBE values for basis sets increasing in size from aVTZ to 7-aVTZ (where the initial number specifies the number of diffuse functions). Note that five sets of diffuse functions were required to obtain a positive binding energy, and that the calculations appeared to be converged with the addition of seven functions.

4.5 Discussion

The first question to address concerns the nature of the excited state of AlO^- observed in these experiments. We have assigned this as the DBS based on the energy of the state, the rotational selection rules, and the agreement with the rotational constants of AlO. Gutsev et al.[26] did predict a $^3\Pi$ valence excited state of AlO^- that is bound, relative to AlO + e^-, by about 600 cm^{-1}. The rotational and vibrational constants predicted for this state (B_e=0.618, ω_e= 978) were not consistent with the experimental data (c.f. Table 1).

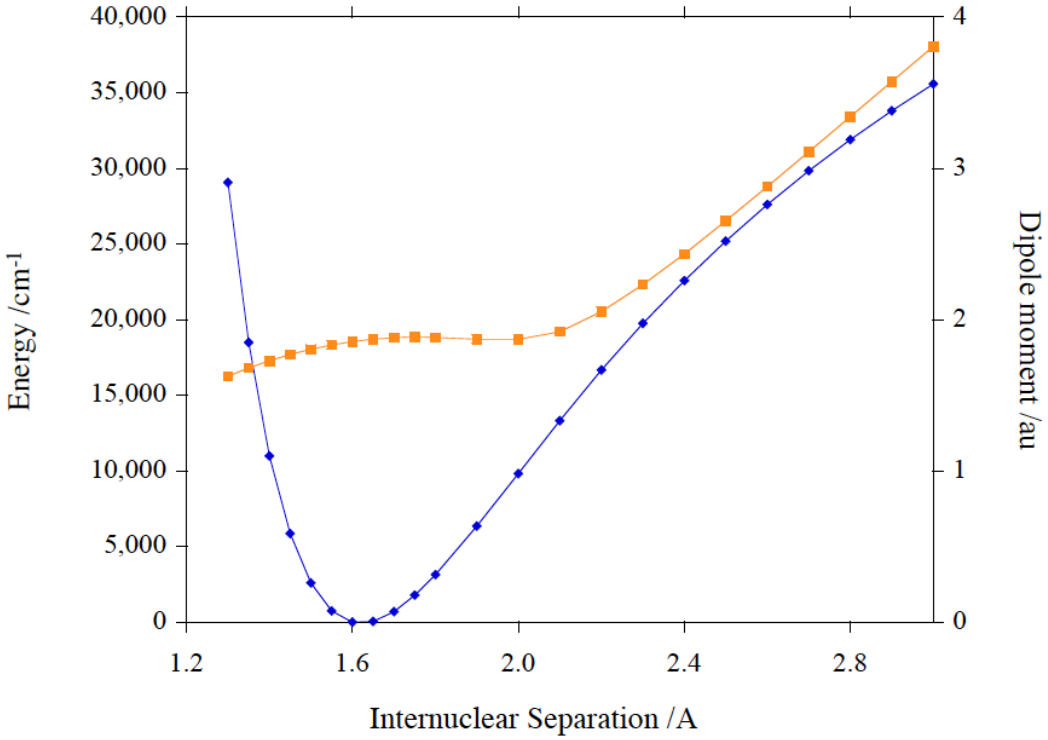

Figure 3. Potential Energy Curve of AlO(X) (blue diamonds) and the molecular dipole moment (orange squares) of AlO(X) as a function of internuclear separation.

Table 2. Spectroscopic constants calculated at the CASSCF+MRCI+Q level of theory. All values are in units of cm^{-1}, except R_e which is in units of Angstrom.

	R_e	B_0	B_1	ω_e	$\omega_e x_e$	$\Delta G_{1/2}$	EA
			$X^2\Sigma$ AlO				
d-aVQZ	1.632	0.627	0.621	963.2	7.49	948.2	20854
d-aV5Z	1.626	0.632	0.626	971.9	7.53	956.8	20897
d-aV(Q,5)Z	1.620	0.637	0.631	981.0	7.55	965.9	20939
Expt. [a]	1.6179	0.6387	0.6328	979.525	7.036	965.45	20970(80)
			$X^1\Sigma$ AlO^-				
d-aVQZ	1.654	0.611	0.606	952.0	5.16	941.7	
d-aV5Z	1.649	0.615	0.610	957.6	5.18	947.2	
d-aV(Q,5)Z	1.644	0.619	0.614	963.5	5.21	953.0	

[a.] The experimental values are from ref. [34], with the exception of the EA which is from ref. [31]

Table 3. Calculated electron binding energies for the DBS of AlO^-

Basis Set	eBE / cm^{-1}
aVTZ	-6249.1
d-aVTZ	-1311.8
t-aVTZ	-241.7
q-aVTZ	-0.2
5-aVTZ	48.7
6-aVTZ	56.5
7-aVTZ	56.3

Conversely, the simple P- and R- branch structure of the spectrum is consistent with a $^1\Sigma^+$ - $^1\Sigma^+$ transition. Hence, we are confident that the DBS was observed.

In order to observe an autodetachment event, the final state of the transition must lie above the detachment threshold. Once excited, the state will decay either through autodetachment or radiative relaxation, but the former usually dominates. In general, an anion can autodetach via vibrational relaxation, with a $\Delta v = -1$ propensity, or rotational relaxation. These processes are manifestations of a breakdown in the Born-Oppenheimer approximation, where the DBSs couple with the continuum through vibrational-electronic and rotational-electronic coupling, respectively.[3,6,7,9,10,12,58] For the $0 - 0$ band, there cannot be a loss in vibrational energy since the υ'=0 level of the DBS autodetaches to $v = 0$ of AlO. Therefore, the DBS υ'=0 level must undergo rotational-electronic autodetachment.

As mentioned above, the 0-0 band rotational branches in Fig. 2 are incomplete, with the final levels *J'*=0-8 being unobserved. The most straightforward interpretation of this observation is that these levels are below the detachment threshold. This situation is illustrated in Fig. 4. If *J'*=9 is the first level above the threshold, the AlO(X) υ=0 product would be produced in rotational levels with $N \leq 3$, where *N* is the angular momentum exclusive of spin (if *N*=4 was open for *J'*=9, the *J'*=8 level could autodetach to *N*=0 and 1). It is likely that the rate for autodetachment increases with a decrease in the change in the molecular angular momentum required. However, the present experiments were not sensitive to this rate provided that it significantly exceeded the radiative decay rate. The abrupt onset of the R-branch evident in Fig. 2 is consistent with a detection process that is predominantly governed by the energetic threshold. Bracketing of the threshold between

the *J'*=8 and 9 levels yields a detachment energy of 21059(6) cm^{-1} (2.6110(7) eV), in good agreement with the results of Desai et al.[31] (2.60(1) eV). The bracketing also provides a value of 52(6) cm^{-1} for the binding energy of the electron in the DBS. The eBE predicted by our theoretical calculations is excellent agreement with this result (to a degree that is probably fortuitous).

Autodetachment is an energetically accessible channel for all rotational levels of the AlO^- DBS with $\upsilon'=1$. Despite this fact, the rotational structure of the 1-1 band showed the same onset for the R-branch at R(8), as was observed for the 0-0 band. This indicates that rotational autodetachment dominates over the vibrationally mediated process for this vibrational level. Note that the calculated dipole moments for AlO(X) in the υ=0 and 1 states (given above) are almost the same. As the electron binding energy in the DBS is determined by the dipole moment, it is entirely reasonable that the rotational autodetachment process would show approximately the same rotational energy threshold (within the bracketing) for υ'=0 and 1. The low probability for vibrational autodetachment may also be related to the weak dependence of the dipole moment on the bond length near the equilibrium separation.

As described in the Introduction, it is expected that the molecular constants of the DBS will be very close to those of the neutral molecule. In keeping with this expectation, we find that the DBS rotational constants obtained from the spectral fitting are the same as the constants for AlO(X), to within the experimental error limits. Hence, it is reasonable to assume that the first vibrational interval ($\Delta G_{1/2}$) for the DBS will be very close to that of AlO(X) (965.455 cm^{-1}). With this approximation, the interval between the 0-0 and 1-1 band origins of Fig. 2 yields a vibrational interval for the ground state of

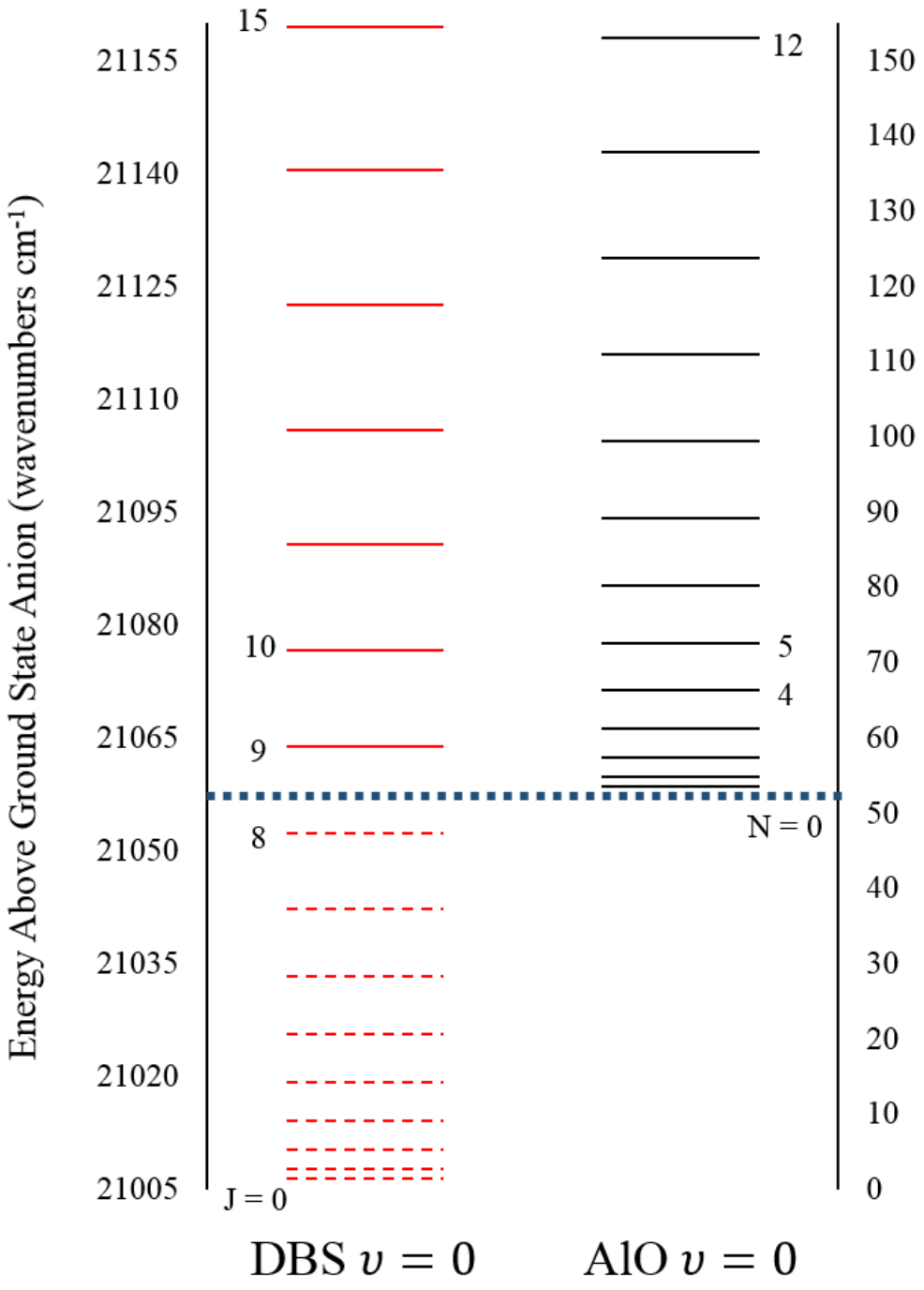

Figure 4. Energy level diagram comparing $\nu_{DBS} = 0$ to $\nu_{AlO} = 0$. The dotted blue line represents the DBS binding energy (right axis) and the detachment threshold of AlO^- (left axis).

AlO^- of $\Delta G_{1/2}$=953.7(5) cm^{-1} (c.f. Table 1). This result is consistent with the value of 900(50) cm^{-1} reported by Desai et al.[31]

The energy for dissociation of AlO^- into the products Al + O^-, $D_0(AlO^-)$, may be determined using the relationship:

$$D_0(AlO^-)=EA(AlO)+D_0(AlO)-EA(O)$$

where D_0(AlO) is the experimentally derived dissociation energy of the neutral ground state of AlO of 5.27(2) eV[59], EA(O) is the electron affinity of O, 1.4611 eV[60], and EA(AlO) is the electron affinity of AlO determined in this study (2.6110(7) eV). Such an analysis results in a value of 6.42(2) eV for D_0 of AlO^-, which is considerably larger than that of the neutral AlO species.

Table 4 presents a comparison of the results from electronic structure calculations for AlO^- with the molecular constants derived from the autodetachment spectrum. Overall, the theoretical predictions are in reasonably good agreement with experiment. The calculations all produced equilibrium bond lengths that were slightly too long. The value of $\Delta G_{1/2}$ of 953.7(5) cm^{-1} is in good agreement with MRCI/d-aV(Q5)Z value of 953.0 cm^{-1} calculated in this work. However, in order to compare with the vibrational frequencies determined in other work, it is helpful to derive an estimate for ω_e based on the experimental data. For this purpose we use the equation, derived from the Morse approximation, $\Delta G_{1/2}=\omega_e-\omega_e^2/2D_e$ where D_e is the dissociation energy. Using the experimental value for $\Delta G_{1/2}$ and the value of D_e=6.42 eV yields an estimate for ω_e of 963 cm^{-1}. The theoretically calculated values are again in respectably good agreement. The D_0 calculated in this work (6.420 eV) is identical to the CCSD(T) value of Gutsev *et*

Table 4. Calculated and measured constants for AlO^-

	D_0 / eV	ω_e/cm^{-1}	EA[a]/eV	Ref.
1.645		945.2	3.08	[37]
1.675		-	2.92	[36]
1.64		975	2.44	[39]
1.643	6.42	969	2.652	[26]
1.644	6.420	963.5	2.596	Present work
1.636(3)[b]	6.42(2)	963[c]	2.6110(7)	Exp.

[a.] Electron affinity
[b.] R_0 value derived from B_0'
[c.] Calculated from the measured $\Delta G_{1/2}$ value. See text for details.

al., and in excellent agreement with the value of 6.42(2) eV derived from our experimental electron affinity. Lastly, the EA is the most challenging property for electronic structure calculations. In Table 4 it can be seen that the CCSD(T) calculations of Gutsev et al.[26] and the present d-aV(Q,5)Z calculations were the most successful in predicting the EA.

4.6 Conclusion

The electronic transition between the ground state and the dipole bound excited state of AlO^- has been characterized using autodetachment spectroscopy. Rotationally resolved data for the 0-0 and 1-1 bands provided molecular constants for the upper and lower states. Observed rotational thresholds for autodetachment yielded an accurate value for the electron affinity of AlO (2.6110(7) eV) and the electron binding energy of the dipole bound state (52±6 cm^{-1}). Comparisons to these results show that high-level theoretical calculations for this prototypical anion are reasonably reliable. The dissociation energy, D_0 of the AlO anion has been derived to be 6.42(2) eV, which is higher than that of the corresponding neutral species. This study establishes benchmark data that can be used to further evaluate theoretical models for anions.

4.7 Acknowledgement

We are grateful to Prof. D. Neumark (University of California, Berkeley) for his generous advice concerning the construction and testing of our anion spectrometer. This work was supported by the National Science Foundation under grant CHE-1265586.

4.8 References to Chapter 4

1. W. C. Lineberger and T. A. Patterson, Chem. Phys. Lett. 13, 40 (1972).
2. H.-T. Liu, D.-L. Huang, Y. Liu, L.-F. Cheung, P. D. Dau, C.-G. Ning, and L.-S. Wang, Journal of Physical Chemistry Letters 6, 637 (2015).
3. T. Andersen, K. R. Lykke, D. M. Neumark, and W. C. Lineberger, Journal of Chemical Physics 86, 1858 (1987).
4. E. A. Brinkman, S. Berger, J. Marks, and J. I. Brauman, Journal of Chemical Physics 99, 7586 (1993).
5. D. B. Dao and R. Mabbs, Journal of Chemical Physics 141, 7 (2014).
6. K. R. Lykke, D. M. Neumark, T. Andersen, V. J. Trapa, and W. C. Lineberger, Journal of Chemical Physics 87, 6842 (1987).
7. J. Marks, J. I. Brauman, R. D. Mead, K. R. Lykke, and W. C. Lineberger, Journal of Chemical Physics 88, 6785 (1988).
8. K. Yokoyama, G. W. Leach, J. B. Kim, and W. C. Lineberger, Journal of Chemical Physics 105, 10696 (1996).
9. R. D. Mead, K. R. Lykke, W. C. Lineberger, J. Marks, and J. I. Brauman, Journal of Chemical Physics 81, 4883 (1984).
10. A. S. Mullin, K. K. Murray, C. P. Schulz, and W. C. Lineberger, Journal of Physical Chemistry 97, 10281 (1993).
11. D. M. Wetzel and J. I. Brauman, Journal of Chemical Physics 90, 68 (1989).
12. A. S. Mullin, K. K. Murray, C. P. Schulz, D. M. Szaflarski, and W. C. Lineberger, Chemical Physics 166, 207 (1992).
13. K. Yokoyama, G. W. Leach, J. B. Kim, W. C. Lineberger, A. I. Boldyrev, and M. Gutowski, Journal of Chemical Physics 105, 10706 (1996).
14. H. T. Liu, C. G. Ning, D. L. Huang, P. D. Dau, and L. S. Wang, Angewandte Chemie-International Edition 52, 8976 (2013).
15. H. T. Liu, C. G. Ning, D. L. Huang, and L. S. Wang, Angewandte Chemie-International Edition 53, 2464 (2014).
16. J. E. Turner, American Journal of Physics 45, 758 (1977).
17. W. R. Garrett, Chemical Physics Letters 62, 325 (1979).
18. J. H. Hendricks, S. A. Lyapustina, H. L. de Clercq, J. T. Snodgrass, and K. H. Bowen, J. Chem. Phys. 104, 7788 (1996).
19. N. I. Hammer, R. J. Hinde, R. N. Compton, K. Diri, K. D. Jordan, D. Radisic, S. T. Stokes, and K. H. Bowen, J. Chem. Phys. 120, 685 (2004).
20. S. Xu, W. Zheng, D. Radisic, and K. H. Bowen, Jr., J. Chem. Phys. 122, 091103/1 (2005).
21. C. Desfrancois, H. Abdoul-Carime, and J.-P. Schermann, International Journal of Modern Physics B 10, 1339 (1996).
22. C. Desfrancois and J. P. Schermann, Chemical Society Reviews 31, 269 (2002).
23. C. E. H. Dessent, J. Kim, and M. A. Johnson, Accounts of Chemical Research 31, 527 (1998).
24. C. L. Adams, H. Schneider, K. M. Ervin, and J. M. Weber, J. Chem. Phys. 130, 074307/1 (2009).
25. K. D. Jordan and F. Wang, Annual Review of Physical Chemistry 54, 367 (2003).

26. G. L. Gutsev, P. Jena, and R. J. Bartlett, Journal of Chemical Physics 110, 2928 (1999).
27. K. D. Jordan, Accounts of Chemical Research 12, 36 (1979).
28. M. Sindelka, V. Spirko, P. Jungwirth, F. Wang, S. Mahalakshmi, and K. D. Jordan, J. Chem. Phys. 121, 1824 (2004).
29. J. Simons, Annual Review of Physical Chemistry 62, 107 (2011).
30. S. R. Desai, H. B. Wu, C. M. Rohlfing, and L. S. Wang, Journal of Chemical Physics 106, 1309 (1997).
31. S. R. Desai, H. B. Wu, and L. S. Wang, International Journal of Mass Spectrometry and Ion Processes 159, 75 (1996).
32. B. H. Lengsfield, III and B. Liu, J. Chem. Phys. 77, 6083 (1982).
33. N. Honjou, Journal of Molecular Structure: THEOCHEM 939, 59 (2010).
34. O. Launila and L. E. Berg, J. Mol. Spectrosc. 265, 10 (2011).
35. M. D. Saksena, M. N. Deo, K. Sunanda, S. H. Behere, and C. T. Londhe, Journal of Molecular Spectroscopy 247, 47 (2008).
36. J. V. Ortiz, Chem. Phys. Lett. 296, 494 (1998).
37. K. A. Peterson and R. C. Woods, J. Chem. Phys. 90, 7239 (1989).
38. K. A. Peterson and R. C. Woods, J. Chem. Phys. 92, 6061 (1990).
39. C. Zenouda, P. Blottiau, G. Chambaud, and P. Rosmus, Journal of Molecular Structure: THEOCHEM 458, 61 (1999).
40. C. Yamada, E. A. Cohen, M. Fujitake, and E. Hirota, Journal of Chemical Physics 92, 2146 (1990).
41. M. Goto, S. Takano, S. Yamamoto, H. Ito, and S. Saito, Chemical Physics Letters 227, 287 (1994).
42. T. Torring and R. Herrmann, Molecular Physics 68, 1379 (1989).
43. H. Ito and M. Goto, Chemical Physics Letters 227, 293 (1994).
44. A. Bernard and R. Gravina, Zeitschrift Fur Naturforschung Section a-a Journal of Physical Sciences 39, 1049 (1984).
45. O. Launila and J. Jonsson, Journal of Molecular Spectroscopy 168, 1 (1994).
46. A. T. Patrascu, C. Hill, J. Tennyson, and S. N. Yurchenko, Journal of Chemical Physics 141 (2014).
47. O. Launila and D. P. K. Banerjee, Astronomy and Astrophysics 508, 1067 (2009).
48. M. A. Duncan, Review of Scientific Instruments 83, 041101/1 (2012).
49. C. M. Western, PGOPHER version 8.0 (University of Bristol Research Data Repository, 2014).
50. H. J. Werner and P. J. Knowles, J. Chem. Phys. 82, 5053 (1985).
51. P. J. Knowles and H. J. Werner, Chem. Phys. Lett. 115, 259 (1985).
52. P. J. Knowles and H. J. Werner, Chem. Phys. Lett. 145, 514 (1988).
53. H. J. Werner and P. J. Knowles, J. Chem. Phys. 89, 5803 (1988).
54. E. R. Davidson and D. W. Silver, Chem. Phys. Lett. 53, 403 (1977).
55. A. Halkier, T. Helgaker, P. Jorgensen, W. Klopper, H. Koch, J. Olsen, and A. K. Wilson, Chem. Phys. Lett. 286, 243 (1998).
56. H.-J. Werner.
57. R. J. LeRoy, LEVEL 8.0.
58. K. R. Lykke, R. D. Mead, and W. C. Lineberger, Physical Review Letters 52, 2221 (1984).

59. L. Pasternack and P. J. Dagdigian, J. Chem. Phys. 67, 3854 (1977).
60. C. Blondel, C. Delsart, C. Valli, S. Yiou, M. R. Godefroid, and S. Van Eck, Physical Review A: Atomic, Molecular, and Optical Physics 64, 052504/1 (2001).

Chapter 5

Photoelectron Velocity-Map Imaging of the Beryllium Oxide Anion, BeO^-

The $X\ ^1\Sigma^+$-$X\ ^2\Sigma^+$ anion ground state to neutral ground state electronic transition of BeO^- has been studied by means of photoelectron velocity-map imaging spectroscopy in a newly constructed apparatus. The $\Delta G_{1/2}$ vibrational interval and the electron detachment threshold of BeO^- were determined for the first time. Experimental results are compared to high level *ab initio* calculations. Details of the spectrometer and its performance are also reported.

5.1 Introduction

As mentioned in the introduction to this chapter in Chapter 1, the evolution of bonding within molecular metal clusters and metal – oxide clusters as they grow in size is of great interest.[1-7] Fundamental questions regarding clusters are: how do their properties develop as a function of cluster size, and at what size do clusters exhibit the properties of bulk metal? There is no one property that can be measured that will identify the exact cluster size that can be defined as being a bulk sample. Instead, molecular identities such as ionization energy, bond energies, geometric structure, and the energy gap between the

highest occupied molecular orbital (HOMO) and the lowest unoccupied molecular orbital (LUMO) are all used to interpret cluster to bulk evolutions.

Be_nO_m clusters have been seen as a promising target for researchers to answer these principle questions since they are both intriguing theoretically and experimentally. Beryllium contains only four electrons making it suitable for high level *ab initio* calculations, while the light masses of beryllium and oxygen make the smaller clusters candidates for rotationally resolved spectroscopies, allowing for geometric analysis.

The smallest beryllium oxide cluster unit, the diatomic BeO, has been investigated for the past several decades, both experimentally[8,9] and theoretically.[10-24] Since this molecule is a diatomic, obtaining the desired information above is relatively trivial with established spectroscopic techniques. However, as described in Chapter 1, as a cluster size grows by either the addition of Be or O atoms, complications can arise making the spectroscopy and/or analysis of results difficult. It was also proposed in Chapter 1 that probing the ground state of a beryllium oxide neutral cluster via photoelectron velocity-map imaging spectroscopy on its anionic form would provide valuable insight in understanding the transition from cluster to bulk material. There is little data on any of the small Be_nO_m clusters ($n, m > 1$), [25-28] and no experimental data for the anions. Therefore, the present work focuses on the smallest beryllium oxide anion cluster unit, BeO^-.

Though BeO has been well-studied, the anion has received far less attention and only from a theoretical point of view.[16,18,29-31] Previous studies of BeO^- have predicted a $^2\Sigma^+$ ground state symmetry, and a vertical electron detachment energy between 2.1 – 2.2

eV. The additional electron is proposed to reside mostly on the positively charged Be atom, in the predominately non-bonding 2s orbital.

Presented here are the previously unmeasured electron affinity of BeO and the $\Delta G_{1/2}$ vibrational interval of BeO^- obtained by photoelectron velocity-map imaging spectroscopy. These results are also compared with the predictions of new high level *ab initio* calculations, revealing great agreement between the theoretical and experimental data. Additionally, details of the spectrometer and its performance are discussed, along with a description of the photoelectron velocity-map imaging technique.

5.2 Experimental Procedure and Photoelectron Velocity-Map Imaging Spectroscopy

The data presented here were measured using photoelectron velocity-map imaging spectroscopy. The details of the technique have been described extensively in other publications[32-34] and will be briefly elaborated on here, while describing the experimental procedure. Detailed descriptions of individual components of the spectrometer were presented earlier in Chapter 1.

The imaging apparatus used in this study was modified from an existing setup described elsewhere[35] (also see Chapter 1, and Chapter 4). Figure 1 shows a diagram of the apparatus used to study BeO^-. BeO^- was produced in a laser ablation source[36] that was coupled to a pulse valve. The helium carrier gas was seeded with 5% N_2O at backing pressures of 18 – 34 psia. The anions produced in the ablation process supersonically expanded into a differentially pumped vacuum chamber where a Wiley-McLaren time of flight mass spectrometer (WM-TOFMS),[37] in a perpendicular orientation with respect to

the direction of the expansion, was housed. Fast rising, negative pulsed voltages were applied to the repeller and extractor of the WM-TOFMS by high voltage switches, accelerating the anions into a drift region to allow for mass separation before reaching the photodetachment region of the velocity-map imaging optics. The resolution of the mass spectrometer was $t/\Delta t = 690$. Along the flightpath of the anions from the WM-TOFMS, an Einzel lens and four sets of deflector plates were used to focus and guide the anions into the velocity-map imaging (VMI) optics. Additionally, a fifth set of deflector plates could be pulsed to act as a mass gate to only allow the anion of interest to enter the detachment region.

Once inside the VMI optics, the mass selected anions were intersected by the polarized, focused output of a Nd:YAG pumped dye laser (Continuum 7010 (532 nm) pumping a Quanta Ray PDL-2 dye laser), operating at a photon energy above the detachment threshold of the species of interest. Typical detachment laser pulse energies were in the range of 1 – 2 mJ, with a beam diameter of < 2 mm. Wavelength calibration of the laser was established using the gas phase absorption spectrum of the B – X transition of room temperature I_2.

The photoelectrons produced within the lens were accelerated down a 66 cm long drift region, shielded from external electric and magnetic fields by layers of mu-metal, to the detector (PHOTONIS USA, INC. 75mm Chevron stacked microchannel plates (MCP) with a fiberoptic phosphor screen with P47 phosphor). Electrons impacting the detector were recorded with a CCD camera (Physimetrics UI-2230SE-M-GL, 1024x768). These electrons were discriminatively detected from all other charged particles by pulsing the voltage (gain) on the MCPs only when the electrons arrived at the detector. Individual

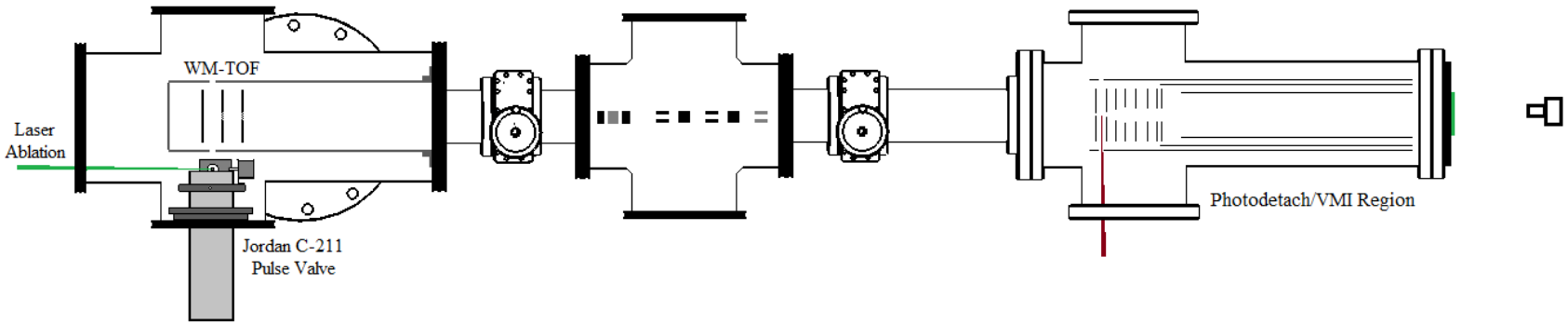

Figure 1: Schematic of photoelectron velocity-map imaging spectrometer. Figure drawn to scale. WM-TOF: Wiley-McLaren Time of Flight, VMI: Velocity-Map Imaging

cycles of the experiment were recorded and summed over several tens of thousands of cycles to produce an image. The final image was saved using the imaging collection software developed by Suits.[38] Transformation of the image from velocity space to energy was done using the Polar Onion Peeling (POP)[39] and Maximum Entropy Velocity Legendre Reconstruction (MEVELER) techniques.[40] The illumination of the screen from electron or anion impacts could also be monitored with a photomultiplier tube positioned off axis from the camera. This form of detection produced the TOF-MS spectrum, and was extremely useful in the optimization of anion and photoelectron production. The repetition rate of the experiment was 10 Hz. All images were calibrated using the known transitions from detachment of the sulfur anion, S^-.[41-43]

The VMI optics used in this study were modeled after those used by León and Wang[33]. VMI optics act as an electrostatic lens that accelerate the photoelectrons produced within the interaction region towards a position sensitive detector, in such a way that a sharp image is formed. The electrons are created in an initial distribution (object) set by the volume of the intersection of the photodetachment laser and the anion packet. This process is called velocity-map imaging.[34] Velocity-map imaging has the capability of mapping charged particles with the same velocity vector onto the same position some distance away, accounting for spatial distributions of their initial starting position. This feature is only true if the charged particles are observed at the focal plane of the VMI optics (lens). The focusing properties of the VMI optics can be adjusted by varying the voltage ratios of the electrostatic plates that make it up. This adjustability is very convenient since it is much harder to move the detector (observer).

Velocity-map imaging also allows for the separation of charged particles of different kinetic energy while maintaining the particles' angular distributions. Placing a position sensitive detector in the path of the accelerated particles at the focal plane of the VMI optics makes it possible to detect both the particles' kinetic energies and their angular distributions. Measurement of their kinetic energies directly determines the energy levels of the anion and neutral species. The electron angular distribution encodes orbital symmetries and molecular dynamics. These measurements can be made for any photo-process involving one or more charged particles,[34,44,45] but only situations involving electrons are addressed in this thesis.

When multiple detachment channels of a species are accessible with a given photon energy, all electron kinetic energies released can be detected simultaneously if the acceleration from the VMI optics is adequate. While the focusing properties of the VMI optics can be changed (tuned) by altering the potential differences between the individual electrodes of the electrostatic optic, the total kinetic energy given to the electrons in the direction of the detector is governed by the net voltage across the entirely of the VMI optic. Given the fixed distance from the detachment region to the detector (the drift region), varying the degree of acceleration to the photoelectrons varies their flight time before detection. This property allows for tunability of the resolution of the VMI and the dynamic range of the spectrometer with respect to electron kinetic energy (eKE). The total energy given to the photoelectrons can be described by the standard equation of motion $v=\sqrt{\frac{2E}{m}}$.

The tunability of the VMI optics is utilized in many situations. If two or more detachment channels are close in energy the overall voltage of the VMI optics can be lowered to provide less acceleration to the photoelectrons towards the detector. This will create a longer flight time for the electrons, allowing for a greater spatial separation of the slightly differing eKEs, and in turn allow for the detachment channels to be resolved. Alternatively, a higher voltage can be applied to the VMI optics, greatly accelerating the photoelectrons. This voltage increase will, of course, have the opposite effect and shorten the flight time of the photoelectrons. Though a loss in resolution will be had for small differences in eKEs, a relatively large energy range of eKEs can be detected simultaneously, giving an overview of the level structure of a species.

5.3 Electronic Structure Calculations

Electronic structure calculations were performed by Dr. Adrian M. Gardner on both the anion and neutral beryllium oxide molecules. This was done to assist in the assignment of the spectra, and to aid in the understanding of the mechanisms of beryllium bonding. For both beryllium and oxygen, the aug-cc-pwCVXZ (X = T, Q, 5) basis sets were employed, denoted awCVXZ herein. A second set of diffuse functions was added to these basis sets in order to better describe the diffuse nature of the BeO^- frontier orbitals. The exponents of the diffuse functions were determined from an even-tempered expansion of the two lowest exponent functions of the awCVXZ basis sets. The resulting basis sets are denoted d-awCVXZ in the following.

All calculations were performed with the MOLPRO suite of programs.[46] Potential energy curves (PECs) were calculated, pointwise, by means of the partially spin adapted coupled cluster method including single and double excitations and perturbative corrections for triple excitations (RCCSD(T)), and the complete active space self-consistent field followed by multireference configuration interaction (CASSCF+MRCI+Q) levels of theory. These PECs are shown in Figure 2. In the RCCSD(T) calculations, all electrons were included in the correlation treatment. The active space in the CASSCF calculations consisted of the 2*s* and 2*p* orbitals of both Be and O, while the "core" orbitals, which are linear combinations of the 1*s* atoms orbitals, were constrained to be doubly occupied. Their wavefunctions were optimized in the CASSCF procedure in order to aid convergence. For both the anion and neutral BeO species, all electrons were included in the correlation treatment in the subsequent MRCID calculation in an attempt to recover the core-valence correlation energy. The Davidson correction was applied in order to partially correct for the size inconsistency of the MRCI calculations. Total RCCSD(T) and MR-CISD interaction energies have been extrapolated to estimate the complete basis set limit using the two point formula of Halkier *et al*.[47] (referred to as d-aV(Q,5)Z). The bound ro-vibrational levels of the resulting PECs were calculated using the LEVEL 8.0 program.[48] The lowest vibrational levels were least squares fit to the standard Morse energy level expression, yielding effective values of ω_e and $\omega_e x_e$. Predictions for the electron affinity were made with the inclusion of the zero point vibrational energies.

Initially, the restricted Hartree – Fock RCCSD(T) (RHF-RCCSD(T)) calculations were attempted for the expected $^2\Sigma^+$ ground state of BeO^-. Although the T_1 diagnostic, a

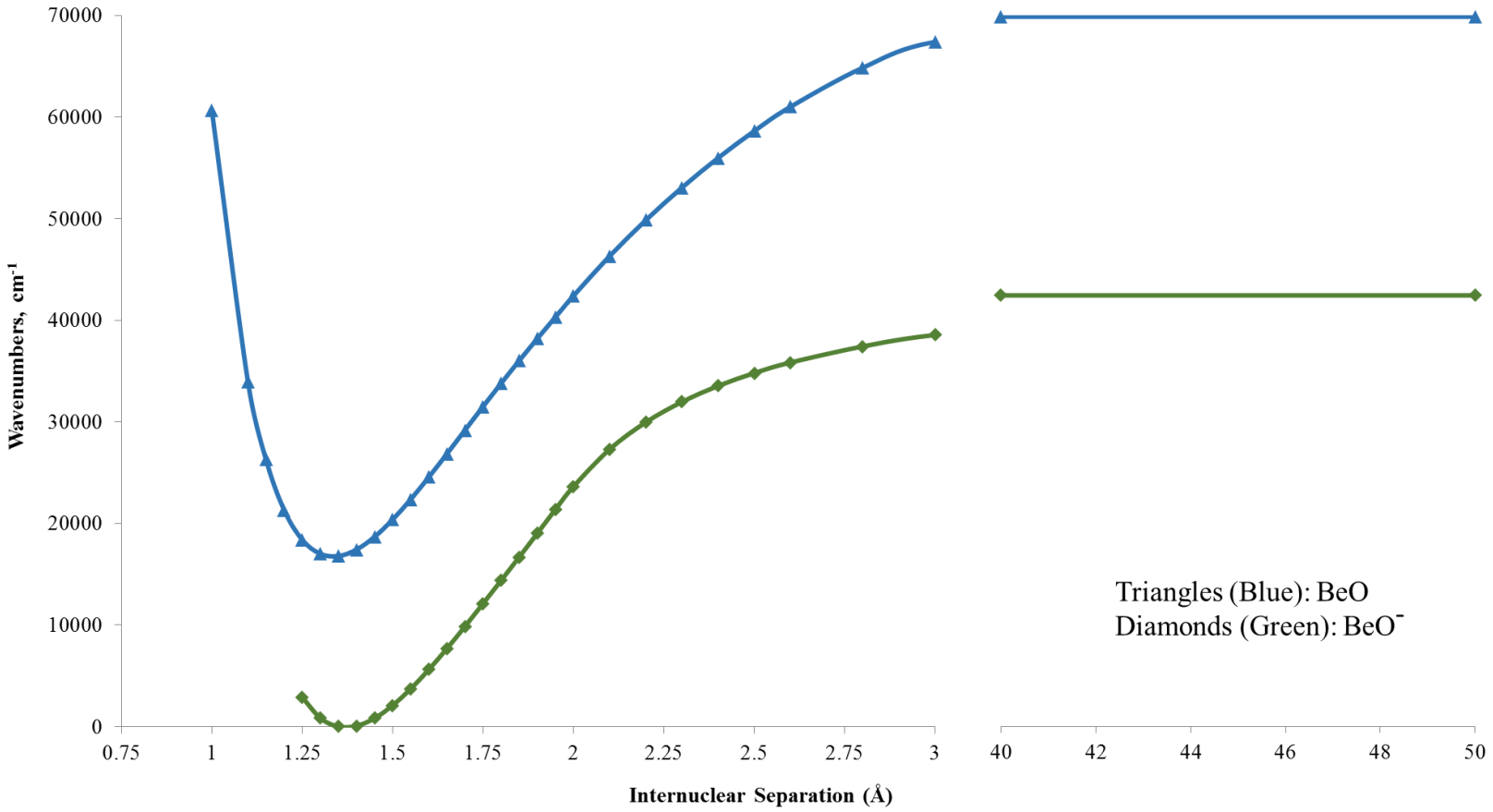

Figure 2: Potential energy curves of the grounds states of BeO^- and BeO. See text for details.

commonly employed test of the degree of multi-reference character of the electronic wavefunction, has values of ~0.022 at internuclear separations in the vicinity of the expected equilibrium bond length of the anion (1.3-1.5 Å), it rises to ~0.04 at an internuclear separation of 1.8 Å. Additionally, convergence of the RHF wavefunction become unstable at longer bond lengths. Values of the T_1 diagnostic lying above 0.044 suggests distinct multi-reference character. Note that CCSD calculations using a spin unrestricted reference wavefunction are not supported by MOLPRO. The T_1 diagnostic examines amplitudes of single excitation in the RCCSD procedure, based on a given self-consistent field (SCF) wavefunction. Large values of the T_1 diagnostic may therefore be obtained when the reference wavefunction is a poor description of the electronic state of interest, and therefore large amplitude single electron excitations are apparent in the more representative RCCSD wavefunction. As a result, initial wavefunctions obtained from a B3LYP (Becke, three-parameter, Lee-Yang-Parr exchange-correlation functional) calculation were used in subsequent RCCSD and RCCSD(T) calculations. These calculations displayed well behaved convergence at internuclear separations of 1-50 Å, with values for the T_1 diagnostic below 0.04 being obtained at internuclear separation between 1.0 – 5 Å, which raised at longer separations. This is referred to as B3LYP-RCCSD(T) later in the discussion section.

5.4 Calibration with Sulfur Anion, S^-

When analyzing an image, the binding energies of the states of interest are determined using

$$E_{Binding} = h\nu - EA - eKE \qquad \text{(Eq. 1)}$$

where EA is the electron affinity of the species, eKE is the electron kinetic energy of the photoelectrons, and hν is the energy of the detachment photon. In order to determine eKE, the VMI optics must be calibrated. The only way one can convert from pixels on an image to eKE at a particular voltage setting (focusing conditions) on the VMI optics is through a calibration. This calibration is done by recording images of a species with known electron detachment transitions. Each transition from the known species will provide one calibration value of eKE. Taking multiple images at different photon energies, but the same VMI voltages, will yield additional calibration points since the eKEs will differ, as seen from Eq. 1.

The data for BeO^- shown later were calibrated using the known transitions from photodetachment of the sulfur atomic anion, S^-.[41-43] Figure 3 shows the raw image of S^- photodetached at a photon energy of 17537 cm^{-1} (570.22 nm). There are six accessible transitions at this photon energy arising from the two spin-orbit states of the anion ground state detaching to the three spin-orbit states of the neutral ground state: $^3P_{2,1,0} \leftarrow {}^2P_{3/2,\ 1/2}$. These six detachment channels can be seen as the six rings in Figure 3, and in the photodetachment spectrum in Figure 4 generated from the deconvolution of the image in Figure 3 using the POP algorithm. Images from S^- photodetachment were taken at two additional photon energies, 16949 and 17100 cm^{-1} (not shown), in order to increase the dynamic range of the calibration over the majority of the screen pixels.

It should be noted that a measurement of the overall energy resolution of the spectrometer was determined to be in the range of $\frac{\Delta eKE}{eKE} = 5$ - 10% based on the spectrum in Figure 4. Here, ΔeKE is the full width half maximum of the transitions at a given

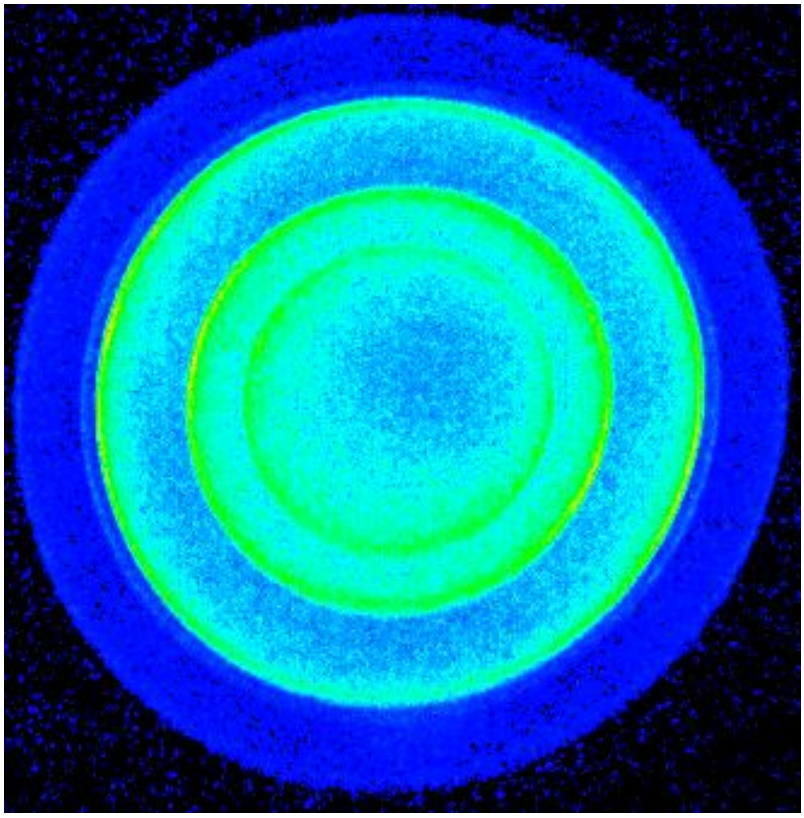

Figure 3: Raw image of S^- photodetached at a photon energy of 17537 cm^{-1} (570.22 nm) (Color). Intensity of electron signal increases from blue to red.

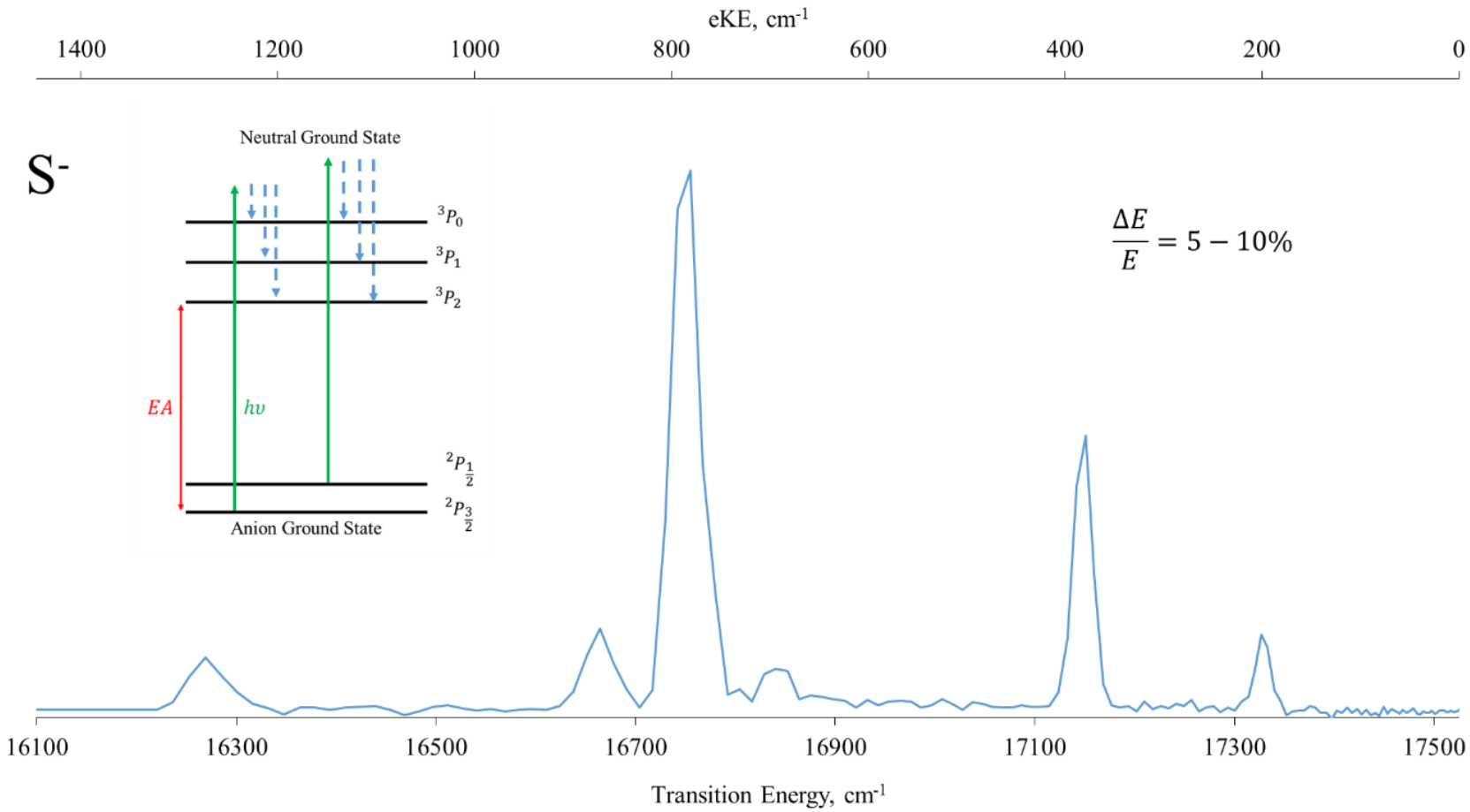

Figure 4: Photodetachment spectrum of S^- at a photon energy of 17537 cm^{-1} (570.22 nm). Transition Energy is given by hν – eKE. Inset: General energy level diagram for the photodetachment of ground state S^- to ground state S (not drawn to scale).

eKE. This form of resolution is used since all the electrons have an initial velocity distribution (Δv) within the anion packet. Since Δv is constant throughout an image, all rings in an image will have the same the width in pixels (Δr). The radius of a ring of an image in pixels (r) scale in energy as

$$E = cr^2 \qquad \text{Eq. (3)}$$

where c is a proportionality constant related to the conditions of the VMI optics. Therefore, as r increases r (increasing eKE), ΔeKE will also increase. A range is given in Figure 4 based on the error in measuring ΔeKE due is a limited number of points per peak. This range equates to about 20 cm^{-1} resolution for the lowest eKE electrons detected with S^-.

5.5 Results and Discussion

Shown in Figure 5 is the raw image from photodetachment of BeO^- taken at 18200 cm^{-1} photon energy. Figure 6 is the photoelectron spectrum resulting from the transformation using the MEVELER algorithm on the image in Figure 5. In order to achieve the best photoelectron spectrum from the image, only the top half (designated by the horizontal white line) was used in the transformation process due to the quality of this image being degraded for several reasons, which will be discussed in detail in a later section.

Two broad features are present in Figure 6. The feature at 17510 cm^{-1} is identified as the $(\nu' - \nu'')$ 0 – 0 origin band. This value, taken at the peak of the feature, places the vertical electron affinity of BeO at 17510 ± 25 cm^{-1} (2.17096 ± 0.0031 eV). The electron affinity is in remarkable agreement with theoretical calculations done in this

study, under predicting by only 23 cm^{-1} for B3LYP-RCCSD(T) as can be seen in Table 1. Previous theoretical predictions from Jordan *et al.*[30] and Gutsev *et al.*[31] are also in great agreement at 17340 cm^{-1} (2.162 eV) and 17437 cm^{-1} (2.15 eV), respectively. The values from the present theoretical and experimental work are listed in Table 1, along with all the spectroscopic parameter from the current study.

It can be seen that the band at 17510 cm^{-1} has a sharp onsets at lower energy and then decrease towards higher energy. These features are due to two factors. First, since there is population in the $v'' = 1$ vibrational level, and possibly $v'' = 2$, the 1 – 1 and 2 – 2 sequence bands can occur with sufficient detachment photon energy. The detachment photon used to acquire the spectrum in Figure 6 was 700 cm^{-1} above the detachment threshold. This energy is much greater than the separation of the sequence band transitions (~80 cm^{-1}), 0 – 0 being the lowest energy transition. Therefore, it is believed that these bands are unresolved. Second, simulated rotational transition profiles to the spectrum in Figure 6 (not shown) were conducted using calculated rotational constants from the present study for the first three vibrational levels of the anion ground state (not reported) and the experimentally determined rotational constants for the first three vibrational levels of the neutral ground state.[31] It was estimated from this simulation that the rotational temperature of BeO^- was on the order of 300K. This rotational temperature would undoubtably broaden the spectrum since the resolution of the apparatus is much poorer than two times the rotational constant of BeO (~3.2 cm^{-1}).

The feature located 1400 cm^{-1} lower in energy is labeled as the 0 – 1 hot band and determines the $\Delta G_{1/2}$ vibrational interval of BeO^- ($\Delta G_{1/2}^-$) as 1400 ± 25 cm^{-1}. Franck-Condon simulations shown in Figure 7 support this assignment, where $\Delta v = 0$ direct

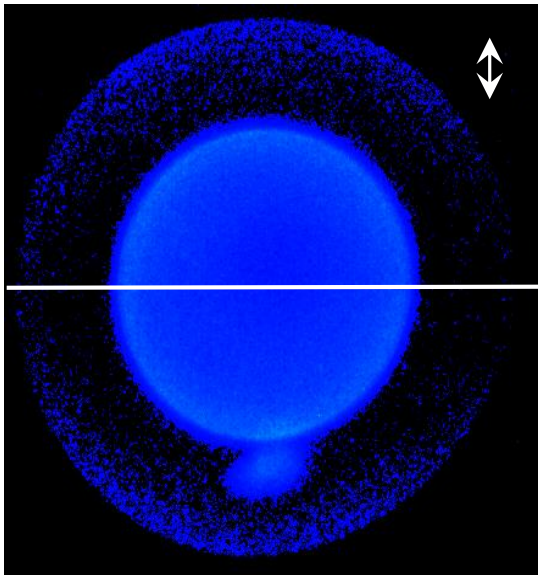

Figure 5: Raw photoelectron velocity-map image of BeO^- taken at 18200 cm^{-1}. Double arrow line indicates the direction of polarization of detachment laser. Horizontal line indicates the dividing line used in analysis (See text). Inner ring spawns from the origin band and 1 – 1 sequence band transitions. Outer ring spawns from hot band transitions.

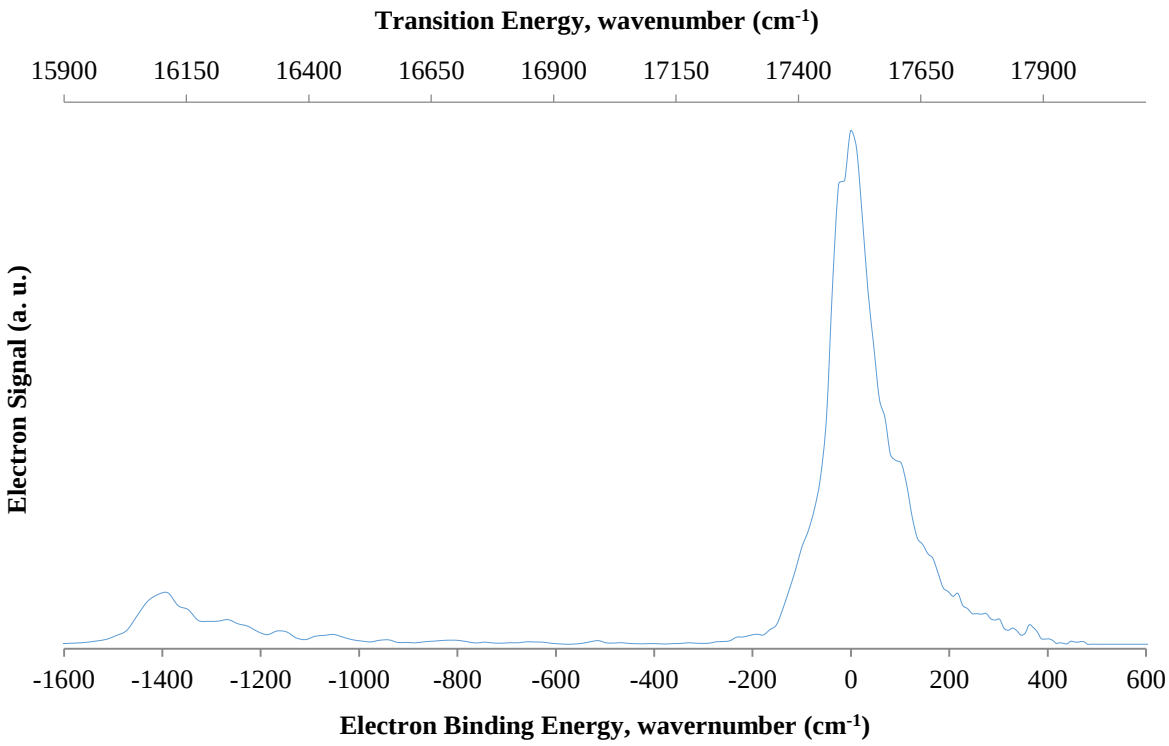

Figure 6: Photoelectron spectrum of BeO^- at 18200 cm^{-1} photon energy. Transition Energy given as hν – eKE.

Table 1: Experimental and theoretical spectroscopic parameters determined in this study. All values are in units of wavenumbers (cm^{-1}) expect R_e which is given in Angstroms.

BeO^-					
	R_e	$\Delta G_{1/2}$	ω_e	$\omega_e x_e$	eBE
Exp.		1400			17510
RHF-RCCSD(T)	1.364	1377.6	1397.4	9.9	
B3LYP-RCCSD(T)	1.364	1374.7	1394.2	9.7	17487
MRCI	1.364	1375.8	1397.6	10.9	17236

BeO					
	R_e	$\Delta G_{1/2}$	ω_e	$\omega_e x_e$	EA
Exp.	1.331		1487.32	11.83	17510
B3LYP-CCSD(T)	1.330	1471.1	1493.5	11.2	17487
MRCI	1.329	1479.4	1502.7	11.6	17236

electron detachment from the anion ground state to the neutral ground state has by far the greatest Franck-Condon overlap. The values for $\Delta G^{-}_{1/2}$ obtained from the MRCI and RCCSD(T) calculations were in agreement, but they were ~30 cm^{-1} below the experimental value. This difference falls close to the lower limit of the estimated error of the experimental data of ± 25 cm^{-1}. Therefore, it is difficult to determine the magnitude of the discrepancy in the calculations. This band has a similar profile as the band at 17510 cm^{-1}. With the inclusion of the 1 – 2 hot band transition, the unresolved structure is attributed to rotational broadening and the overall resolution of the spectrometer.

The $\Delta G_{1/2}$ vibrational interval of BeO ground state is 1510.91 cm^{-1}.[8] This value is over 100 cm^{-1} greater than $\Delta G^{-}_{1/2}$. The lower vibrational interval of the anion ground state suggest a weakening in the beryllium – oxygen bond with the addition of the extra electron. Calculations show a lengthening of the equilibrium bond length from R_e = 1.330Å for BeO to R_e = 1.364Å for BeO^- (Table 1**)**, also suggesting that the orbital occupied by the unpaired electron of the anion has some anti-bonding character. The anti-bonding character coincides with the predicted anti-bonding character of the LUMO σ^*molecular orbital obtained from molecular orbital theory. However, since the orbital is largely Be 2s in character, residing on the positively charged beryllium atom, the electron density gained on Be will most likely lower the charge polarity of the bond, causing it to lengthen to accommodate the new charge balance. A lower harmonic vibrational frequency for the anion was also predicted in past studies.[29,31]

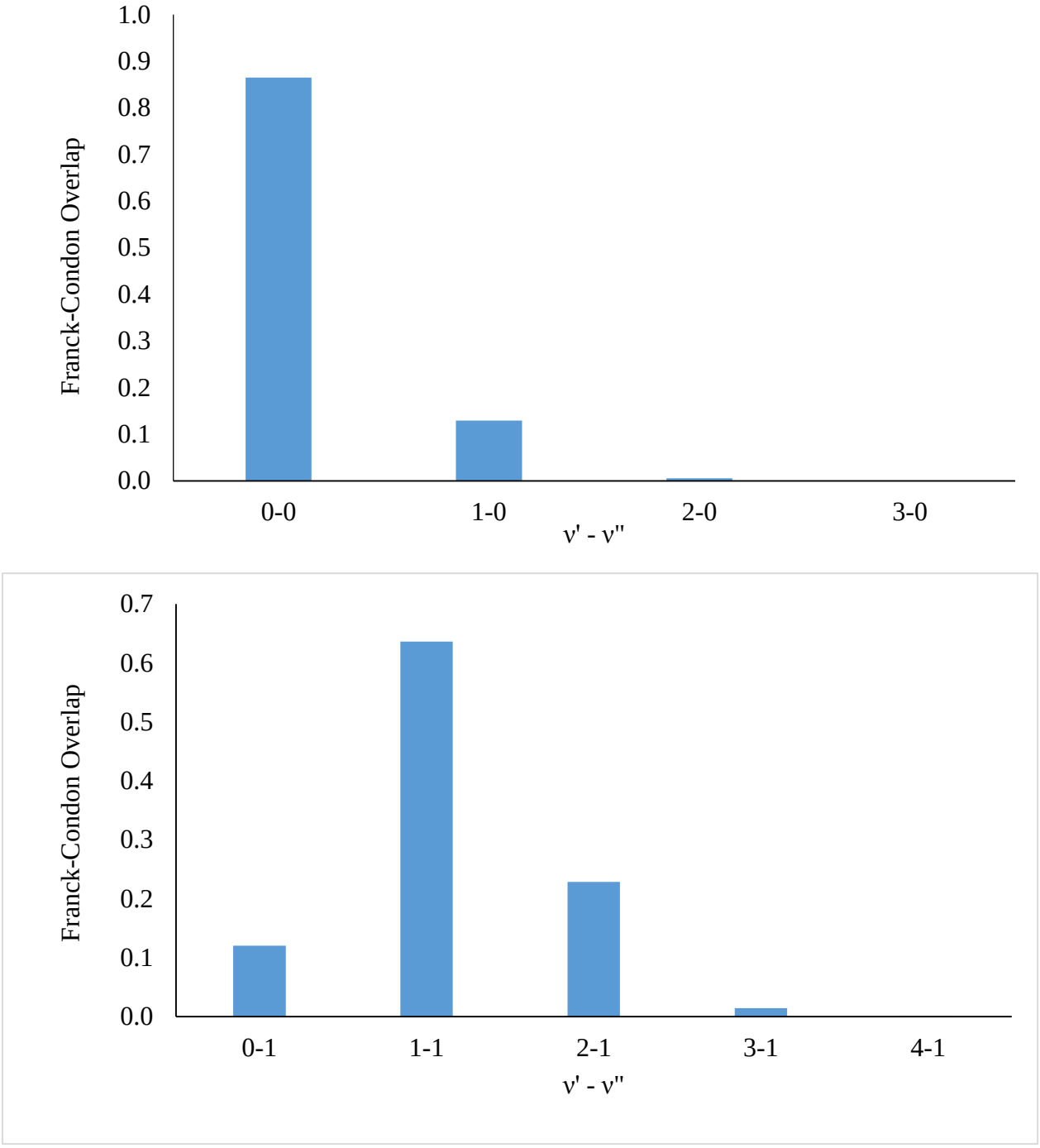

Figure 7: Franck-Condon simulation of direct electron detachment of ν" = 0 ground state BeO^- (Top) to ground state BeO, and ν" = 1 ground state BeO^- (Bottom) to ground state BeO.

It should be noted that the spectroscopic parameters determined at the RHF-RCCSD(T) and B3LYP-RCCSD(T) levels were in excellent agreement with one another, confirming that despite the differing reference wavefunctions/densities employed, the final electronic structure reached in the RCCSD(T) calculation were very similar.

In order to determine the symmetries of the initial and final states involved in a photodetachment process, the photoelectron angular distribution (PAD) can be examined. The PAD is the measurement of electron signal as a function of θ, the azimuthal angle between the polarization of the detachment photon and the velocity vector of the ejected electron. For single-photon detachment,[49] the PAD is given by

$$I(\theta)=\frac{\sigma}{4\pi}(1+\beta P_2(\cos\theta)) \qquad \text{(Eq. 2)}$$

where σ is the total photodetachment cross section, $P_2(\cos\theta)$ is the second Legendre polynomial, and β is the anisotropy parameter having values between -1 and 2. Calculating β by fitting Eq. 2 to a photoelectron velocity-map image will determine the angular anisotropy of the detached electrons at a given eKE. This information will, in turn, allow the identification of either the initial or final state symmetry through direct product of their irreducible representations within the molecular point group, assuming only one of the state's symmetry is known.

Identifying the state symmetries of the ground states of BeO and BeO^- is quite trivial and can be done *a priori* of the experiment. The ground state of the closed shelled neutral has been experimentally verified to be $^1\Sigma^+$.[24] There is no experimental work on the anion, but different levels of theory have concluded that the anion ground state symmetry[16,18,29-31] is $^2\Sigma^+$. Therefore, since the electronic state symmetries are already

known, and the uncertainty of the assignment of the transitions seen is low, the PAD for this experiment will mostly be an indication of the quality of the image.

Figure 8 shows the relationship between the anisotropy parameter and electron kinetic energy for the X $^1\Sigma^+$-X $^2\Sigma^+$ transition of BeO^-. β can be seen to oscillate between 0 and 0.5 spaced about 110 cm^{-1} apart around the origin band. The spacings are in decent agreement with the spacings of the 0 – 0, 1 – 1, and possibly the 2 – 2 sequence bands, given the uncertainty in peak positions due to the low resolution. However, based on both ground state symmetries being Σ, one would expect a β value very close to 2, signifying an electron angular momentum of $l = 1$. A value of $l = 1$ would arise from an s-type electron being detached, meaning it resides in an s(σ) atomic(molecular) orbital. Likewise, the electron must gain one unit of angular momentum from the incident photon since the neutral BeO does not gain this unit of momentum, on the grounds that the molecular symmetry stays as Σ ($\Delta\Lambda = 0$). β for the hot band transition peaks at 1.5, closer to the predicted value of 2. In order to explain the discrepancies between the measured and expected values of β the quality of the image must be analyzed.

5.6 Image Quality and its Effects on Spectrometer Resolution

There are a few features to be discussed about the image in Figure 5. First is the intense spot towards the bottom of the image. This spot is due to anions that have detached during their flight from the source that happen to impact the detector at the same time that the photoelectrons arrive. These neutrals are usually not a problem since the detector's "on" time is so short (tens of nanoseconds), but it is sometimes a difficult situation to avoid (the solution being to blindly alter source conditions). Furthermore,

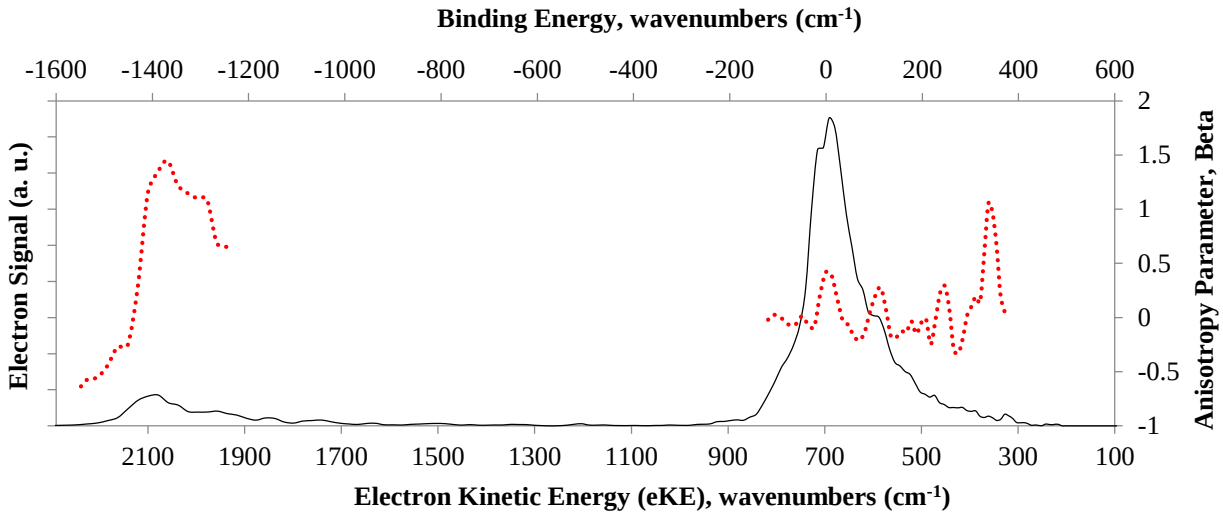

Figure 8: Comparison of the anisotropy parameter, β (dotted red), and the photoelectron spectrum of BeO^- (solid black).

this problem only becomes apparent after an image has been accumulating for several thousand cycles. This spot will greatly affect the quality of the transformation from velocity space to energy since it overlaps the signal of interest. Only the top half of the image was used to eliminate the effects of the neutral signal. This elimination could be done with little consequence, so long as each quadrant of an image is identical upon a combination of a simple rotation about the center of the image and a vertical or horizontal reflection. This requirement is true in most cases. The negative effects of not using the entire image to reproduce the spectrum is a considerable loss in signal to noise, since one is literally removing signal.

As mentioned above, the quality of an image greatly affects the value of β calculated. There are two critical reasons the image in Figure 5 would produce inaccurate β values. The first is that the raw image is rotated counterclockwise about the center with respect to the polarization of the detachment laser. Recall that the PAD is a measurement of the angle of ejection of the electrons with respect to the polarization vector of the incident photon. The polarization vector is assumed by the POP and MEVELER algorithms to be along the double-headed arrow in Figure 5. If the true polarization of the laser deviates from this position in the plane of the detector surface (image) it will rotate the image about the center axis orthogonal to the plane of the image, as it is in Figure 5. When quadrate symmetrizing during transformation of the image, any rotation in the image will result in "extending" the intensity of the ring about its circumference. This gives a value for β closer to 0, resembling an isotropic intensity distribution. Rotation of the image does not affect β for transitions that are truly isotropic.

The second reason for the potential inaccurate β measurements is the instrument distortion of the image. The image is visibly non-circular, most notably in the bottom right quadrant. It is not entirely clear what effect(s) are contributing to the deformation of the electron distribution, but it is believed that the most probable cause is due to the construction of the VMI optics. The electric fields within the optics must be as close to symmetrical about the center axis as possible. Any defects will break the symmetry and map electrons with the same velocity vectors to different radii. Much trial and error has led to the conclusion that at least four factors could be the source of this problem. The surface quality and flatness of the individual plates is very important in maintaining a uniform electric field between each plate. Another factor is the degree of parallelism of each plate with respect to every other plate. If all of the plates are not parallel to each other, the electric field between them will be asymmetric. Lastly, the VMI optics must be parallel to the detector. The electron spheres created within the VMI optics must impact the detector head on. If there is any drift from the center axis of the experiment, the image will become elliptical. Eliminating these problems is an ongoing effort. Regardless of these faults, the image in Figure 5 is the highest quality image taken of BeO^- on this spectrometer to date.

5.7 Conclusion

The $X\ ^1\Sigma^+$-$X\ ^2\Sigma^+$ electronic transition of BeO^- was studied by means of photoelectron velocity-map imaging spectroscopy in a newly constructed apparatus. The $\Delta G_{1/2}$ vibrational interval of BeO^- and the electron affinity of BeO were determined for the first time. Experimental and theoretical results were compared and agreed very well.

Details of the spectrometer and its performance were discussed and possible reasons for the underperformance were outlined.

Efforts to improve the circularity of the images, thus greatly increasing the resolution of the spectrometer, are ongoing. The spectroscopy of BeO^- will be revisited in the future upon the improvement of the spectrometer's performance. This improvement will diminish the error bars on the values reported, by up to an order of magnitude. Accurate values of β will also be able to be measured.

Photoelectron velocity – map imaging will also be applied to study the unexplored low lying a $^3\Pi$ state of BeO. This state is optically forbidden from the BeO ground state (a $^3\Pi \leftarrow X\ ^1\Sigma^+$) based on electron spin selection rules. Detachment from the anion ground state, however, is spin allowed (a $^3\Pi \leftarrow X\ ^2\Sigma^+$).

5.8 References to Chapter 5

(1) Wang, L. M.; Wang, L. S. Probing the electronic properties and structural evolution of anionic gold clusters in the gas phase. *Nanoscale* **2012**, *4*, 4038-4053.

(2) Jena, P.; Castleman, A. W. Clusters: A bridge across the disciplines of physics and chemistry. *Proceedings of the National Academy of Sciences of the United States of America* **2006**, *103*, 10560-10569.

(3) Thomas, O. C.; Zheng, W. J.; Xu, S. J.; Bowen, K. H. Onset of metallic behavior in magnesium clusters. *Physical Review Letters* **2002**, *89*, 4.

(4) Heaven, M. C.; Merritt, J. M.; Bondybey, V. E.: Bonding in Beryllium Clusters. In *Annual Review of Physical Chemistry, Vol 62*; Leone, S. R., Cremer, P. S., Groves, J. T., Johnson, M. A., Eds.; Annual Review of Physical Chemistry; Annual Reviews: Palo Alto, 2011; Vol. 62; pp 375-393.

(5) Hakkinen, H.; Moseler, M.; Landman, U. Bonding in Cu, Ag, and Au clusters: Relativistic effects, trends, and surprises. *Physical Review Letters* **2002**, *89*, 4.

(6) Raghavachari, K.; Logovinsky, V. STRUCTURE AND BONDING IN SMALL SILICON CLUSTERS. *Physical Review Letters* **1985**, *55*, 2853-2856.

(7) Morse, M. D. CLUSTERS OF TRANSITION-METAL ATOMS. *Chemical Reviews* **1986**, *86*, 1049-1109.

(8) Lagerqvist, A. PERTURBATIONS IN THE BAND SPECTRUM OF BERYLLIUM OXIDE. *Nature* **1946**, *157*, 547-547.

(9) Thompson, C. A.; Andrews, L. REACTIONS OF LASER-ABLATED BE ATOMS WITH O-2 - INFRARED-SPECTRA OF BERYLLIUM OXIDES IN SOLID ARGON. *Journal of Chemical Physics* **1994**, *100*, 8689-8699.

(10) Verhaege.G; Richards, W. G. VALENCE LEVELS OF BERYLLIUM OXIDE. *Journal of Chemical Physics* **1966**, *45*, 1828-&.

(11) Huo, W. M.; Freed, K. F.; Klempere.W. VALENCE EXCITED STATED OF BEO. *Journal of Chemical Physics* **1967**, *46*, 3556-&.

(12) Yoshimin.M. COMPUTED GROUND STATE PROPERTIES OF BEO MGO CAO AND SRO IN MOLECULAR OBITAL APPROXOXIMATION. *Journal of the Physical Society of Japan* **1968**, *25*, 1100-&.

(13) Schaefer, H. F. ELECTRON CORRELATION IN LOWEST SIGMA-1+ STATE OF BERYLLIUM OXIDE. *Journal of Chemical Physics* **1971**, *55*, 176-&.

(14) Oneil, S. V.; Pearson, P. K.; Schaefer, H. F. REPULSIVE SIGMA-3(-) AND LOW-LYING (=1.9EV) SIGMA-3(+) STATES OF BEO. *Chemical Physics Letters* **1971**, *10*, 404-&.

(15) Pearson, P. K.; Schaefer, H. F.; Oneil, S. V. ROLE OF ELECTRON CORRELATION IN A-PRIORI PREDICTIONS OF ELECTRONIC GROUND STATE OF BEO. *Journal of Chemical Physics* **1972**, *56*, 3938-&.

(16) Yoshioka, Y.; Jordan, K. D. MANY-BODY PERTURBATION THEORETICAL-STUDIES OF THE DIPOLE-MOMENTS, POLARIZABILITIES, AND ELECTRON-AFFINITIES OF LIF AND BEO. *Journal of Chemical Physics* **1980**, *73*, 5899-5901.

(17) Bauschlicher, C. W.; Yarkony, D. R. MCSCF WAVE-FUNCTIONS FOR EXCITED-STATES OF POLAR-MOLECULES - APPLICATION TO BEO. *Journal of Chemical Physics* **1980**, *72*, 1138-1144.

(18) Yoshioka, Y.; Jordan, K. D. POLARIZABILITIES, DIPOLE-MOMENTS AND ELECTRON-AFFINITIES OF LIF AND BEO. *Chemical Physics* **1981**, *56*, 303-320.

(19) Irisawa, J.; Iwata, S. ABINITIO STUDIES OF THE LOW-LYING STATES OF BEO. *Theoretica Chimica Acta* **1992**, *81*, 223-235.

(20) Watts, J. D.; Urban, M.; Bartlett, R. J. ACCURATE ELECTRICAL AND SPECTROSCOPIC PROPERTIES OF X(1) SIGMA(+) BEO FROM COUPLED-CLUSTER METHODS. *Theoretica Chimica Acta* **1995**, *90*, 341-355.

(21) Adamovic, I.; Parac, M.; Hanrath, M.; Peric, M. Ab initio study of the electronic spectrum of BeO. *Journal of the Serbian Chemical Society* **1999**, *64*, 721-735.

(22) Sorensen, T. E.; England, W. B. Valence states of BeO Feynman's way. *International Journal of Quantum Chemistry* **2000**, *76*, 259-279.

(23) Diercksen, G. H. F.; Sadlej, A. J.; Urban, M. ELECTRIC PROPERTIES OF IONIC DIATOMS - BEO. *Chemical Physics* **1991**, *158*, 19-32.

(24) Thrush, B. A. THE GROUND STATE OF BERYLLIUM OXIDE. *Proceedings of the Chemical Society of London* **1960**, 339-340.

(25) Merritt, J. M.; Bondybey, V. E.; Heaven, M. C. Spectroscopy, Structure, and Ionization Energy of BeOBe. *Journal of Physical Chemistry A* **2009**, *113*, 13300-13309.

(26) Ostojic, B.; Jensen, P.; Schwerdtfeger, P.; Assadollahzadeh, B.; Bunker, P. R. The predicted infrared spectrum of the hyperberyllium molecule BeOBe in its (X)over-tilde(1)Sigma(+)(g) and (a)over-tilde(3)Sigma(+)(u) electronic states. *Journal of Molecular Spectroscopy* **2010**, *263*, 21-26.

(27) Andrews, L.; Chertihin, G. V.; Thompson, C. A.; Dillon, J.; Byrne, S.; Bauschlicher, C. W. Infrared spectra and quantum chemical calculations of group 2 MO(2), O(2)MO(2), and related molecules. *Journal of Physical Chemistry* **1996**, *100*, 10088-10099.

(28) Zhou, Z. J.; Li, Y. Z.; Zhuang, J.; Wang, G. J.; Chen, M. H.; Zhao, Y. Y.; Zheng, X. M.; Zhou, M. F. Formation and Characterization of Two Interconvertible Side-On and End-On Bonded Beryllium Ozonide Complexes. *Journal of Physical Chemistry A* **2011**, *115*, 9947-9953.

(29) Jordan, K. D.; Griffing, K. M.; Kenney, J.; Andersen, E. L.; Simons, J. THEORETICAL-STUDY OF STABLE NEGATIVE-IONS OF POLAR-MOLECULES - NAH-, LIH-, LIF-, BEO. *Journal of Chemical Physics* **1976**, *64*, 4730-4740.

(30) Jordan, K. D.; Seeger, R. ABINITIO STUDY OF GROUND-STATE ANIONS OF LIF, NAF, BEO AND MGO. *Chemical Physics Letters* **1978**, *54*, 320-326.

(31) Gutsev, G. L.; Nooijen, M.; Bartlett, R. J. Valence and excited dipole-bound states of polar diatomic anions: LiH-, LiF-, LiCl-, NaH-, NaF-, NaCl-, BeO-, and MgO. *Chemical Physics Letters* **1997**, *276*, 13-19.

(32) Neumark, D. M. Slow Electron Velocity-Map Imaging of Negative Ions: Applications to Spectroscopy and Dynamics. *Journal of Physical Chemistry A* **2008**, *112*, 13287-13301.

(33) Leon, I.; Yang, Z.; Liu, H. T.; Wang, L. S. The design and construction of a high-resolution velocity-map imaging apparatus for photoelectron spectroscopy studies of size-selected clusters. *Review of Scientific Instruments* **2014**, *85*, 12.

(34) Eppink, A.; Parker, D. H. Velocity map imaging of ions and electrons using electrostatic lenses: Application in photoelectron and photofragment ion imaging of molecular oxygen. *Review of Scientific Instruments* **1997**, *68*, 3477-3484.

(35) Mascaritolo, K. J.; Gardner, A. M.; Heaven, M. C. Autodetachment spectroscopy of the aluminum oxide anion dipole bound state (vol 143, 114311, 2015). *Journal of Chemical Physics* **2015**, *143*.

(36) Duncan, M. A. Invited Review Article: Laser vaporization cluster sources. *Review of Scientific Instruments* **2012**, *83*, 19.

(37) Wiley, W. C.; McLaren, I. H. TIME-OF-FLIGHT MASS SPECTROMETER WITH IMPROVED RESOLUTION. *Review of Scientific Instruments* **1955**, *26*, 1150-1157.

(38) Li, W.; Chambreau, S. D.; Lahankar, S. A.; Suits, A. G. Megapixel ion imaging with standard video. *Review of Scientific Instruments* **2005**, *76*, 7.

(39) Roberts, G. M.; Nixon, J. L.; Lecointre, J.; Wrede, E.; Verlet, J. R. R. Toward real-time charged-particle image reconstruction using polar onion-peeling. *Review of Scientific Instruments* **2009**, *80*, 7.

(40) Dick, B. Inverting ion images without Abel inversion: maximum entropy reconstruction of velocity maps. *Physical Chemistry Chemical Physics* **2014**, *16*, 570-580.

(41) Hotop, H.; Lineberger, W. C. BINDING-ENERGIES IN ATOMIC NEGATIVE-IONS .2. *Journal of Physical and Chemical Reference Data* **1985**, *14*, 731-750.

(42) Martin, W. C.; Zalubas, R.; Musgrove, A. ENERGY-LEVELS OF SULFUR, S-I THROUGH S-XVI. *Journal of Physical and Chemical Reference Data* **1990**, *19*, 821-880.

(43) Blondel, C.; Chaibi, W.; Delsart, C.; Drag, C. The fine structure of S and S- measured with the photodetachment microscope. *Journal of Physics B-Atomic Molecular and Optical Physics* **2006**, *39*, 1409-1416.

(44) Wei, J.; Kuczmann, A.; Riedel, J.; Renth, F.; Temps, F. Photofragment velocity map imaging of H atom elimination in the first excited state of pyrrole. *Physical Chemistry Chemical Physics* **2003**, *5*, 315-320.

(45) Ahmed, M.; Peterka, D. S.; Suits, A. G. Crossed-beam reaction of O(D-1)+D-2 -> OD+D by velocity map imaging. *Chemical Physics Letters* **1999**, *301*, 372-378.

(46) Werner, H. J.; Knowles, P. J.; Knizia, G.; Manby, F. R.; Schutz, M. Molpro: a general-purpose quantum chemistry program package. *Wiley Interdisciplinary Reviews-Computational Molecular Science* **2012**, *2*, 242-253.

(47) Halkier, A.; Helgaker, T.; Jorgensen, P.; Klopper, W.; Koch, H.; Olsen, J.; Wilson, A. K. Basis-set convergence in correlated calculations on Ne, N-2, and H2O. *Chemical Physics Letters* **1998**, *286*, 243-252.

(48) LeRoy, R. J.: LEVEL 8.0: A Computer Program for Solving the Radial Schrödinger Equation for Bound and Quasibound Levels. University of Waterloo Chemical Physics Research Report CP-663, 2007.

(49) Cooper, J.; Zare, R. N. ANGULAR DISTRIBUTION OF PHOTOELECTRONS. *Journal of Chemical Physics* **1968**, *48*, 942-&.

Conclusion to Dissertation

The design and functionality of the first two stages of the spectrometer described in the preceding chapters displayed excellent performance in recording cold, high resolution molecular spectroscopic data of previously unreported systems. The $^2\Pi(4p)$ – X $^2\Pi$ $(3p)$ band system of AlAr van der Waals complex was observed using two-photon excitation. The spectrum revealed a short progression, showing doublet bands consistent with the spin-orbit intervals of Al(4*p*).

Rotationally and vibrationally cold spectroscopic data were measured for the 2 ^{2}A' – X ^{2}A' transitions of the BeOH/D radicals. Several bending mode transitions were identified for both species, allowing for comparison with previously published MRCI calculations. Predictions that the molecule is quasilinear in the ground state were confirmed. Lastly, the $^1\Sigma^+ \leftarrow$ X $^1\Sigma^+$ electronic transition between the ground state and the dipole bound excited state of AlO^- was characterized using autodetachment spectroscopy. Rotationally resolved data for the 0-0 and 1-1 bands provided molecular constants for the upper and lower states, the electron affinity of AlO, and the electron binding energy of the dipole bound state. These benchmark studies laid the foundation for the incorporation of a velocity – map imaging (VMI) spectrometer. With this addition, photoelectron kinetic energies (eKE) and their angular anisotropy upon detachment could be measured.

The overall construction and testing of the photoelectron velocity – map imaging spectrometer was shown to be successful with respect to the recording of focused images of photoelectrons produced from the photodetachment of mass selected anions. A

resolution that allowed for unambiguous assignment of the six detachment transitions of S^- ($^3P_{2,1,0} \leftarrow {}^2P_{3/2,\ 1/2}$) was achieved, providing accurate eKE measurements for calibration of the VMI optics. While the sequence band transitions seen for the detachment of BeO^- were unable to be resolved, the measurements of the electron detachment threshold energy and the $\Delta G_{1/2}$ vibrational interval of the anion were determined and found to be in agreement with theoretical predictions.

Moving forward, steps will be taken to improve the resolution of the VMI optics. When completed, the order of magnitude better resolution that could be realized with the current VMI optical design will greatly reduce the uncertainty of the experimental values reported for BeO^-. Additionally, the improved resolution will be necessary in determining the vibrational intervals and overall energy level structure of larger neutral and anionic beryllium containing molecules and clusters. These measurements will help evaluate theoretical predictions of the electronic structures of these species. Experimentally verified theoretical models will provide insight into the unusual bonding characteristics of beryllium.